SHAPE OPTIMIZATION OF MICROSTRUCTURES GOVERNED BY MAXWELL'S EQUATIONS

A Dissertation

by

MANASWINEE BEZBARUAH

Submitted to the Graduate and Professional School of
Texas A&M University
in partial fulfillment of the requirements for the degree of

DOCTOR OF PHILOSOPHY

Chair of Committee,	Matthias S. Maier
Co-Chair of Committee,	Timothy A. Davis
Committee Members,	Jean-Luc Guermond
	Andrea Bonito
Head of Department,	Peter Howard

May 2025

Major Subject: Mathematics

ABSTRACT

This dissertation focuses on shape optimization of nanoscale optical metamaterials with the aim of fine-tuning their optical properties. These materials have a wide range of applications, from biomedical devices to photovoltaic batteries. They exhibit a variety of striking optical phenomenon that are unlike the classical behavior of electromagnetic waves. The ability to precisely tailor these properties offers emerging possibilities for enhancing the performance of these materials.

A mathematical framework based on homogenization theory for time-harmonic Maxwell's equations is used to model these materials. This framework subsequently enables the formulation of a PDE-constrained shape optimization problem. By defining a cost function that minimizes the difference between the effective permittivity and target permittivity, iterative numerical optimization methods are applied. The computational workflow leverages the finite element library `deal.II` and the optimization library `DOpElib`. Numerical experiments validate the effectiveness of the proposed methods, demonstrating convergence to a variety of target permittivity values without compromising mesh quality. The outcomes highlight the potential of PDE-constrained optimization in advancing the design of plasmonic crystals and metamaterials, pushing the boundaries of material science and optics.

We outline a future extension of the homogenization framework that incorporates a spectral problem to better capture the frequency-dependent optical properties of metamaterials. A promising direction involves introducing a deformation field into the spectral problem and defining a cost function to minimize discrepancies between computed and target eigenvalues, allowing for an alternative approach to tune the microscale properties of these metamaterials. Additionally, improving computational efficiency through high-performance sparse matrix libraries like `GraphBLAS` will address bottlenecks in assembling finite element matrices, enabling fast, scalable, and multi-threaded simulations. These advancements will enhance the feasibility of large-scale, high-fidelity simulations.

DEDICATION

To my younger self, who decided to embark on this difficult journey.

ACKNOWLEDGMENTS

First and foremost, I would like to sincerely thank my supervisor, Dr. Matthias Maier. I am immensely grateful for the time you have dedicated to me, the mathematical insights you have shared, and the unwavering support you have provided over the past six years. This thesis would not have been possible without you, and it has been an absolute privilege to work alongside you!

I would also like to thank my committee members for their patience and guidance: Dr. Tim Davis, Dr. Jean-Luc Guermond and Dr. Andrea Bonito; your time and feedback was greatly appreciated. Im also extremely grateful towards all the administrative staff in the Department of Mathematics at TAMU.

To all my friends who have supported me: thank you for your encouragement, humor, and for lending me a listening ear. Thank you to the numerical analysis group and my fellow graduate students in the department for their input, discussions, and company. Special thanks needs to be extended to my friends Grey, Jacquie, and Rachel - you all have been my strongest supporters and my yappiest girls. Sneha - I am so incredibly grateful for your unshakable friendship from across the pond. Thank you for believing in me at my lowest.

Thank you to my extended family who have always encouraged me to dream big. Finally, I would like to thank my parents for teaching me resilience and for never giving up on me. Through sadness and laughter, you have always been there for me and I don't know what I would do without your never ending love. ♡

CONTRIBUTORS AND FUNDING SOURCES

Contributors

This work was supported by a dissertation committee consisting of Dr. Matthias Maier (chair) of the Department of Mathematics at Texas A&M University, Dr. Timothy Davis (chair) of the Department of Computer Science and Engineering at Texas A&M University, Dr. Jean-Luc Guermond and Dr. Andrea Bonito of the Department of Mathematics at Texas A&M University.

The majority of this dissertation is based on joint work with Dr. Matthias Maier and Dr. Winnifried Wollner [9], and Section 6.2 is based on joint work with Dr. Tim Mattson, Dr. Matthias Maier, Dr. Scott McMillan, Dr. Michel Pelletier, Dr. Erik Welch, and Dr. Timothy Davis [62]. All other work conducted for the dissertation was completed by the student independently.

Funding Sources

This work was supported in part by the National Science Foundation grants DMS-1912847 and DMS-2045636, and in part by a teaching assistantship from Texas A&M University.

TABLE OF CONTENTS

Page

LIST OF FIGURES

FIGURE Page

LIST OF TABLES

TABLE Page

1. INTRODUCTION

The emergence of two-dimensional material with innovative material properties has transformed several areas of optics and nanophotonics. One such material is *graphene*, a two-dimensional carbon allotrope with a single atom layer that is arranged in a honeycomb lattice structure. Since its successful exfoliation in 2004 [81], graphene has attracted great interest due to its exceptional electrical, mechanical, thermal, and optical properties. Doped monolayer graphene [18, 21, 22] exhibits optical conductivity that enables strong light-matter interactions across a broad frequency spectrum, spanning from the terahertz to the mid-infrared range. This unique property has driven the development of innovative graphene-based *plasmonic devices* and metamaterials with tunable optical properties.

Plasmonic crystals are a promising class of metamaterials that have demonstrated a range of optical phenomena that challenge conventional electromagnetic wave behavior. These include optical cloaking, negative refraction, subwavelength focusing, and the epsilon-near-zero effect [4, 14, 61, 64, 68, 86]. Such properties make plasmonic materials highly desirable for applications in photonics, waveguiding, sensing, and quantum optics. Traditionally, plasmons were studied at metal-dielectric interfaces. However, using metals in plasmonics has several limitations. First, plasmon activity in metals occurs primarily in the near-infrared range, which isn't ideal for all applications. Second, metals heavily dampen electromagnetic waves, resulting in short plasmon lifetimes. Lastly, the carrier concentration in metals is fixed, meaning plasmonic devices made from metals can only function at specific light wavelengths.

In recent years, graphene has emerged as an alternate material for plasmonics which overcomes the shortcomings of metals. A well-studied example of a plasmonic crystal consists of *graphene nanosheets* that are arranged periodically with subwavelength spacing and suspended in a bulk non-magnetic dielectric host. This dissertation describes a class of *shape optimization problems* for the nanoscale graphene inclusion with the aim of *fine-tuning the*

macroscale optical properties of the plasmonic metamaterial. The ability to tune the effective optical response of these structures is a fundamental challenge in designing novel optical devices.

Plasmonic crystals and similar periodically structured media can be modeled with classical electrodynamics. They are governed by *time-harmonic Maxwells equations*, which describes the time harmonic optical response on the microscale layers. However, resolving the system of equations for each layer of the nanosheet at the microscale is computationally expensive. Instead, *homogenization* techniques provide a framework for describing the macroscopic optical response of a microscopically structured material. These methods replace the complex microstructure with microscale inclusions by a homogenous bulk material with *effective* optical properties.

Our homogenization approach builds on a theory (see Section 2.3) of convergence developed by Nguetseng [69] and a two-scale convergence result established by Allaire [2]. The extension of this two-scale convergence to the context of this research is based on a periodic homogenization theory for time-harmonic Maxwell equations [83–85], which is extended to our periodic inclusions composed of lower-dimensional interfaces [5, 58, 60]. This method replaces the permittivity of each periodic inclusion with an equivalent *effective permittivity tensor*. The tensor is computed as a weighted average over a *cell problem*. This framework not only provides valuable theoretical insights but also offers an efficient computational tool for simulating the optical macroscale response of these materials.

Finally, we introduce an important inverse problem: *Given a specific macroscopic optical property, can we determine the shape of the microstructure of a plasmonic crystal?*. Traditional approaches [70, 77] to this inverse problem have relied on heuristic design principles or extensive parameter sweeps, which can be inefficient and limited in scope. In this research, we treat the geometry of the inclusions as the control variable and formulate a shape-optimization problem based on the homogenization procedure. This thesis presents a mathematical and computational framework for such optimization problems, integrating

numerical shape optimization methods with *inverse* homogenization theory.

As an addendum, we lay the foundation for a related *frequency-independent* optimization problem. The frequency-independent problem is constrained by a *geometric eigenvalue problem*, which arises as a result of the interplay between frequency-independent geometric nanoscale resonances and frequency-dependent local conductivity models [45]. This formulation is crucial for understanding the frequency response of our optical metamaterials and it enables an efficient approximation to compute this frequency response. The optimization framework is similar to the one used above. We end with some remarks on the computational bottlenecks of our optimization routine and suggest some high-performance alternatives for the algorithms employed.

Thesis objectives: Our objective with this research is to develop robust shape optimization frameworks for designing plasmonic crystals with predetermined effective optical properties. This involves solving a mathematically rigorous inverse problem that determines the optimal shape of the microscale dielectric inclusions in order to achieve a target macroscopic response. More concretely, the objectives are:

- *Extending the homogenization framework for plasmonic crystal*: We build upon existing homogenization theory for time-harmonic Maxwells equations, incorporating shape deformations into the formulation. A deformation field is introduced to describe deviations from a reference geometry, allowing for control over the shape of the inclusions.

- *Formulating a numerical shape optimization algorithm*: An optimization problem is formulated, where the objective is to minimize the difference between the computed effective permittivity tensor and a given target tensor. The deformation field serves as the control variable, the governing PDE serves as the state variable, and constraints are introduced to maintain mesh regularity and avoid singular deformations.

- *Implementing an adjoint-based optimization method*: The optimization framework employs an adjoint formulation, which enables efficient computation of derivatives for

gradient-based numerical optimization. This is combined with numerical optimization algorithms based on gradient descent and Broyden-Fletcher-Goldfarb-Shanno (BFGS) to form optimization algorithms.

– *Validating the approach with numerical experiments*: The optimization algorithm is applied to various test cases to demonstrate its ability to tune optical microstructures. We in particular demonstrate that our shape optimization formulation works for tuning optical microstructures to achieve an epsilon-near-zero effect.

Thesis layout: To provide a comprehensive and systematic presentation of the research, the remainder of this thesis is structured as follows,

Chapter 2 is a review of homogenization techniques, which are essential for understanding the behavior of plasmonic crystals at the macroscale. The chapter starts with an introduction to the heterogeneous Maxwells equations and the jump conditions, which govern the electromagnetic behavior of the material. It then delves into a description of the layered and periodic structure of the plasmonic crystals. Then, a systematic review of the homogenization process is presented, starting with convergence of periodically oscillating functionals and linear elliptic equations. Finally, we review the homogenization of the time-harmonic Maxwell's equations on the plasmonic crystals and some well-posedness theorems required for our analysis.

Chapter 3 introduces the deformation field, which plays a crucial role in formulating out shape optimization problem. The chapter then discusses the deformed cell problem and proves the well-posedness of the deformed problem, ensuring that the mathematical formulation is uniquely solvable under reasonable assumptions. In addition, the chapter introduces regularity and variance bounds, which are critical for ensuring the accuracy and stability of the numerical methods used later. These bounds help control the behavior of the deformation and ensure that the optimization techniques applied later can be relied upon to yield valid results.

In Chapter 4, the focus shifts to the shape optimization problem. The chapter explains

the mathematical formulation of the optimization problem; describing the objective function, constraints, and the methods used to solve it. A key technique introduced here is the adjoint approach, which is a method used to efficiently compute gradients. The chapter provides anexplanation of the numerical optimization algorithms and their implementation. Additionally, strategies for mesh regularization are discussed.

Chapter 5 presents the results of several numerical experiments designed to test and validate the framework developed in previous chapters. These experiments provide concrete evidence of the effectiveness, accuracy, and robustness of the proposed methods. The final chapter of the thesis (Chapter 6) offers a summary of the key findings from the research, highlighting the contributions made. We also provide some outlook and summarize two directions of future work. We lay the groundwork for a frequency-independent optimization problem, which provides an alternate mathematical approach using a geometric eigenvalue problem. Later, we discuss some computational bottlenecks and techniques to speed up the existing algorithms. Specifically, we propose some methods to speed up the finite element assembly that occurs in every iteration of our numerical optimization routine.

2. A SURVEY OF HOMOGENIZATION

This chapter is dedicated to summarizing the underlying microscale model [58] and the corresponding homogenization theory [2, 58–60, 69, 83–85]. The concepts reviewed are: heterogeneous time-harmonic Maxwell's equations, a conductivity model, the setup of plasmonic crystals, periodically oscillating PDEs, two-scale convergence, homogenization of linear elliptic equations, and homogenization of time-Harmonic Maxwell's equations.

2.1 Time-harmonic Maxwell's equations

The starting point of our analysis is the strong form of Maxwells equations. Maxwell's equations describe the time evolution of an electromagnetic field $(\boldsymbol{\mathcal{E}}(t,\boldsymbol{x}),\boldsymbol{\mathcal{H}}(t,\boldsymbol{x}))$ as,

$$\begin{cases} \nabla\times\boldsymbol{\mathcal{E}} &= -\mu\frac{\partial\boldsymbol{\mathcal{H}}}{\partial t}, \\ \nabla\times\boldsymbol{\mathcal{H}} &= \varepsilon\frac{\partial\boldsymbol{\mathcal{E}}}{\partial t}+\boldsymbol{\mathcal{J}}_a. \end{cases} \tag{2.1}$$

Here, $\boldsymbol{\mathcal{E}}$ and $\boldsymbol{\mathcal{H}}$ are time-dependent electric and magnetic fields, ε and μ are the relative electrical permittivity and magnetic permeability of the material, and $\boldsymbol{\mathcal{J}}_a$ is the current density. For the purpose of this work, we operate in the time-harmonic realm, which means we use the the time-harmonic electromagnetic field $(\boldsymbol{\mathcal{E}}(t,\boldsymbol{x}),\boldsymbol{\mathcal{H}}(t,\boldsymbol{x})) = \mathrm{Re}\big(e^{-i\omega t}(\boldsymbol{E}(\boldsymbol{x}),\boldsymbol{H}(\boldsymbol{x}))\big)$. Plugging into (2.1), we arrive at the time-harmonic Maxwell's equations:

$$\begin{cases} \nabla\times\boldsymbol{E} &= i\omega\mu\boldsymbol{H}, \\ \nabla\times\boldsymbol{H} &= -i\omega\varepsilon\boldsymbol{E}+\boldsymbol{J}_a, \end{cases} \tag{2.2}$$

The (constant) parameter ω is the temporal angular frequency ($\omega>0$), $\boldsymbol{J}_a$ is the time-independent current density that arises from the time-harmonic density,

$$\boldsymbol{\mathcal{J}}_a(t,\boldsymbol{x}) = \mathrm{Re}(\big(e^{-i\omega t}(\boldsymbol{J}_a(\boldsymbol{x})\big).$$

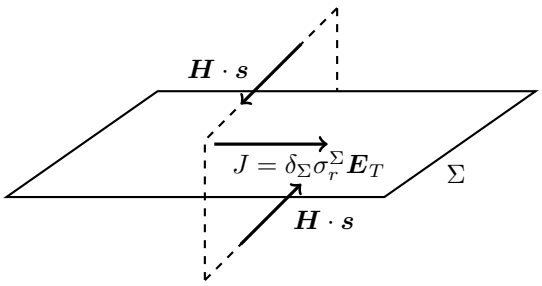

Figure 2.1: Jump condition on the graphene surface.

2.1.1 Modeling of graphene as effective jump conditions

Our domain is plasmonic crystals consisting of graphene nanosheets. Due to the surface conductivity of graphene we have a jump condition in the tangential component of the magnetic field, while the tangential electric field is continuous. The jump on the surface Σ with respect to a chosen normal field ν is denoted as $[\boldsymbol{F}]_\Sigma := \lim_{\alpha\searrow 0}\Big(\boldsymbol{F}(\boldsymbol{x}+\alpha\boldsymbol{\nu}) - \boldsymbol{F}(\boldsymbol{x}-\alpha\boldsymbol{\nu})\Big)$, $\boldsymbol{x}\in\Sigma$ and the equations on the surface are:

$$\begin{cases} \big[\boldsymbol{\nu}\times\boldsymbol{E}\big]_\Sigma &= 0, \\ \big[\boldsymbol{\nu}\times\boldsymbol{H}\big]_\Sigma &= \sigma^\Sigma\boldsymbol{E}_T. \end{cases} \tag{2.3}$$

Here, σ^Σ is the surface conductivity of Σ and $\boldsymbol{E}_T$ is the tangential component of $\boldsymbol{E}$. The surface conductivity in the parameter regimes relevant to our the numerical tests will be given by the Drude model, also known as a Drude-Lorentz oscillator model [3, 23, 30] (described below).

2.1.2 A conductivity model

The Drude model was proposed by Paul Drude in 1900 [23]. In this section, we provide a brief summary of the model based on notes by Almog, et al. [3]. The Drude model represents an electron as a driven damped harmonic oscillator. Let the mass of the electron be m_e and

charge be $-q$, and we let $\boldsymbol{y}$ be the position vector of the electron. Let us begin with the scenario where there is no dampening and suppose the harmonic oscillator has force constant k, and by Newton's second law of motion, $-k\boldsymbol{y} = m_e \frac{\partial^2 \boldsymbol{y}}{\partial t^2}$. The solution to this equation is a sine function of frequency $\omega_0 := \sqrt{\frac{k}{m_e}}$, and this is called the *resonant frequency*, (or *natural frequency* or *fundamental frequency*) [3].

Now let us look at the case where we have a dampening force and an oscillating electric field $\boldsymbol{E}$. As described by Almog, Bradley, and Bulović [3], the damping force is assumed to be linearly proportional to the velocity of the mass. Assume that electrons scatter randomly at uncorrelated times. The average time between scattering is τ, also known as the *relaxation time* and therefore, $\frac{1}{\tau}$ is the *damping coefficient* of our imaginary spring. So the damping force is $-m_e \frac{1}{\tau} \frac{\partial \boldsymbol{y}}{\partial t}$. The driving force due to the electric field is $-q\boldsymbol{E}$. The total force on the electron is [3],

$$\begin{aligned} F_{\text{net}} &= F_{\text{driving}} + F_{\text{damping}} + F_{\text{oscillator}}, \\ \implies m_e \frac{\partial^2 \boldsymbol{y}}{\partial t^2} &= -m_e \omega_0^2 \boldsymbol{y} - m_e \frac{1}{\tau} \frac{\partial \boldsymbol{y}}{\partial t} - q\boldsymbol{E}, \\ \implies \frac{\partial^2 \boldsymbol{y}}{\partial t^2} + \frac{1}{\tau} \frac{\partial \boldsymbol{y}}{\partial t} + \omega_0^2 \boldsymbol{y} &= -\frac{q}{m_e} \boldsymbol{E}. \end{aligned} \tag{2.4}$$

Polarization $\boldsymbol{P}$ is the number of dipole moments per volume. If N is the number of electrons per volume then $\boldsymbol{P} := -Nq\boldsymbol{y}$. Also, plasma frequency $\omega_p := \sqrt{\frac{Nq}{m_e \varepsilon_0}}$, where ε_0 is the electric permittivity of vacuum [41].

$$\frac{\partial^2 \boldsymbol{P}}{\partial t^2} + \frac{1}{\tau} \frac{\partial \boldsymbol{P}}{\partial t} + \omega_0^2 \boldsymbol{P} = \frac{Nq^2}{m_e} \boldsymbol{E} = \varepsilon_0 \omega_p^2 \boldsymbol{E}. \tag{2.5}$$

Solve this system for $\boldsymbol{P}$, and then compute the susceptibility χ_e using the other formula for polarization $\boldsymbol{P} = \varepsilon_0 \chi_e \boldsymbol{E}$. The relative electric permittivity ε_r or the *dielectric constant* is computed using $\varepsilon_r = 1 + \chi_e$. If we treat the electrons as conductive current with the given electron density, we can use ε_r to find the current density, which in conjunction with the

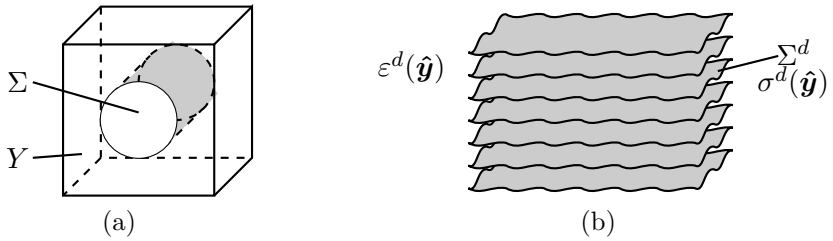

Figure 2.2: (a) The unit cell $Y = [0,1]^3$ consisting of 2D graphene inclusions Σ with surface conductivity σ in an ambient host material with permittivity ε; (b) the plasmonic crystal formed by many scaled and repeated copies of Y in all space directions.

Ohm's law, can be used to arrive at the surface conductivity [58]:

$$\sigma(\boldsymbol{x}, \boldsymbol{y}) \;=\; \tilde{\sigma}(\omega)\, \boldsymbol{I}, \qquad \tilde{\sigma}(\omega) = \frac{\mathrm{i}\omega_p}{\omega + \mathrm{i}/\tau}, \qquad \omega_p,\, \tau \in \mathbb{R}_{\geq 0}. \tag{2.6}$$

Here $\boldsymbol{I}$ is the identity matrix. This is a common model for the surface conductivity of graphene, and after a suitable rescaling, typical values for the constants are $\omega_p \approx 4/137$ and $\tau \approx 100$ for frequencies $\omega \approx 1$ [45].

2.2 A microscopic model of the layered heterostructure

We now review the geometry of the microscopic problem as described by Maier [45, 58–60]. This structure is the basis of our shape optimization later in this work. Figure 2.2 shows the geometry of a three-dimensional plasmonic crystal consisting of periodic copies of a scaled representative volume element Y containing a curved surface Σ representing a 2D material with surface conductivity σ and otherwise filled with a dielectric host material. This shape of this curved surface Σ being optimized in our analysis. The parameter d denotes a *scaling parameter* or *periodicity* for the for the microscale inclusions [60]:

$$\Sigma^d = \big\{ d\,\boldsymbol{z} + d\,\boldsymbol{\varsigma} \;\;:\;\; \boldsymbol{z} \in \mathbb{Z}^3,\; \boldsymbol{\varsigma} \in \Sigma \big\}.$$

Finally, Σ^d is the union of all scaled copies of Σ, as illustrated in Figure 2.2 [60].

The electromagnetic response on each periodic layer is described by the time-harmonic Maxwell equations governing the scattering of an electromagnetic wave $(\boldsymbol{E}^d, \boldsymbol{H}^d)$, as follows [56]:

$$\begin{cases} \nabla \times \boldsymbol{E}^d = i\omega\mu \boldsymbol{H}^d, \\ \nabla \times \boldsymbol{H}^d = -i\omega\varepsilon^d \boldsymbol{E}^d + \boldsymbol{J}_a^d, \\ \left[\boldsymbol{\nu} \times \boldsymbol{E}^d\right]_{\Sigma^d} = 0, \\ \left[\boldsymbol{\nu} \times \boldsymbol{H}^d\right]_{\Sigma^d} = (\sigma^d \boldsymbol{E}^d)_{\mathbf{t}}. \end{cases} \tag{2.7}$$

Here, ε^d is the electric permittivity and $\boldsymbol{J}_a^d$ is the electric current density of each copy of Σ^d. As described above, we see jump conditions over the graphene interface Σ^d due to the presence of a current density $\boldsymbol{J}_{\Sigma^d} = \delta_{\Sigma^d}\sigma^d \boldsymbol{E}_{\mathbf{t}}^d$ caused by the surface conductivity σ^d [58]. Here, δ_{Σ^d} is the surface measure of Σ^d. We refer the reader to [60] for a more detailed discussion of the scaling provided by Maier, et. al.

Note that the permittivity ε^d and surface conductivity σ^d are tensor-valued. We make the additional scaling assumption on (bulk) permittivity and surface conductivity that they depend on a slow scale and are periodic and rapidly oscillating on a fast scale proportional to d, namely [60],

$$\varepsilon^d(\boldsymbol{x}) = \varepsilon(\boldsymbol{x}, \boldsymbol{x}/d), \qquad \sigma^d(\boldsymbol{x}) \,=\, d\,\sigma(\boldsymbol{x}, \boldsymbol{x}/d). \tag{2.8}$$

$\varepsilon(\boldsymbol{x}, \boldsymbol{y})$ and $\sigma(\boldsymbol{x}, \boldsymbol{y})$ are complex-valued scalar functions, periodic with respect to $y \in Y$, and σ is Lipschitz continuous. Equation (2.7) implies the following equation in $\Omega \setminus \Sigma_d$,

$$\frac{1}{\mu}\nabla \times (\nabla \times \boldsymbol{E}^d) = \omega^2 \varepsilon^d \boldsymbol{E}^d + i\omega \boldsymbol{J}^d. \tag{2.9}$$

Along with $\boldsymbol{H}^d = \frac{1}{i\omega\mu}\nabla \times \boldsymbol{E}^d$, we arrive at the *impedance boundary condition*,

$$\frac{1}{\mu}(\nabla \times \boldsymbol{E}^d) \times \boldsymbol{\nu} = i\omega\lambda \boldsymbol{E}_t^d \ \text{ on } \partial\Omega. \tag{2.10}$$

Where $\boldsymbol{\nu}$ is a normal unit vector and $\lambda = \sqrt{\frac{\varepsilon}{\mu}}$. Consider a smooth test function ψ. We formulate the weak form [60],

$$\begin{aligned}\int_\Omega \frac{1}{\mu}(\nabla \times \boldsymbol{E}^d) \cdot (\nabla \times \bar{\psi})\,\mathrm{d}y - \int_{\partial\Omega} i\omega\lambda \boldsymbol{E}^d \cdot \bar{\psi}_T\,\mathrm{d}o_y - \int_\Omega \omega^2 \varepsilon^d \boldsymbol{E}^d \cdot \bar{\psi}\,\mathrm{d}y \\ - \int_{\Sigma^d} i\omega\sigma^d \boldsymbol{E}_T^d \cdot \bar{\psi}_T\,\mathrm{d}o_y = \int_\Omega i\omega \boldsymbol{J}_a \cdot \bar{\psi}\,\mathrm{d}y.\end{aligned} \tag{2.11}$$

Let us define the function space [60],

$$X^d = \{\boldsymbol{u} \in H(\mathrm{curl};\Omega) \mid \boldsymbol{u}_T \in L^2(\partial\Omega;\mathbb{C}^3)\},$$

along with the norm [60],

$$\|\boldsymbol{u}\|_{X^d}^2 = \|\boldsymbol{u}\|_{L^2(\Omega)}^2 + \|\nabla \times \boldsymbol{u}\|_{L^2(\Omega)}^2 + \|\boldsymbol{u}_T\|_{L^2(\partial\Omega)}^2 + \|\boldsymbol{u}_T\|_{L^2(\Sigma^d)}^2.$$

Here, $H(\mathrm{curl};\Omega) := \{\boldsymbol{u} \in L^2(\Omega;\mathbb{C}^3) \mid \nabla \times \boldsymbol{u} \in L^2(\Omega;\mathbb{C}^3)\}$ and $\boldsymbol{u}_T = (\boldsymbol{\nu} \times \boldsymbol{u}) \times \boldsymbol{\nu}$ is the tangential component of $\boldsymbol{u}$. Also,

$$\|\boldsymbol{u}_T\|_{L^2(\Sigma^d)}^2 := d\int_{\Sigma^d} |\boldsymbol{u}_T|^2\,\mathrm{d}o_y = \sum_{k\in\Gamma^d} d\int_\Sigma |\boldsymbol{u}_T(x', kd)|^2\,\mathrm{d}y'.$$

A precise formulation (2.11) with the the function space describes above is as follows,

$$\boldsymbol{E}^d \in X^d, \quad a^d(\boldsymbol{E}^d, \boldsymbol{\Psi}) = i\omega \int_\Omega \boldsymbol{J}_a \cdot \bar{\boldsymbol{\Psi}}\,\mathrm{d}y \qquad \forall \boldsymbol{\Psi} \in X^d. \tag{2.12}$$

where $a^d : X^d \times X^d \to \mathbb{C}$ is defined as [60],

$$a^d(\boldsymbol{u}, \boldsymbol{v}) = \int_\Omega \frac{1}{\mu}(\nabla \times \boldsymbol{u}) \cdot (\nabla \times \bar{\boldsymbol{v}})\, \mathrm{d}y - \int_\Omega \omega^2 \varepsilon^d \boldsymbol{u} \cdot \bar{\boldsymbol{v}}\, \mathrm{d}y$$
$$- \int_{\Sigma^d} i\omega\sigma^d \boldsymbol{u}_T \cdot \bar{\boldsymbol{v}}_T\, \mathrm{d}o_y - \int_{\partial\Omega} i\omega\lambda \boldsymbol{u}_T \cdot \bar{\boldsymbol{v}}_T\, \mathrm{d}o_y.$$

The corresponding magnetic field is given by,

$$\boldsymbol{H}^d(x) = \frac{1}{i\omega\mu} \nabla \times \boldsymbol{E}^d(x).$$

Let us introduce a few assumptions on the parametrs [58, 60]. $\mu, \lambda \in \mathbb{R}_{>0}$ and ε^d, σ^d are measurable complex valued functions such that,

$$\begin{cases} 0 < c \leq \mathrm{Im}(\varepsilon^d(\boldsymbol{x})) \leq C \quad \textit{and} \quad |\mathrm{Re}(\varepsilon^d(\boldsymbol{x}))| \leq C \qquad \forall \boldsymbol{x} \in \Omega \\ 0 < c \leq \frac{1}{d}\mathrm{Re}(\sigma^d(\boldsymbol{x})) \leq C \quad \textit{and} \quad |\frac{1}{d}\mathrm{Im}(\sigma^d(\boldsymbol{x}))| \leq C \qquad \forall \boldsymbol{x} \in \Sigma^d \end{cases} \tag{2.13}$$

for some constants c, C. With this, Maier et al. [60] provide the following theorem,

Theorem 2.2.1 (Well-posedness of the microscale problem [60])**.** *Under the assumptions* (2.13)*,* (2.12) *has a unique solution in* X^d *for all* $\boldsymbol{J}_a \in L^2(\Omega; \mathbb{C}^3)$ *and for all* $d > 0$*.*

The proof of this theorem involves the definition of a sesquilinear form on a limit and the application of Lax-Milgram. Moreover, we have the following a priori estimate:

Proposition 2.2.2 (A priori estimate for the microscale problem [60])**.** *Under the assumption* (2.13)*, the solution* E^d *of* (2.12) *is bounded in* X_d *uniformly with respect to* d*.*

$$\frac{1}{\omega}\|\nabla \times \boldsymbol{E}^d\|^2_{L^2(\Omega)} + \omega\|\boldsymbol{E}^d\|^2_{L^2(\Omega)} + \|(\boldsymbol{E}^d)^T\|^2_{L^2(\Sigma^d)} + \|(\boldsymbol{E}^d)^T\|^2_{L^2(\partial\Omega)} \leq C\|\boldsymbol{J}_a\|_{L^2(\Omega)}. \tag{2.14}$$

Where C *is a constant independent of* d*.*

2.3 Review of homogenization and convergence

Following our discussion of heterogeneous Maxwell's equations, we review the process of homogenization. Homogenization is a mathematical framework used to study differential equations with rapidly oscillating coefficients. This approach enables the derivation of effective macroscopic equations that capture the influence of fine-scale structures without explicitly resolving them. By averaging out microscopic variations, homogenization provides a systematic method to approximate the behavior of complex materials and wave propagation phenomena. The core idea is to replace a highly oscillatory system with an equivalent homogenized model, where effective properties emerge from the periodic microstructure. This section reviews some general homogenization results for elliptic PDEs with periodically oscillating coefficients, and then applies them to homogenize linear inhomogeneous Maxwell's equations. Finally, we summarize the homogenization problem and convergence results for time-harmonic Maxwell's equations in the context of plasmonic crystals.

2.3.1 Periodically oscillating functionals and two-scale convergence

Convergence of periodically oscillating functionals was first introduced by G. Nguetseng in 1989 [69] and then the term *two-scale convergence* was coined by G. Allaire in 1992 [2]. In this section we review some of these concepts, as they apply to our optimization problem. Let Ω be a bounded and open set in $\mathbb{R}^N$ and let $Y =]0,1[^N$ be an open unit cube in $\mathbb{R}^N$. We define $\mathbb{F}_{\#}(Y)$ as all functions in $\mathbb{F}_{loc}(\mathbb{R}^N)$ which are periodical repetitions of some function in $\mathbb{F}(Y)$. For example, $C_{\#}(Y)$ and $C^{\infty}_{\#}(Y)$ are the space of continuous and infinitely differentiable functions, respectively, in $\mathbb{R}^N$ that are periodic of period Y. Note that $L^2_{\#}(Y)$ is the completion for the norm of $L^2(Y)$ of $C^{\infty}_{\#}(Y)$. Let (ε) be a sequence of positive numbers converging to 0. We will utilize functionals of type:

$$F_\varepsilon(\psi) = \int_\Omega u_\varepsilon(x)\psi\big(x, \frac{x}{\varepsilon}\big)\,\mathrm{d}x.$$

Here, u_ε is a function in $L^2(\Omega)$ and is (or depends on) the solution of a partial differential equation on Ω with ε-periodic coefficients (i.e. periodic with period ε in each variable). An admissible test function is defined as follows:

Definition 2.3.1 (Admissible test function [69]). *A test function $\psi(x,y) \in L^2[\Omega; C_\#(Y)]$ is admissible if it is continuous on $\bar{\Omega}\times\mathbb{R}^N$ and for a fixed x, the function $y \to \psi(x,y)$ is periodic with period 1 in each variable. Moreover, for the sequence $(\psi^\varepsilon)_{\varepsilon>0}$ with $\psi^\varepsilon(x) = \psi\big(x, \frac{x}{\varepsilon}\big)$ for $x \in \Omega$, we have:*

$$\lim_{\varepsilon\to 0} \int_Y \psi\left(x, \frac{x}{\varepsilon}\right)^2 \, \mathrm{d}y = \int_\Omega \int_Y \psi(x,y)^2 \, \mathrm{d}x \, \mathrm{d}y.$$

In 1989, G. Nguetseng [69] proved the following theorem:

Theorem 2.3.2 (Two-scale convergence [69]). *For each bounded sequence (u_ε) in $L^2(\Omega)$, there exists a subsequence, still indexed by ε, and a function $u_0(x,y) \in L^2(\Omega \times Y)$ such that for every sufficiently smooth $\psi(x,y)$ which is Y-periodic in y:*

$$\lim_{\varepsilon\to 0} \int_\Omega u_\varepsilon(x) \, \psi\left(x, \frac{x}{\varepsilon}\right) \, \mathrm{d}x = \int_\Omega \int_Y u_0(x,y) \, \psi(x,y) \, \mathrm{d}y \, \mathrm{d}x, \tag{2.15}$$

G. Allaire [2] defined the type of convergence described by 2.15 as *two-scale convergence*. The idea of *two-scale convergence* makes sense because of the following compactness theorem:

Theorem 2.3.3 (Compactness [2]). *For each bounded sequence u_ε in $L^2(\Omega)$. we can extract a subsequence, and there exists a limit $u_0(x,y) \in L^2(\Omega \times Y)$ such that this subsequence two-scale converges to u_0.*

We also have the following theorem about two-scale convergence and L^2 convergence:

Theorem 2.3.4 (L^2 convergence [2]). *Let (u_ε) be a sequence in $L^2(\Omega)$ which two-scale converges to $u_0 \in L^2(\Omega \times Y)$. Then, u_ε also converges to $u(x) = \int_Y u_0(x,y)\, dy$ in $L^2(\Omega)$ weakly and, we have*

$$\lim_{\varepsilon\to 0} \|u_\varepsilon\|_{L^2(\Omega)} \geq \|u_0\|_{L^2(\Omega\times Y)} \geq \|u\|_{L^2(\Omega)}. \tag{2.16}$$

Furthermore, if equality is achieved on the left part i.e.

$$\lim_{\varepsilon \to 0} \|u_\varepsilon\|_{L^2(\Omega)} = \|u_0\|_{L^2(\Omega \times Y)} \tag{2.17}$$

and if $u_0(x, y)$ is sufficiently smooth then

$$\lim_{\varepsilon \to 0} \left\| u_\varepsilon(x) - u_0\left(x, \frac{x}{\varepsilon}\right) \right\|_{L^2(\Omega \times Y)} = 0 \tag{2.18}$$

We have the following lemma:

Lemma 2.3.5 (Existence of a limit [2])**.** *Any function $u_0(x, y)$ in $L^2(\Omega \times Y)$ is attained as a two-scale limit.*

So far we have only considered bounded sequences in $L^2(\Omega)$, but we also have additional bounds on sequences of derivatives:

Proposition 2.3.6 (Bounds on derivatives [2])**.**

(i) Let u_ε be a bounded sequence in $H^1(\Omega)$ that converges weakly to a limit u in $H^1(\Omega)$. Then, u_ε two-scale converges to $u(x)$, and there exists a $u_1(x, y) \in L^2(\Omega; H^1_\#(Y)/\mathbb{R})$ such that, up to a subsequence, ∇u two-scale converges to $\nabla_x u(x) + \nabla_y u_1(x, y)$.

(ii) Let u and $\varepsilon \nabla u$ be two bounded sequences in $L^2(\Omega)$. Then, there exists a function $u_0(x, y)$ in $L^2(\Omega; H^1_\#(Y))$ such that, up to a subsequence, u and $\varepsilon \nabla u$ two-scale converge to $u_0(x, y)$ and $\nabla_y u_0(x, y)$, respectively.

(iii) Let u be a divergence-free bounded sequence in $[L^2(\Omega)]^N$, which two-scale converges to $u_0(x, y)$ in $[L^2(\Omega \times Y)]^N$. Then, the two-scale limit satisfies $div_y\, u_0(x, y) = 0$ and $\int_Y div_x\, u_0(x, y)\, dy = 0$.

Proposition 2.3.6 allows us to generalize theorems 2.3.2, 2.3.3, 2.3.4 and lemma 2.3.5 to bounded sequences in $L^p(\Omega)$, with $1 < p \leq \infty$.

2.3.2 Homogenization of linear second-order elliptic equations

In this section, we summarize some of Allaire's results [2] on two-scale convergence and homogenization of linear second-order elliptic equations with periodically oscillating coefficients. Let Ω be a bounded open set of $\mathbb{R}$ and let f be a given function in $L^2(\Omega)$. We consider the following linear second-order elliptic equation:

$$\begin{aligned} -\text{div}\left(A\left(x, \frac{x}{\varepsilon}\right)\nabla u_\varepsilon\right) &= f \quad \text{on } \Omega, \\ u_\varepsilon &= 0 \quad \text{on } \partial\Omega. \end{aligned} \tag{2.19}$$

Here, $A(x, y)$ defined on $\Omega \times Y$ is Y-periodic in y and elliptic, which means that for all $\xi \in \mathbb{R}^N$, there exist two positive constants $0 < \alpha \leq \beta$ satisfying,

$$\alpha|\xi|^2 \leq \sum_{i,j=1}^{N} A_{ij}(x, y)\xi_i\xi_j \leq \beta|\xi|^2.$$

We also require that $A_{ij}(x, y)$ is an admissible test function in the sense of definition 2.3.1:

$$\lim_{\varepsilon\to 0} \int_Y A_{ij}\left(x, \frac{x}{\varepsilon}\right)^2 \, \mathrm{d}y = \int_\Omega \int_Y A_{ij}(x, y)^2 \, \mathrm{d}x \, \mathrm{d}y.$$

Under these two assumptions, equation (2.19) admits a unique solution $u_\varepsilon \in H^1(\Omega)$, which satisfies the a priori estimate,

$$\|u_\varepsilon\|_{H^1(\Omega)} \leq C\|f\|_{L^2(\Omega)},$$

where C is a positive constant that depends only on Ω and α, and not on ε. Thus, there exists $u \in H^1(\Omega)$ such that, up to a subsequence, u_ε converges weakly to u in $H^1(\Omega)$. The homogenization of (2.19) amounts to finding the following *homogenized problem* that admits the limit u as its unique solution.

Definition 2.3.7 (Homogenized elliptic problem [2]). *The homogenized problem is defined as:*

$$\begin{aligned} -div\,[A^*(x)\nabla u(x)] &= f \quad in\ \Omega, \\ u &= 0 \quad on\ \partial\Omega. \end{aligned} \tag{2.20}$$

The entries of the matrix A^* are given by

$$A^*_{ij}(x) = \int_Y A(x,y)\big[\nabla_y w_i(x,y) + e_i\big] \cdot \big[\nabla_y w_j(x,y) + e_j\big]\, dy, \tag{2.21}$$

*and, for $i = 1, \ldots, N$, $w_i(x,y)$ is the solution of the **cell problem**:*

$$\begin{aligned} -div_y\big[A(x,y)(\nabla_y w_i(x,y) + e_i)\big] &= 0 \quad in\ Y, \\ y \to w_i(x,y) &\quad is\ Y\text{-}periodic. \end{aligned} \tag{2.22}$$

As a result of the cell problem, we have the following theorem:

Theorem 2.3.8 (Covergence of solutions [2]). *The sequence u_ε of solutions of* (2.19) *converges weakly in $H^1(\Omega)$ to the unique solution u of* (2.20).

This above theorem is established by introducing a *two-scale homogenized* problem, which is a combination of the homogenized problem (2.20) and the cell problem (2.22). The two-scale homogenized problem is a system of two equations with two unknowns, where the macroscopic and microscopic scales are mixed. It is equivalent to the homogenized system and the cell problem without any assumptions on the symmetry of the matrix A. The results summarized in 2.3.1 and the Lax-Millgram lemma are then applied to this two-scale homogenized problem to recover the convergence result in theorem 2.3.8.

2.3.3 Homogenization of time-harmonic Maxwell's equations

In this section, we review some homogenization results for time-harmonic Maxwell's equations with linear coefficients. Wellander introduced this theory for ε-periodic material

in 2001 [84] and expanded to the non-linear and fixed-frequency cases in [83, 85]. We adapt some of this theory to the time-harmonic equations and review some relevant asymptotic analysis [60]. Let us introduce the homogenized system [60],

Definition 2.3.9 (Homogenized system [60])**.**

$$\nabla \times \boldsymbol{\mathcal{E}} = i\omega\mu\boldsymbol{\mathcal{H}}, \qquad \nabla \times \boldsymbol{\mathcal{H}} = -i\omega\varepsilon^{\mathit{eff}}\boldsymbol{\mathcal{E}} + \boldsymbol{J}_a, \tag{2.23}$$

The heterogeneous permittivity and microscale inclusions have been replaced by the effective permittivity of the plasmonic crystal which is given by a uniform, frequency dependent permittivity tensor:

$$\varepsilon_{ij}^{\mathit{eff}}(\boldsymbol{x}) = \int_Y \varepsilon(\boldsymbol{x},\boldsymbol{y})(\boldsymbol{e}_j + \nabla\chi_j^{\,T}) \cdot (\boldsymbol{e}_i + \overline{\nabla\chi_i^{\,T}})\,\mathrm{d}y \\ - \frac{1}{i\omega}\int_\Sigma \sigma(\boldsymbol{x},\boldsymbol{y})(\boldsymbol{e}_{j\mathbf{t}} + \nabla_{\mathbf{t}}\chi_j^{\,T}) \cdot (\boldsymbol{e}_{i\mathbf{t}} + \overline{\nabla_{\mathbf{t}}\chi_i^{\,T}})\,\mathrm{d}o_y. \tag{2.24}$$

The corrector $\chi_i \in H := \left\{\varphi \in H^1_{per}(Y,\mathbb{C}),\ \nabla_{\mathbf{t}}\varphi \in \boldsymbol{L}^2(\Sigma,\mathbb{C})\right\}$, $i = 1,2,3$ *is given by an associated cell problem,*

$$\int_Y \varepsilon(\boldsymbol{x},\boldsymbol{y})(\boldsymbol{e}_i + \nabla\chi_i^{\,T}) \cdot \overline{\nabla\varphi^{\,T}}\,\mathrm{d}y \\ - \frac{1}{i\omega}\int_\Sigma \sigma(\boldsymbol{x},\boldsymbol{y})(\boldsymbol{e}_{i\mathbf{t}} + \nabla_{\mathbf{t}}\chi_i^{\,T}) \cdot \overline{\nabla_{\mathbf{t}}\varphi^{\,T}}\,\mathrm{d}o_y \;=\; 0 \quad \textit{for all } \varphi \in H. \tag{2.25}$$

Here, we have adopted the convention that the gradient is a row vector and $\boldsymbol{e}_i$ denotes the i-th (column) unit vector. The subscript $\mathbf{t}$ denotes projection onto the tangential plane of Σ, and $\bar{\cdot}$ denotes the complex conjugate of a complex-valued quantity. $H^1_{\mathrm{per}}(\Omega,\mathbb{C})$ denotes the Sobolev-space of all complex-valued square-integrable function with square-integrable partial derivatives defined on the unit cell Y that are periodic in all three space directions, $\varphi(\boldsymbol{y}) = \varphi(\boldsymbol{y} + \boldsymbol{e}_i)$ for $i = 1,2,3$ and for all $y \in Y$. Maier et al. present the following convergence theorem,

Theorem 2.3.10 (Convergence of solutions [60]). *Under the assumptions* (2.8), *for all* $\boldsymbol{J}_a \in L^2(\Omega;\mathbb{C}^3)$, *the electric field* $\boldsymbol{E}^d(\boldsymbol{x})$ *of* (2.12) *and the corresponding magnetic field* $\boldsymbol{H}^d(\boldsymbol{x})$ *converge weakly in* $L^2(\Omega;\mathbb{C}^3)$ *to functions* $\boldsymbol{\mathcal{E}}(\boldsymbol{x})$ *and* $\boldsymbol{\mathcal{H}}(\boldsymbol{x})$ *satisfying the following weak form of the homogenized system* (2.23)*:*

$$\boldsymbol{\mathcal{E}} \in X_0, \quad a_0(\boldsymbol{\mathcal{E}}, \boldsymbol{\Psi}) = \int_\Omega i\omega \boldsymbol{J}_a \cdot \boldsymbol{\Psi} \, \mathrm{d}x \quad \forall \boldsymbol{\Psi} \in X_0 \tag{2.26}$$

and

$$\boldsymbol{\mathcal{H}}(\boldsymbol{x}) = \frac{1}{i\omega\mu} \nabla \times \boldsymbol{\mathcal{E}}(\boldsymbol{x}).$$

Here, $a_0 : X_0 \times X_0 \to \mathbb{C}$ *is given by*

$$a_0(\boldsymbol{u}, \boldsymbol{v}) = \int_\Omega \frac{1}{\mu} (\nabla \times \boldsymbol{u}) \cdot (\nabla \times \boldsymbol{v}) \, \mathrm{d}x - \int_\Omega \frac{\omega^2}{\varepsilon^{\mathit{eff}}} \boldsymbol{u} \cdot \boldsymbol{v} \, \mathrm{d}x - \int_{\partial\Omega} i\omega\lambda \boldsymbol{u}_T \cdot \boldsymbol{v}_T \, d\sigma,$$

and the function space X_0 *is defined by*

$$X_0 = \left\{ \boldsymbol{u} \in H(\mathit{curl}; \Omega) \mid \boldsymbol{u}_T \in L^2(\partial\Omega; \mathbb{C}^3) \right\}.$$

The effective permittivity is the same as (2.24).

We also have the following well-posedness theorem:

Theorem 2.3.11 (Well-posedness of the homogenized system [60]). *Under the assumptions* (2.8), *the homogenized problem* (2.23) *has a unique solution* $\boldsymbol{\mathcal{E}}(\boldsymbol{x})$ *in* X_0 *for all* $\boldsymbol{J}_a \in L^2(\Omega;\mathbb{C}^3)$.

The proofs of theorems 2.3.10 and 2.3.11 are based on the notion of two-scale convergence presented in subsections 2.3.1 and 2.3.2. Here we summarize the proof of this theorem based on the two-scale convergence as presented by Maier et al. [60]. Let $\boldsymbol{E}^d(\boldsymbol{x})$ be the unique solution of (2.12) as established. We have a corresponding $\boldsymbol{H}^d(\boldsymbol{x})$ for $\boldsymbol{x} \in \Omega$. Proposition

2.2.2 implies that $\boldsymbol{H}_d \in L^2(\Omega;\mathbb{C}^3)$. The weak formulations are [60],

$$\int_\Omega \boldsymbol{E}^d \cdot (\nabla \times \boldsymbol{\Psi})\ \mathrm{d}x = i\omega\mu \int_\Omega \boldsymbol{H}^d \cdot \boldsymbol{\Psi}\ \mathrm{d}x \quad \forall \boldsymbol{\Psi} \in H_T(\mathrm{curl};\Omega) \tag{2.27}$$

$H_T(\mathrm{curl};\Omega) := \{\boldsymbol{u} \in H(\mathrm{curl};\Omega) \mid \boldsymbol{u}_T = 0 \text{ on } \partial\Omega\}$.

$$\begin{aligned}\int_\Omega \boldsymbol{H}^d \cdot (\nabla \times \boldsymbol{\Psi})\ \mathrm{d}x - \int_{\partial\Omega} \lambda \boldsymbol{E}^d \cdot \boldsymbol{\Psi}_T\, \mathrm{d}\sigma + \int_\Omega i\omega\varepsilon(\boldsymbol{x}, \boldsymbol{x}/d)\boldsymbol{E}^d \cdot \boldsymbol{\Psi}\ \mathrm{d}x \\ = d\int_{\Sigma_d} \sigma(\boldsymbol{x}, \boldsymbol{x}/d)(\boldsymbol{E}^d)^T \cdot \boldsymbol{\Psi}_T\, \mathrm{d}\sigma + \int_\Omega \boldsymbol{J}_a \cdot \boldsymbol{\Psi}\ \mathrm{d}x \quad \forall \boldsymbol{\Psi} \in X_d.\end{aligned} \tag{2.28}$$

Our goal is to pass to the limit $d \to 0$. We start with the following lemma.

Lemma 2.3.12 (Two-scale convergence [60])**.** *Up to a subsequence, the functions $\boldsymbol{E}^d(\boldsymbol{x})$ and $\boldsymbol{H}_d(\boldsymbol{x})$ two-scale converge to functions $\boldsymbol{E}^{(0)}(\boldsymbol{x},\boldsymbol{y})$ and $\boldsymbol{H}^{(0)}(\boldsymbol{x},\boldsymbol{y})$ in $L^2(\Omega; L^2(Y;\mathbb{C}^3))$ which satisfy*

$$\begin{cases} \boldsymbol{E}^{(0)}(\boldsymbol{x},\boldsymbol{y}) &= \boldsymbol{\mathcal{E}}(\boldsymbol{x}) + \nabla_{\boldsymbol{y}}\varphi(\boldsymbol{x},\boldsymbol{y}), \\ \boldsymbol{H}^{(0)}(\boldsymbol{x},\boldsymbol{y}) &= \boldsymbol{\mathcal{H}}(\boldsymbol{x}), \end{cases}$$

for some functions $\boldsymbol{\mathcal{E}}, \boldsymbol{\mathcal{H}} \in L^2(\Omega;\mathbb{C}^3)$ and $\varphi(\boldsymbol{x},\boldsymbol{y}) \in L^2(\Omega; H^1_\#(Y;\mathbb{C}))$.

The proof of this lemma uses the fact that $\boldsymbol{E}^d$ and $\boldsymbol{H}^d$ are bounded in $L^2(\Omega;\mathbb{C})$, and so we can apply Theorem 2.3.4 to conclude that there exist some subsequences that converge to $(\boldsymbol{E}^{(0)}, \boldsymbol{H}^{(0)})$. Using integration by parts and using the test function $\boldsymbol{\Psi}_d(\boldsymbol{x}) = dw(x)\boldsymbol{\Phi}(\boldsymbol{x}/d)$ with $\boldsymbol{\Phi} \in C^\infty_\#(Y;\mathbb{C}^3)$ and $w \in \mathcal{D}(\Omega)$. Passing to the limit in a way similar to section 2.3.2,

$$\int_\Omega w(x) \int_Y \boldsymbol{E}^{(0)}(\boldsymbol{x},\boldsymbol{y}) \cdot \nabla_{\boldsymbol{y}} \times \boldsymbol{\Phi}(\boldsymbol{y})\ \mathrm{d}y\ \mathrm{d}x = 0.$$

Similarly,

$$\int_\Omega w(x) \int_Y \boldsymbol{H}^{(0)}(\boldsymbol{x},\boldsymbol{y}) \cdot \nabla_{\boldsymbol{y}} \times \boldsymbol{\Phi}(\boldsymbol{y})\ \mathrm{d}y\ \mathrm{d}x = 0.$$

Using a result from Fourier analysis, we arrive at

$$\begin{cases} \boldsymbol{E}^{(0)}(\boldsymbol{x},\boldsymbol{y}) & = \boldsymbol{\mathcal{E}}(\boldsymbol{x}) + \nabla_{\boldsymbol{y}}\varphi(\boldsymbol{x},\boldsymbol{y}), \\ \boldsymbol{H}^{(0)}(\boldsymbol{x},\boldsymbol{y}) & = \boldsymbol{\mathcal{H}}(\boldsymbol{x}) + \nabla_{\boldsymbol{y}}\varphi_1(\boldsymbol{x},\boldsymbol{y}). \end{cases}$$

From here, the final result is derived using a different test function and the periodic boundary conditions. For more details, we refer the reader to [60]. We also refer the reader to [60] for the remaining lemmas that allow for the following theorem as $d \to 0$,

Theorem 2.3.13 (Well-posedness and two-scale convergence [5, 60])**.** *Let $\mu \in \mathbb{R}_{>0}$ and let $\varepsilon^d, \sigma^d \in L^\infty(Y, \mathbb{C}^{d\times d})$ be bounded, complex and tensor-valued functions such that $Im(\varepsilon^d(\mathbf{x}))$ and $Re(\sigma^d(\mathbf{x}))$ are symmetric and uniformly elliptic. Then, provided Σ is sufficiently smooth [5, 60],* (2.2) *&* (2.3)*,* (2.23)*, and* (2.25) *are well-posed, the solution* $(\boldsymbol{E}^d, \boldsymbol{H}^d)$ two-scale converges *to the solution* $(\boldsymbol{\mathcal{E}}, \boldsymbol{\mathcal{H}})$ *of the homogenized problem* (2.23)*.*

The proof of this theorem is not fully presented here and we refer the reader to [60] for a complete analysis. The main challenge with this proof is establishing,

$$\lim_{d\to 0} d \int_{\Sigma_d} (\boldsymbol{E}^d)^T \cdot \boldsymbol{\Psi}(\boldsymbol{x}, \boldsymbol{x}/d)\, \mathrm{d}o_y = \int_{\Omega}\int_{\Sigma} (\boldsymbol{\mathcal{E}}(\boldsymbol{x}) + \nabla_y\varphi(\boldsymbol{x},\boldsymbol{y})))^T \cdot \boldsymbol{\Psi}(\boldsymbol{x},\boldsymbol{y})\, \mathrm{d}o_y \mathrm{d}x$$

To solve this, we employ a similar asymptotic analysis as discussed above and the two-scale convergence theorems presented in section 2.3.1.

Remark 2.3.14. *The above theorem is, strictly speaking, a generalized version of what has been shown in [5, 60] where the material parameters ε^d and σ^d had been assumed to be scalar (and not tensor-valued coefficients). Proving the generalized statement, however, only requires minor adjustments to the proofs.*

3. DEFORMED CELL PROBLEM

We now introduce a deformation and a deformed cell problem. We adopt the notation that $\hat{\cdot}$ indicates that a function, coordinate or differential operator is on the reference configuration [75]. Let $\hat{Y}$ and $\hat{\Sigma}$ denote a given reference configuration consisting of the unit cell $\hat{Y} = [0,1]^3$ with given (two dimensional) inclusions $\hat{\Sigma}$. Let Y and Σ denote the deformed volume and inclusions. We assume that the deformed geometry is given by a deformation vector field $\hat{\boldsymbol{q}} \in \boldsymbol{D}(\hat{Y}, \hat{\Sigma})$ of the reference configuration [75],

$$\hat{\boldsymbol{q}} \ : \ \hat{Y} \ \to \mathbb{R}^3, \quad \text{such that} \quad \hat{Y} \ni \hat{\boldsymbol{y}} \ \leftrightarrow \ \boldsymbol{y}(\hat{\boldsymbol{y}}) := \hat{\boldsymbol{y}} + \hat{\boldsymbol{q}}(\hat{\boldsymbol{y}}) \in Y. \tag{3.1}$$

We also assume that $\hat{\boldsymbol{q}}$ is a diffeomorphism that also maps $\hat{\Sigma}$ onto Σ bijectively. Figure 3.1 is an example of how such a coordinate transformation would play out in a unit cell with a graphene inclusion. Note that here, in analogy to the function space H we have introduced,

$$\boldsymbol{D}(\hat{Y}, \hat{\Sigma}) := \big\{ \hat{\boldsymbol{\varphi}} \in \boldsymbol{W}_0^{1,\infty}(\hat{Y}) : \ \hat{\boldsymbol{\tau}}_k \cdot \hat{\nabla} \hat{\boldsymbol{\varphi}} \in L^\infty(\hat{\Sigma}),\, k = 1, 2 \big\}. \tag{3.2}$$

$W_0^{1,\infty}(\hat{Y})$ shall denotes the Sobolev space of all functions $\varphi \in W_0^{1,\infty}(\hat{Y})$ with vanishing trace on $\partial \hat{Y}$.

Remark 3.0.1. *We note that $\hat{\boldsymbol{q}} \in \boldsymbol{D}(\hat{Y}, \hat{\Sigma})$ implies that $\hat{\boldsymbol{q}}$ is already Lipschitz continuous. This implies that the trace of $\hat{\boldsymbol{q}}$ onto Σ and $\partial\Omega$ is well defined and also Lipschitz continuous. Strictly speaking, this renders the condition $\hat{\boldsymbol{\tau}}_k \cdot \hat{\nabla} \hat{\boldsymbol{\varphi}} \in L^\infty(\hat{\Sigma})$ superfluous.*

Now, we introduce a series of definitions and rules that are neccessary for the formulation of the transformed cell problem.

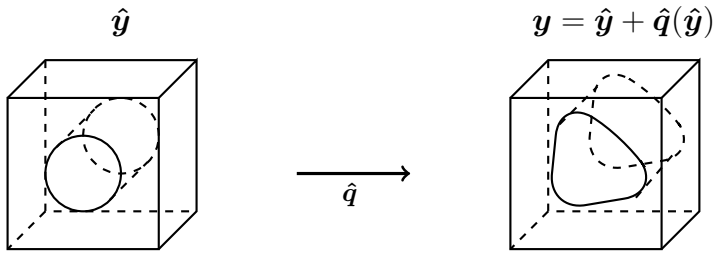

Figure 3.1: The reference configuration of a unit cell $\hat{Y}$ with a graphene inclusion $\hat{\Sigma}$ being transformed by a deformation $\hat{\boldsymbol{q}}$ into a deformed configuration Y, Σ.

3.1 Definitions and transformation rules

Definition 3.1.1. *The* transformation gradient $\hat{F}(\hat{\boldsymbol{y}})$ *and determinant* $\hat{J}$ *are given by,*

$$\hat{F}(\hat{\boldsymbol{y}}) \;:=\; \boldsymbol{I} + \hat{\nabla}\hat{\boldsymbol{q}}(\hat{\boldsymbol{y}}), \qquad \hat{J}(\hat{\boldsymbol{y}}) \;:=\; \det\big(\hat{F}(\hat{\boldsymbol{y}})\big). \tag{3.3}$$

Here, we have adopted the convention that $\big(\hat{\nabla}\hat{\boldsymbol{q}}\big)_{ij} = \frac{\partial}{\partial \hat{y}_j}\hat{q}_i$ and $\boldsymbol{I}$ denotes the unit matrix. We then have a few lemmas that provide the transformation rules. The proof of these lemmas are adapted from similar results presented by Richter for the case of fluids [75].

Lemma 3.1.2 (Transformation of gradients)**.** *Let* $\hat{\varphi}(\hat{\boldsymbol{y}})$ *be a differentiable function defined on* $\hat{Y}$ *and let* $\varphi(\boldsymbol{y}) \;:\; Y \to \mathbb{R}$ *be defined by setting* $\varphi(\boldsymbol{y}) := \hat{\varphi}(\hat{\boldsymbol{y}}(\boldsymbol{y}))$*. Then,*

$$\nabla\varphi(\boldsymbol{y})^T \;=\; \hat{F}(\hat{\boldsymbol{y}})^{-T}\hat{\nabla}\hat{\varphi}(\hat{\boldsymbol{y}})^T. \tag{3.4}$$

Proof. We know that $\boldsymbol{y}(\hat{\boldsymbol{y}}) = \hat{\boldsymbol{y}} + \hat{\boldsymbol{q}}(\hat{\boldsymbol{y}})$. Then,

$$\hat{\partial}_i\hat{\varphi}(\hat{\boldsymbol{y}})^T = \hat{\partial}_i\varphi(\boldsymbol{y}(\hat{\boldsymbol{y}}))^T = \sum_i \partial_i\varphi(\boldsymbol{y}(\hat{\boldsymbol{y}}))^T\hat{\partial}_i\boldsymbol{y}^j(\hat{\boldsymbol{y}}) = \sum_i \partial_i\varphi(\boldsymbol{y})^T\hat{F}_{ij}(\hat{\boldsymbol{y}}).$$

Hence,

$$\hat{\nabla}\hat{\varphi}(\hat{\boldsymbol{y}})^T = \hat{F}(\hat{\boldsymbol{y}})^T \nabla\varphi(\boldsymbol{y})^T \implies \nabla\varphi(\boldsymbol{y})^T = \hat{F}(\hat{\boldsymbol{y}})^{-T}\hat{\nabla}\hat{\varphi}(\hat{\boldsymbol{y}})^T.$$

□

We note here that the lemma uses $\varphi(\boldsymbol{y})^T$ instead of $\varphi(\boldsymbol{y})$ due to the way gradients appear in the effective permittivity tensor (2.24) and cell problem (2.25). Let us define the rules on the tangents and normals.

Lemma 3.1.3 (Transformation of tangents and normals)**.** *Let $\hat{\boldsymbol{\nu}}$ be a (unit) normal field on $\hat{\Sigma}$ and let $\hat{\boldsymbol{\tau}}_1$, $\hat{\boldsymbol{\tau}}_2$ be two orthonormal (unit) tangential fields. Then,*

$$\boldsymbol{\nu} = \hat{F}(\hat{\boldsymbol{y}})^{-T}\hat{\boldsymbol{\nu}}/\|\hat{F}(\hat{\boldsymbol{y}})^{-T}\hat{\boldsymbol{\nu}}\|_{\ell^2}, \quad \boldsymbol{\tau}_i = \hat{F}(\hat{\boldsymbol{y}})\hat{\boldsymbol{\tau}}_i/\|\hat{F}(\hat{\boldsymbol{y}})\hat{\boldsymbol{\tau}}_i\|_{\ell^2},\ i = 1, 2.$$

are a (unit) normal field and orthonormal tangential fields on Σ.

Proof. The transformation of the unit normal $\boldsymbol{\nu}$ is a direct consequence of *Nanson's formula*, which is a fundamental relation in continuum mechanics that links differential areas in the reference (undeformed) configuration and the current (deformed) configuration through the deformation gradient. We refer the reader to [73, p. 61] for details. The tangent transformations are derived using orthonormality of $\boldsymbol{\tau}_i$ and $\boldsymbol{\nu}$ and the transformation for $\boldsymbol{\nu}$. □

Lemma 3.1.4 (Transformation of volume and area elements)**.** *With the definitions presented above, we also have:*

$$\mathrm{d}y \;=\; \hat{J}\,\mathrm{d}\hat{y}, \qquad\qquad \mathrm{d}o_y \;=\; \|\hat{F}(\hat{\boldsymbol{y}})^{-T}\hat{\boldsymbol{\nu}}\|_{\ell^2}\hat{J}\,\mathrm{d}\hat{o}_{\hat{y}}. \tag{3.5}$$

Proof. The transformation formula for $\mathrm{d}y$ is a simple substitution $\hat{\boldsymbol{y}}$ into the unit integral:

$$\int_Y 1\,\mathrm{d}y = \int_{\hat{Y}} \det(\,\boldsymbol{I} + \hat{\nabla}\hat{\boldsymbol{q}}(\hat{\boldsymbol{y}}))\,\mathrm{d}\hat{y} = \int_{\hat{Y}} \hat{J}\,\mathrm{d}\hat{y}.$$

As for $\mathrm{d}o_y$, this is the *Nanson's formula* and we once again refer the reader to [73, p. 61] for the complete proof. □

Lemma 3.1.5. *In the setting of Lemmas 3.1.2 and 3.1.3 we have the identity*

$$\nabla_{\mathbf{t}}\varphi \;=\; \sum_k \boldsymbol{\tau}_k\boldsymbol{\tau}_k^T(\hat{F}(\hat{\boldsymbol{y}})^{-T}\hat{\nabla}\hat{\varphi}) \;=\; \sum_k \frac{\hat{F}(\hat{\boldsymbol{y}})\hat{\boldsymbol{\tau}}_k}{\|\hat{F}(\hat{\boldsymbol{y}})\hat{\boldsymbol{\tau}}_k\|_{\ell^2}^2}\,\hat{\boldsymbol{\tau}}_k\cdot\hat{\nabla}\hat{\varphi}.$$

Proof. The statement is a direct consequence of Lemmas 3.1.2 and 3.1.3 and the fact that,

$$\nabla_{\mathbf{t}}\varphi = \sum_k \boldsymbol{\tau}_k\boldsymbol{\tau}_k^T\nabla\varphi.$$

□

We are now prepared to define the transformed effective permittivity tensor and the deformed cell problem.

3.2 Transformed ε^{eff} and deformed cell problem

We are now in a position to recast (2.24) and (2.25) from definition 2.3.9 in reference coordinates. We introduce the function space,

$$\boldsymbol{H}(\hat{Y},\hat{\Sigma}) := \big\{\hat{\boldsymbol{\varphi}}\in\boldsymbol{H}^1_{\text{per}}(\hat{Y},\mathbb{C}) \;:\; \hat{\boldsymbol{\tau}}_k\cdot\hat{\nabla}\hat{\boldsymbol{\varphi}}\in L^2(\hat{\Sigma},\mathbb{C}^{d\times d}),\, k=1,2\big\}.$$

Definition 3.2.1. *The effective permittivity tensor in the reference coordinates is given by*

$$\begin{aligned}\varepsilon_{ij}^{\mathit{eff}}(\hat{\boldsymbol{\chi}};\hat{\boldsymbol{q}}) = \int_{\hat{Y}} \varepsilon(\boldsymbol{x},\boldsymbol{y}(\hat{\boldsymbol{y}}))(\boldsymbol{e}_j+\hat{F}(\hat{\boldsymbol{y}})^{-T}\hat{\nabla}\hat{\chi}_j^{\,T})\cdot(\boldsymbol{e}_i+\hat{F}(\hat{\boldsymbol{y}})^{-T}\overline{\hat{\nabla}\hat{\chi}_i^{\,T}})\hat{J}\,\mathrm{d}\hat{y}\\ -\frac{1}{i\omega}\int_{\hat{\Sigma}}\sigma(\boldsymbol{x},\boldsymbol{y}(\hat{\boldsymbol{y}}))\Big(\boldsymbol{e}_{j_{\mathbf{t}}}+\sum_k\boldsymbol{\tau}_k\boldsymbol{\tau}_k^T\hat{F}(\hat{\boldsymbol{y}})^{-T}\hat{\nabla}\hat{\boldsymbol{\chi}}_j^{\,T}\Big)\\ \cdot\Big(\boldsymbol{e}_{i\mathbf{t}}+\sum_k\boldsymbol{\tau}_k\boldsymbol{\tau}_k^T\hat{F}(\hat{\boldsymbol{y}})^{-T}\overline{\hat{\nabla}\hat{\boldsymbol{\chi}}_i^{\,T}}\Big)\|\hat{F}(\hat{\boldsymbol{y}})^{-T}\hat{\boldsymbol{\nu}}\|_{\ell^2}\hat{J}\,\mathrm{d}\hat{o}_{\hat{y}}. \quad (3.6)\end{aligned}$$

and the corrector $\hat{\boldsymbol{\chi}} = \big(\hat{\chi}_i\big)_{i=1}^3 \in \boldsymbol{H}(\hat{Y}, \hat{\Sigma})$ *is determined by,*

$$E(\hat{\boldsymbol{\chi}}, \hat{\boldsymbol{\varphi}}; \hat{\boldsymbol{q}}) \;=\; 0 \quad \textit{for all } \hat{\boldsymbol{\varphi}} \in \boldsymbol{H}(\hat{Y}, \hat{\Sigma}), \tag{3.7}$$

where,

$$\begin{aligned} E(\hat{\boldsymbol{\chi}}, \hat{\boldsymbol{\varphi}}; \hat{\boldsymbol{q}}) := \int_{\hat{Y}} \varepsilon(\boldsymbol{x}, \boldsymbol{y}(\hat{\boldsymbol{y}}))(\boldsymbol{I} + \hat{F}(\hat{\boldsymbol{y}})^{-T}\hat{\nabla}\hat{\boldsymbol{\chi}}^{\,T}) \cdot (\hat{F}(\hat{\boldsymbol{y}})^{-T}\overline{\hat{\nabla}\hat{\boldsymbol{\varphi}}^{\,T}})\hat{J}\,\mathrm{d}\hat{y} \\ - \frac{1}{i\omega}\int_{\hat{\Sigma}} \sigma(\boldsymbol{x}, \boldsymbol{y}(\hat{\boldsymbol{y}}))\Big(\sum_k \boldsymbol{\tau}_k\boldsymbol{\tau}_k^T\big(\boldsymbol{I} + \hat{F}(\hat{\boldsymbol{y}})^{-T}\hat{\nabla}\hat{\boldsymbol{\chi}}^{\,T}\big)\Big) \\ \cdot \Big(\sum_k \boldsymbol{\tau}_k\boldsymbol{\tau}_k^T\hat{F}(\hat{\boldsymbol{y}})^{-T}\overline{\hat{\nabla}\hat{\boldsymbol{\varphi}}^{\,T}}\Big)\|\hat{F}(\hat{\boldsymbol{y}})^{-T}\hat{\boldsymbol{\nu}}\|_{\ell^2}\hat{J}\,\mathrm{d}\hat{o}_{\hat{y}}. \end{aligned} \tag{3.8}$$

Here, $\boldsymbol{I}$ is the unit matrix. We note that $\sigma(\boldsymbol{x}, \boldsymbol{y}(\hat{\boldsymbol{y}}))$ and $\varepsilon(\boldsymbol{x}, \boldsymbol{y}(\hat{\boldsymbol{y}}))$, still denote tensors acting on gradients in transformed (non-reference) coordinates.

Before we move on to well-posedness and regularity of our problem, we introduce two transformed tensors:

$$\begin{gathered} \hat{\varepsilon}(\boldsymbol{x}, \hat{\boldsymbol{y}}) := \hat{F}(\hat{\boldsymbol{y}})^{-1}\varepsilon(\boldsymbol{x}, \boldsymbol{y}(\hat{\boldsymbol{y}}))\hat{F}(\hat{\boldsymbol{y}})^{-T}\hat{J}, \quad \hat{\sigma}(\boldsymbol{x}, \hat{\boldsymbol{y}}) := \sum_{mn} \hat{\sigma}_{mn}\,\hat{\boldsymbol{\tau}}_m\hat{\boldsymbol{\tau}}_n^T, \\ \text{where} \quad \hat{\sigma}_{mn} := \frac{\sigma_{mn}(\boldsymbol{x}, \boldsymbol{y}(\hat{\boldsymbol{y}}))\|\hat{F}(\hat{\boldsymbol{y}})^{-T}\hat{\boldsymbol{\nu}}\|_{\ell^2}\hat{J}}{\|\hat{F}(\hat{\boldsymbol{y}})\hat{\boldsymbol{\tau}}_m\|_{\ell^2}^2\|\|\hat{F}(\hat{\boldsymbol{y}})\hat{\boldsymbol{\tau}}_n\|_{\ell^2}^2}, \end{gathered} \tag{3.9}$$

and σ_{mn} is defined by $\sigma(\boldsymbol{x}, \boldsymbol{y}(\hat{\boldsymbol{y}})) =: \sum_{mn}\sigma_{mn}\,\boldsymbol{\tau}_m\boldsymbol{\tau}_n^T$. We make the following observations:

Lemma 3.2.2 (Boundedness of the tensors (3.9))**.** *Assume that* $\hat{\boldsymbol{q}}(\hat{\boldsymbol{y}}) \in \boldsymbol{D}(\hat{Y}, \hat{\Sigma})$ *and* $0 < \delta \leq \hat{J}(\hat{\boldsymbol{y}})$ *is uniformly bounded. Then, the tensors* $\hat{\varepsilon}(\hat{\boldsymbol{y}})$ *and* $\hat{\sigma}(\hat{\boldsymbol{y}})$ *are bounded, complex and tensor-valued functions and* $\mathrm{Re}\,(\hat{\varepsilon}(\hat{\boldsymbol{y}}))$ *and* $Im(\hat{\sigma}(\hat{\boldsymbol{y}}))$ *are symmetric,* $Im(\hat{\varepsilon}(\hat{\boldsymbol{y}}))$ *and* $Re(\hat{\sigma}(\hat{\boldsymbol{y}}))$ *are symmetric and uniformly elliptic with a constant depending on* δ*.*

Proof. We know that $\hat{\boldsymbol{q}}(\hat{\boldsymbol{y}}) \in \boldsymbol{D}(\hat{Y}, \hat{\Sigma})$ implying that $\hat{J}$ and $F(\hat{\boldsymbol{y}})$ are bounded with respect to $\|.\|_{L^\infty}$. Moreover, $\varepsilon(\boldsymbol{x}, \boldsymbol{y}(\hat{\boldsymbol{y}})), \sigma(\boldsymbol{x}, \boldsymbol{y}(\hat{\boldsymbol{y}}))$ are bounded, complex and tensor valued by assumption. Therefore, $\hat{\varepsilon}(\boldsymbol{x}, \hat{\boldsymbol{y}})$ and $\hat{\sigma}(\boldsymbol{x}, \hat{\boldsymbol{y}})$ are by construction also bounded, complex

and tensor valued. Simultaneous multiplication by a tensor from the left and its transpose from the right preserves symmetry, and so does scaling and multiplication by $\hat{J}$. Therefore, $\operatorname{Re}\hat{\varepsilon}(\boldsymbol{x},\hat{\boldsymbol{y}})$, $\operatorname{Im}\hat{\varepsilon}(\boldsymbol{x},\hat{\boldsymbol{y}})$, $\operatorname{Re}\hat{\sigma}(\boldsymbol{x},\hat{\boldsymbol{y}})$, and $\operatorname{Im}\hat{\sigma}(\boldsymbol{x},\hat{\boldsymbol{y}})$ are symmetric owing to the symmetry of $\varepsilon(\boldsymbol{x},\boldsymbol{y})$ and $\sigma(\boldsymbol{x},\boldsymbol{y})$. Similarly, the uniform ellipticity of $\operatorname{Im}\hat{\varepsilon}(\boldsymbol{x},\hat{\boldsymbol{y}})$ and $\operatorname{Re}\hat{\sigma}(\boldsymbol{x},\hat{\boldsymbol{y}})$ is a direct consequence of the uniform ellipticity of $\operatorname{Im}\varepsilon(\boldsymbol{x},\boldsymbol{y})$ and $\operatorname{Re}\sigma(\boldsymbol{x},\boldsymbol{y})$ and the uniform lower bound on the determinant of the deformation gradient: $0<\delta<\hat{J}(\hat{\boldsymbol{y}})$. □

Using the transformed tensors, we have the following transformed system:

Lemma 3.2.3 (Equivalence of the problems)**.** *The bilinear term* (3.8) *can be equivalently written as follows:*

$$E(\hat{\boldsymbol{\chi}},\hat{\boldsymbol{\varphi}};\hat{\boldsymbol{q}}) := \int_{\hat{Y}} \hat{\varepsilon}(\boldsymbol{x},\hat{\boldsymbol{y}})\big(\hat{F}(\hat{\boldsymbol{y}})^T + \hat{\nabla}\hat{\boldsymbol{\chi}}^T\big)\cdot\overline{\hat{\nabla}\hat{\boldsymbol{\varphi}}^T}\,\mathrm{d}\hat{y} - \frac{1}{i\omega}\int_{\hat{\Sigma}} \hat{\sigma}(\boldsymbol{x},\hat{\boldsymbol{y}})\big((\hat{F}(\hat{\boldsymbol{y}})^T)_{\hat{\mathfrak{t}}} + \hat{\nabla}_{\hat{\mathfrak{t}}}\hat{\boldsymbol{\chi}}^T\big)\cdot\overline{\hat{\nabla}_{\hat{\mathfrak{t}}}\hat{\boldsymbol{\varphi}}^T}\,\mathrm{d}\hat{o}_{\hat{y}}. \quad (3.10)$$

Similarly, (3.6) *takes the form:*

$$\varepsilon^{\mathit{eff}}_{ij}(\hat{\boldsymbol{\chi}};\hat{\boldsymbol{q}}) = \int_{\hat{Y}} \hat{\varepsilon}(\boldsymbol{x},\hat{\boldsymbol{y}})\big(\hat{F}(\hat{\boldsymbol{y}})^T\boldsymbol{e}_j + \hat{\nabla}\hat{\boldsymbol{\chi}}_j^T\big)\cdot\big(\hat{F}(\hat{\boldsymbol{y}})^T\boldsymbol{e}_i + \overline{\hat{\nabla}\hat{\boldsymbol{\chi}}_i^T}\big)\,\mathrm{d}\hat{y} - \frac{1}{i\omega}\int_{\hat{\Sigma}} \hat{\sigma}(\boldsymbol{x},\hat{\boldsymbol{y}})\big((\hat{F}(\hat{\boldsymbol{y}})^T\boldsymbol{e}_j)_{\hat{\mathfrak{t}}} + \hat{\nabla}_{\hat{\mathfrak{t}}}\hat{\boldsymbol{\chi}}_j^T\big)\cdot\big((\hat{F}(\hat{\boldsymbol{y}})^T\boldsymbol{e}_i)_{\hat{\mathfrak{t}}} + \overline{\hat{\nabla}_{\hat{\mathfrak{t}}}\hat{\boldsymbol{\chi}}_i^T}\big)\,\mathrm{d}\hat{o}_{\hat{y}}. \quad (3.11)$$

Proof. We start with (3.8). Substituting σ_{mn} given in (3.9) and using Lemma 3.1.5 for transforming $\boldsymbol{\tau}_m$ and $\boldsymbol{\tau}_n$ gives:

$$\begin{aligned} E(\hat{\boldsymbol{\chi}},\hat{\boldsymbol{\varphi}};\hat{\boldsymbol{q}}) = \int_{\hat{Y}} \varepsilon(\boldsymbol{x},\boldsymbol{y}(\hat{\boldsymbol{y}}))(\hat{F}(\hat{\boldsymbol{y}})^{-T}\hat{F}(\hat{\boldsymbol{y}})^T + \hat{F}(\hat{\boldsymbol{y}})^{-T}\hat{\nabla}\hat{\boldsymbol{\chi}}^T)\cdot(\hat{F}(\hat{\boldsymbol{y}})^{-T}\overline{\hat{\nabla}\hat{\boldsymbol{\varphi}}^T})\hat{J}\,\mathrm{d}\hat{y} \\ - \frac{1}{i\omega}\sum_{m,n}\int_{\hat{\Sigma}} \sigma_{mn}\Big(\frac{\hat{F}(\hat{\boldsymbol{y}})\hat{\boldsymbol{\tau}}_m}{\|\hat{F}(\hat{\boldsymbol{y}})\hat{\boldsymbol{\tau}}_m\|}\cdot\big(\hat{F}(\hat{\boldsymbol{y}})^{-T}\hat{F}(\hat{\boldsymbol{y}})^T + \hat{F}(\hat{\boldsymbol{y}})^{-T}\hat{\nabla}\hat{\boldsymbol{\chi}}^T\big)\Big) \\ \cdot\Big(\frac{\hat{F}(\hat{\boldsymbol{y}})\hat{\boldsymbol{\tau}}_n}{\|\hat{F}(\hat{\boldsymbol{y}})\hat{\boldsymbol{\tau}}_n\|}\cdot\hat{F}(\hat{\boldsymbol{y}})^{-T}\overline{\hat{\nabla}\hat{\boldsymbol{\varphi}}^T}\Big)\|\hat{F}(\hat{\boldsymbol{y}})^{-T}\hat{\boldsymbol{\nu}}\|_{\ell^2}\hat{J}\,\mathrm{d}\hat{o}_{\hat{y}}. \end{aligned}$$

After some more simplifications and using the definitions of $\hat{\varepsilon}(\boldsymbol{x}, \hat{\boldsymbol{y}})$ and $\hat{\sigma}_{mn}$ from equation (3.9):

$$\begin{aligned} E(\hat{\boldsymbol{\chi}}, \hat{\boldsymbol{\varphi}}; \hat{\boldsymbol{q}}) = \int_{\hat{Y}} \hat{\varepsilon}(\boldsymbol{x}, \hat{\boldsymbol{y}})(\hat{F}(\hat{\boldsymbol{y}})^T + \hat{\nabla}\hat{\boldsymbol{\chi}}^T) \cdot (\overline{\hat{\nabla}\hat{\boldsymbol{\varphi}}^T})\hat{J}\,\mathrm{d}\hat{y} \\ - \frac{1}{i\omega} \sum_{m,n} \int_{\hat{\Sigma}} \hat{\sigma}_{mn}\Big(\hat{\boldsymbol{\tau}}_m \cdot (\hat{F}(\hat{\boldsymbol{y}})^T + \hat{\nabla}\hat{\boldsymbol{\chi}}^T)\Big) \\ \Big(\hat{\boldsymbol{\tau}}_n \cdot \overline{\hat{\nabla}\hat{\boldsymbol{\varphi}}^T}\Big) \|\hat{F}(\hat{\boldsymbol{y}})^{-T}\hat{\boldsymbol{\nu}}\|_{\ell^2} \hat{J}\,\mathrm{d}\hat{o}_{\hat{y}} = 0. \end{aligned}$$

Now using the definition for $\hat{\sigma}(\boldsymbol{x}, \hat{\boldsymbol{y}})$ given in (3.9) yields (3.10). Equation (3.6) can be transformed into (3.11) in a similar fashion. □

So, our final transformed problem is defined as follows:

Definition 3.2.4 (Transformed homogenized system)**.** *The effective permittivity tensor in the reference coordinates is given by*

$$\begin{aligned} \varepsilon_{ij}^{\mathit{eff}}(\hat{\boldsymbol{\chi}}; \hat{\boldsymbol{q}}) = \int_{\hat{Y}} \hat{\varepsilon}(\boldsymbol{x}, \hat{\boldsymbol{y}})\big(\hat{F}(\hat{\boldsymbol{y}})^T\boldsymbol{e}_j + \hat{\nabla}\hat{\boldsymbol{\chi}}_j^T\big) \cdot \big(\hat{F}(\hat{\boldsymbol{y}})^T\boldsymbol{e}_i + \overline{\hat{\nabla}\hat{\boldsymbol{\chi}}_i^T}\big)\,\mathrm{d}\hat{y} \\ - \frac{1}{i\omega} \int_{\hat{\Sigma}} \hat{\sigma}(\boldsymbol{x}, \hat{\boldsymbol{y}})\big((\hat{F}(\hat{\boldsymbol{y}})^T\boldsymbol{e}_j)_{\hat{\mathbf{t}}} + \hat{\nabla}_{\hat{\mathbf{t}}}\hat{\boldsymbol{\chi}}_j^T\big) \cdot \big((\hat{F}(\hat{\boldsymbol{y}})^T\boldsymbol{e}_i)_{\hat{\mathbf{t}}} + \overline{\hat{\nabla}_{\hat{\mathbf{t}}}\hat{\boldsymbol{\chi}}_i^T}\big)\,\mathrm{d}\hat{o}_{\hat{y}}. \end{aligned}$$

and the corrector $\hat{\boldsymbol{\chi}} = \big(\hat{\chi}_i\big)_{i=1}^3 \in \boldsymbol{H}(\hat{Y}, \hat{\Sigma})$ *is determined by*

$$E(\hat{\boldsymbol{\chi}}, \hat{\boldsymbol{\varphi}}; \hat{\boldsymbol{q}}) \;=\; 0 \quad \textit{for all } \hat{\boldsymbol{\varphi}} \in \boldsymbol{H}(\hat{Y}, \hat{\Sigma}),$$

where,

$$\begin{aligned} E(\hat{\boldsymbol{\chi}}, \hat{\boldsymbol{\varphi}}; \hat{\boldsymbol{q}}) := \int_{\hat{Y}} \hat{\varepsilon}(\boldsymbol{x}, \hat{\boldsymbol{y}})\big(\hat{F}(\hat{\boldsymbol{y}})^T + \hat{\nabla}\hat{\boldsymbol{\chi}}^T\big) \cdot \overline{\hat{\nabla}\hat{\boldsymbol{\varphi}}^T}\,\mathrm{d}\hat{y} \\ - \frac{1}{i\omega} \int_{\hat{\Sigma}} \hat{\sigma}(\boldsymbol{x}, \hat{\boldsymbol{y}})\big((\hat{F}(\hat{\boldsymbol{y}})^T)_{\hat{\mathbf{t}}} + \hat{\nabla}_{\hat{\mathbf{t}}}\hat{\boldsymbol{\chi}}^T\big) \cdot \overline{\hat{\nabla}_{\hat{\mathbf{t}}}\hat{\boldsymbol{\varphi}}^T}\,\mathrm{d}\hat{o}_{\hat{y}}. \end{aligned}$$

3.3 Well-posedness and regularity

To set up for shape optimization, we prove that our problem 3.2.4 is well-posed.

Theorem 3.3.1 (Well-posedness)**.** *Under the assumptions on the deformation field $\hat{\boldsymbol{q}}(\hat{\boldsymbol{y}})$ as stated in Lemma 3.2.2 problem* (3.7) *is well-posed.*

Proof. Lemma 3.1.5 ensures that equation (3.7) is the same as (2.25) with modified material tensors and a modified forcing. Lemma 3.2.2 ensures that all assumptions on the material tensors stated in Theorem 2.3.13 hold true. Well-posedness is thus an immediate consequence of Theorem 2.3.13. □

We now introduce a some regularity and robustness results that will be used later to justify the optimization approach.

Theorem 3.3.2 (A priori estimate)**.** *For the unique solution $\hat{\boldsymbol{\chi}} \in \boldsymbol{H}(\hat{Y}, \hat{\Sigma})$ to* (3.7)*, we have the following a priori estimate:*

$$\begin{aligned}\|\hat{\nabla}\hat{\boldsymbol{\chi}}\|^2_{L^2(\hat{Y})} + \frac{1}{\omega}\|\hat{\nabla}_{\hat{\mathbf{t}}}\hat{\boldsymbol{\chi}}\|^2_{L^2(\hat{\Sigma})} \\ \leq C\left(\|\hat{\varepsilon}(\boldsymbol{x},\hat{\boldsymbol{y}})\|^2_{L^\infty(\hat{Y})}\|\hat{F}^T\|^2_{L^2(\hat{Y})} + \frac{1}{\omega}\|\hat{\sigma}(\boldsymbol{x},\hat{\boldsymbol{y}})\|^2_{L^\infty(\hat{\Sigma})}\|\hat{F}^T\|^2_{L^2(\hat{\Sigma})}\right)\end{aligned}$$

for a constant $C > 0$ only depending on $\hat{\Sigma}$ and the lower bound δ of $\hat{J}(\hat{\boldsymbol{x}})$ as defined in Lemma 3.2.2.

Proof. The statement is a consequence of Lemmas 3.2.2 and 3.2.3. We start by testing (3.10) with $\hat{\boldsymbol{\varphi}} = \overline{\hat{\boldsymbol{\chi}}(\hat{\boldsymbol{q}})}$ and taking the imaginary part. Recalling that $\operatorname{Re}\hat{\varepsilon}$, $\operatorname{Im}\hat{\varepsilon}$, $\operatorname{Re}\hat{\sigma}$, $\operatorname{Im}\hat{\sigma}$ are symmetric by virtue of Lemma 3.2.2 we arrive at

$$\begin{aligned}\int_{\hat{Y}} \operatorname{Im}\hat{\varepsilon}\,\hat{\nabla}\hat{\boldsymbol{\chi}}^T \cdot \overline{\hat{\nabla}\hat{\boldsymbol{\chi}}^T}\,\mathrm{d}\hat{y} + \frac{1}{\omega}\int_{\hat{\Sigma}} \operatorname{Re}\hat{\sigma}\,\hat{\nabla}_{\hat{\mathbf{t}}}\hat{\boldsymbol{\chi}}^T \cdot \overline{\hat{\nabla}_{\hat{\mathbf{t}}}\hat{\boldsymbol{\chi}}^T}\,\mathrm{d}\hat{o}_{\hat{y}} \\ = -\operatorname{Im}\Big\{\int_{\hat{Y}} \hat{\varepsilon}\left(\hat{F}(\hat{\boldsymbol{y}})^T\right) \cdot \overline{\hat{\nabla}\hat{\boldsymbol{\chi}}^T}\,\mathrm{d}\hat{y} + \frac{1}{\mathrm{i}\omega}\int_{\hat{\Sigma}} \hat{\sigma}\left(\hat{F}(\hat{\boldsymbol{y}})^T\right)_{\hat{\mathbf{t}}} \cdot \overline{\hat{\nabla}_{\hat{\mathbf{t}}}\hat{\boldsymbol{\chi}}^T}\,\mathrm{d}\hat{o}_{\hat{y}}\Big\}.\end{aligned}$$

The statement now follows from using Young's inequality for both terms on the right side and uniform ellipticity of $\operatorname{Im}\hat{\varepsilon}$ and $\operatorname{Re}\hat{\sigma}$ with a δ-dependent constant that was established in Lemma 3.2.2. □

Theorem 3.3.3 (Bounds on second derivatives)**.** *Let $\hat{\Sigma}$ be a smooth, closed hypersurface, i. e., $\partial\hat{\Sigma} = 0$. Suppose there exist a smooth, $\hat{Y}$-periodic extensions $\hat{\boldsymbol{\tau}}_i(\boldsymbol{x}) : \hat{Y} \to \mathbb{R}^n$ of the tangential fields $\hat{\boldsymbol{\tau}}_i$ with $|\hat{\boldsymbol{\tau}}_i(\boldsymbol{x})| \leq 1$ for all $\boldsymbol{x} \in \hat{Y}$. Then, under the assumptions stated in Theorem 3.3.2 and provided that $\hat{\varepsilon}(\boldsymbol{x}, \hat{\boldsymbol{y}})$ and $\hat{\sigma}(\boldsymbol{x}, \hat{\boldsymbol{y}})$ are sufficiently regular the following stability estimate holds true:*

$$\begin{aligned}\|\hat{\nabla}\hat{\nabla}_{\hat{\mathbf{t}}}\hat{\boldsymbol{\chi}}\|^2_{L^2(\hat{Y})} + \frac{1}{\omega}\|\hat{\nabla}_{\hat{\mathbf{t}}}\hat{\nabla}_{\hat{\mathbf{t}}}\hat{\boldsymbol{\chi}}\|^2_{L^2(\hat{\Sigma})} \\ \leq\ C\ \max\left\{\|\hat{\varepsilon}(\boldsymbol{x}, \hat{\boldsymbol{y}})\|^2_{W^{1,\infty}(\hat{Y})}, \frac{1}{\omega}\|\hat{\sigma}(\boldsymbol{x}, \hat{\boldsymbol{y}})\|^2_{W^{1,\infty}(\hat{\Sigma})}\right\} \\ \times \left\{\|\hat{\varepsilon}(\boldsymbol{x}, \hat{\boldsymbol{y}})\|^2_{W^{1,\infty}(\hat{Y})}\|\hat{F}^T\boldsymbol{e}_i\|^2_{H^1(\hat{Y})} + \frac{1}{\omega}\|\hat{\sigma}(\boldsymbol{x}, \hat{\boldsymbol{y}})\|^2_{W^{1,\infty}(\hat{\Sigma})}\|\hat{F}^T\boldsymbol{e}_i\|^2_{H^1(\hat{\Sigma})}\right\}. \quad (3.12)\end{aligned}$$

Here, the constant C only depends on $\hat{\Sigma}$ and the chosen extension of $\hat{\boldsymbol{\tau}}$.

In order to show regularity we follow the well-established strategy of introducing a difference quotient and then passing to the limit; see for example [27]. For the sake of completeness, we restate and generalize the argument here so that it can be applied to our case of a periodic domain with a curved hypersurface. A number of preparatory steps are in order.

Definition 3.3.4. *Let $\boldsymbol{\eta}(x) : \hat{Y} \to \mathbb{R}^n$ be a smooth, $\hat{Y}$-periodic vector field with $\boldsymbol{\eta}(\hat{\boldsymbol{y}})\cdot\boldsymbol{n}(\hat{\boldsymbol{y}}) = 0$ for $\hat{\boldsymbol{y}} \in \hat{\Sigma}$, where $\boldsymbol{n}$ denotes a fixed normal field on $\hat{\Sigma}$, and assume that $\boldsymbol{\eta}(\hat{\boldsymbol{y}}) = \mathbf{0}$ for $\hat{\boldsymbol{y}} \in \partial\hat{\Sigma}$.*

a) For $\hat{\boldsymbol{y}} \in \hat{Y}$ let $\boldsymbol{\xi}_{\boldsymbol{\eta},\hat{\boldsymbol{y}}} : \mathbb{R} \to \hat{Y}$ be the integral curve of $\boldsymbol{\eta}$ with $\boldsymbol{\xi}_{\boldsymbol{\eta},\hat{\boldsymbol{y}}}(0) = \hat{\boldsymbol{y}}$ and $\frac{d}{ds}\boldsymbol{\xi}_{\boldsymbol{\eta},\hat{\boldsymbol{y}}}(s) = \boldsymbol{\eta}(\boldsymbol{\xi}_{\boldsymbol{\eta},\hat{\boldsymbol{y}}}(s))$ for all $s \in \mathbb{R}$. Here, by slight abuse of notation, we equip $\hat{Y}$ with a toroidal topology by identifying opposing periodic boundaries, so that $\boldsymbol{\xi}_{\boldsymbol{\eta},\hat{\boldsymbol{y}}}$ admits $\mathbb{R}$ as domain of definition.

b) Introduce a transformation, $T_h : \hat{Y} \to \hat{Y}$ characterized by $T_h(\hat{\boldsymbol{y}}) := \boldsymbol{\xi}_{\boldsymbol{\eta},\hat{\boldsymbol{y}}}(h)$.

c) For a given $f \in C^\infty_{per}(\hat{Y})$ and $h > 0$ introduce two difference operators:

$$\hat{\nabla}^h_\eta f(\hat{\boldsymbol{y}}) := \frac{f\big(T_h(\hat{\boldsymbol{y}})\big) - f(\hat{\boldsymbol{y}})}{h}, \qquad \hat{\nabla}^{-h}_\eta f(\hat{\boldsymbol{y}}) := \frac{f(\hat{\boldsymbol{y}}) - f\big(T_{-h}(\hat{\boldsymbol{y}})\big)\kappa(\hat{\boldsymbol{y}})}{h}.$$

Here, $\kappa(\hat{\boldsymbol{y}}) := det\big(\nabla T_{-h}(\hat{\boldsymbol{y}})\big)$.

We have the following results at hand:

Lemma 3.3.5. *Let $\boldsymbol{\eta}$ be a vector field as characterized in definition 3.3.4. Then, for all $f, g \in C^\infty_{per}(\hat{Y})$ and under the assumption that $h > 0$ is sufficiently small it holds that*

(1.) T_h *and* T_{-h} *are automorphisms on* $\hat{Y}$ *and* $\hat{\Sigma}$, *with* $T_{-h} \circ T_h = Id$,

(2.) $|\nabla\kappa(\hat{\boldsymbol{y}})| \leq c\, h \max\big(|\nabla\boldsymbol{\eta}|_\infty(\hat{\boldsymbol{y}}), |\nabla^2\boldsymbol{\eta}(\hat{\boldsymbol{y}})|_\infty\big)$ *for all* $\hat{\boldsymbol{y}} \in \hat{Y}$,

(3.) $\displaystyle\int_{\hat{Y}} (\hat{\nabla}^h_\eta f(\hat{\boldsymbol{y}}))g(\hat{\boldsymbol{y}})\,\mathrm{d}\hat{y} = -\int_{\hat{Y}} f(\hat{\boldsymbol{y}})(\hat{\nabla}^{-h}_\eta g(\hat{\boldsymbol{y}}))\,\mathrm{d}\hat{y},$

(4.) $\displaystyle\int_{\hat{\Sigma}} (\hat{\nabla}^h_\eta f(\hat{\boldsymbol{y}}))g(\hat{\boldsymbol{y}})\,\mathrm{d}\hat{o}_{\hat{y}} = -\int_{\hat{\Sigma}} f(\hat{\boldsymbol{y}})(\hat{\nabla}^{-h}_\eta g(\hat{\boldsymbol{y}}))\,\mathrm{d}\hat{o}_{\hat{y}},$

(5.) $\hat{\nabla}^h_\eta(fg)(\hat{\boldsymbol{y}}) = f(T_h(\hat{\boldsymbol{y}}))(\hat{\nabla}^h_\eta g)(\hat{\boldsymbol{y}}) + (\hat{\nabla}^h_\eta f)(\hat{\boldsymbol{y}})g(\hat{\boldsymbol{y}}),$

(6.) $\displaystyle\lim_{h\to 0} \hat{\nabla}^h_\eta f(\hat{\boldsymbol{y}}) = \boldsymbol{\eta}(\hat{\boldsymbol{y}}) \cdot \hat{\nabla} f(\hat{\boldsymbol{y}}) =: \hat{\nabla}_\eta f(\hat{\boldsymbol{y}}).$

Proof. (1.) The integral curve $\boldsymbol{\xi}_{\boldsymbol{\eta},\hat{\boldsymbol{y}}}(s)$ is described by an initial value problem with smooth right hand side on $\hat{Y}$. Thus, by virtue of the Picard-Lindelöf theorem a unique solution $\boldsymbol{\xi}_{\boldsymbol{\eta},\hat{\boldsymbol{y}}}(s)$ exists. Moreover, $\boldsymbol{\xi}_{\boldsymbol{\eta},\hat{\boldsymbol{y}}}(s)$ depends smoothly on the initial data $\hat{\boldsymbol{y}}$ and the differential $\nabla_{\hat{\boldsymbol{y}}}\boldsymbol{\xi}_{\boldsymbol{\eta},\hat{\boldsymbol{y}}}(s)$ is given by an initial value problem

$$\nabla_{\hat{\boldsymbol{y}}}\boldsymbol{\xi}_{\boldsymbol{\eta},\hat{\boldsymbol{y}}}(0) = \boldsymbol{I}, \qquad \frac{\mathrm{d}}{\mathrm{d}s}\nabla_{\hat{\boldsymbol{y}}}\boldsymbol{\xi}_{\boldsymbol{\eta},\hat{\boldsymbol{y}}}(s) = \nabla\boldsymbol{\eta}(\xi_{\boldsymbol{\eta},\hat{\boldsymbol{y}}}(s))\nabla_{\hat{\boldsymbol{y}}}\boldsymbol{\xi}_{\boldsymbol{\eta},\hat{\boldsymbol{y}}}(s). \tag{3.13}$$

This shows that the transformation $T_h(\hat{\boldsymbol{y}}) = \boldsymbol{\xi}_{\boldsymbol{\eta},\hat{\boldsymbol{y}}}(h)$ is a well-defined differentiable function. Moreover, owing to the compactness of $\hat{Y}$ there exists an h_0 such that $\|\nabla T_h(\hat{\boldsymbol{y}}) - \boldsymbol{I}\| \leq \delta < 1$ for all $\hat{\boldsymbol{y}} \in \hat{Y}$ and $|h| \leq h_0$. This implies that T_h is injective for $|h| \leq h_0$. A consequence of the initial value problem of the integral curves is the fact that $\boldsymbol{\xi}_{\boldsymbol{\eta},\tilde{\boldsymbol{y}}}(-h) = \hat{\boldsymbol{y}}$ for $\tilde{\boldsymbol{y}} = \boldsymbol{\xi}_{\boldsymbol{\eta},\hat{\boldsymbol{y}}}(h)$

for all $\hat{\boldsymbol{y}} \in \hat{Y}$. This implies that $T_{-h} \circ T_h = Id$.

(2.) We first observe that $\nabla\kappa(\hat{\boldsymbol{y}})$ is a sum of products of $(d-1)$ entries of $\nabla_{\hat{\boldsymbol{y}}}\boldsymbol{\xi}_{\boldsymbol{\eta},\hat{\boldsymbol{y}}}(h)$ and one entry of the tensor of second derivatives $\nabla^2_{\hat{\boldsymbol{y}}}\boldsymbol{\xi}_{\boldsymbol{\eta},\hat{\boldsymbol{y}}}(h)$. This implies that,

$$|\nabla\kappa(\hat{\boldsymbol{y}})|_\infty \leq c\,|\nabla_{\hat{\boldsymbol{y}}}\boldsymbol{\xi}_{\boldsymbol{\eta},\hat{\boldsymbol{y}}}(h)|_\infty^{d-1}\,|\nabla^2_{\hat{\boldsymbol{y}}}\boldsymbol{\xi}_{\boldsymbol{\eta},\hat{\boldsymbol{y}}}(h)|_\infty \leq c\,|\nabla^2_{\hat{\boldsymbol{y}}}\boldsymbol{\xi}_{\boldsymbol{\eta},\hat{\boldsymbol{y}}}(h)|_\infty,$$

where for the second inequality we increased the constant c with a uniform bound on $\nabla_{\hat{\boldsymbol{y}}}\boldsymbol{\xi}_{\boldsymbol{\eta},\hat{\boldsymbol{y}}}(h)$ that was established for $|h| \leq h_0$ in (1.). We now observe that $\nabla^2_{\hat{\boldsymbol{y}}}\hat{\boldsymbol{y}}_{\boldsymbol{\eta},\hat{\boldsymbol{y}}}(0) = \mathbf{0}$. The tensor of second derivatives obeys an initial value problem similarly to (3.13) but with a right hand side involving $\nabla\boldsymbol{\eta}(\hat{\boldsymbol{y}})$ and $\nabla^2\boldsymbol{\eta}(\hat{\boldsymbol{y}})$:

$$\frac{\mathrm{d}}{\mathrm{d}s}\nabla^2_{\hat{\boldsymbol{y}}}\boldsymbol{\xi}_{\boldsymbol{\eta},\hat{\boldsymbol{y}}}(s) = \big(\nabla^2\boldsymbol{\eta}(\xi_{\boldsymbol{\eta},\hat{\boldsymbol{y}}}(s))\nabla_{\hat{\boldsymbol{y}}}\boldsymbol{\xi}_{\boldsymbol{\eta},\hat{\boldsymbol{y}}}(s)\big)\cdot\nabla_{\hat{\boldsymbol{y}}}\boldsymbol{\xi}_{\boldsymbol{\eta},\hat{\boldsymbol{y}}}(s) + \nabla\boldsymbol{\eta}(\xi_{\boldsymbol{\eta},\hat{\boldsymbol{y}}}(s))\nabla^2_{\hat{\boldsymbol{y}}}\boldsymbol{\xi}_{\boldsymbol{\eta},\hat{\boldsymbol{y}}}(s).$$

Integrating the differential equation and using the initial condition we get,

$$|\nabla^2_{\hat{\boldsymbol{y}}}\boldsymbol{\xi}_{\boldsymbol{\eta},\hat{\boldsymbol{y}}}(h)|_\infty \;\leq\; c\int_0^h \max\Big(|\nabla\boldsymbol{\eta}|,|\nabla^2\boldsymbol{\eta}|\Big)(\boldsymbol{\xi}_{\boldsymbol{\eta},\hat{\boldsymbol{y}}}(s))\mathrm{d}s.$$

possibly shrinking h_0 again with a compactness argument now establishes,

$$|\nabla^2_{\hat{\boldsymbol{y}}}\boldsymbol{\xi}_{\boldsymbol{\eta},\hat{\boldsymbol{y}}}(h)|_\infty \;\leq\; ch\,\max\big(|\nabla\boldsymbol{\eta}|_\infty(\hat{\boldsymbol{y}}),|\nabla^2\boldsymbol{\eta}(\hat{\boldsymbol{y}})|_\infty\big).$$

(3.) By definition,

$$\int_{\hat{Y}}(\hat{\nabla}^h_\eta f(\hat{\boldsymbol{y}}))g(\hat{\boldsymbol{y}})\,\mathrm{d}\hat{y} = \int_{\hat{Y}}\frac{f(T_h(\hat{\boldsymbol{y}}))}{h}g(\hat{\boldsymbol{y}})\,\mathrm{d}\hat{y} - \int_{\hat{Y}}\frac{f(\hat{\boldsymbol{y}})}{h}g(\hat{\boldsymbol{y}})\,\mathrm{d}\hat{y}$$

Applying the transformation $\hat{\boldsymbol{y}} \mapsto T_{-h}(\hat{\boldsymbol{y}})$ and exploiting $\hat{Y}$-periodicity gives,

$$\begin{aligned}
&= \int_{\hat{Y}} \frac{f(\hat{\boldsymbol{y}})}{h} g(T_{-h}(\hat{\boldsymbol{y}}))\kappa(\hat{\boldsymbol{y}})\,\mathrm{d}\hat{y} - \int_{\hat{Y}} \frac{f(\hat{\boldsymbol{y}})}{h} g(\hat{\boldsymbol{y}})\,\mathrm{d}\hat{y} \\
&= -\int_{\hat{Y}} f(\hat{\boldsymbol{y}})(\hat{\nabla}_{\eta}^{-h} g(\hat{\boldsymbol{y}}))\,\mathrm{d}\hat{y}.
\end{aligned}$$

(4.) The proof of this statement is similar to (1.) with the important detail that we have to establish that the transformed surface element is given by $\kappa(\hat{\boldsymbol{y}})\,\mathrm{d}\hat{o}_{\hat{y}}$. By definition of $\boldsymbol{\eta}$ we have $\boldsymbol{\eta}(\hat{\boldsymbol{y}}) \cdot \boldsymbol{n}(\hat{\boldsymbol{y}}) = 0$ for $\hat{\boldsymbol{y}} \in \hat{\Sigma}$. This implies that $\hat{\Sigma}$ is *parallel* to integral curves and as a consequence we have that,

$$\hat{\nabla} T_h(\hat{\boldsymbol{y}}) \simeq \begin{pmatrix} \partial_{\tau_1}(T_h \cdot \boldsymbol{\tau}_1) & \partial_{\tau_2}(T_h \cdot \boldsymbol{\tau}_1) & \partial_n(T_h \cdot \boldsymbol{\tau}_1) \\ \partial_{\tau_1}(T_h \cdot \boldsymbol{\tau}_2) & \partial_{\tau_2}(T_h \cdot \boldsymbol{\tau}_2) & \partial_n(T_h \cdot \boldsymbol{\tau}_2) \\ 0 & 0 & 1 \end{pmatrix},$$

when expressing the Jacobian of $T_h(\hat{\boldsymbol{y}})$ for $\hat{\boldsymbol{y}} \in \hat{\Sigma}$ in a local coordinate system spanned by $(\boldsymbol{n}, \boldsymbol{\tau}_1, \boldsymbol{\tau}_2)$.

(5.) An elementary calculation shows:

$$\begin{aligned}
\hat{\nabla}_{\eta}^{h}(fg)(\hat{\boldsymbol{y}}) &= \frac{f(T_h(\hat{\boldsymbol{y}}))g(T_h(\hat{\boldsymbol{y}})) - f(T_h(\hat{\boldsymbol{y}}))g(\hat{\boldsymbol{y}})}{h} \\
&\qquad + \frac{f(T_h(\hat{\boldsymbol{y}}))g(\hat{\boldsymbol{y}}) - f(\hat{\boldsymbol{y}})g(\hat{\boldsymbol{y}})}{h} \\
&= f(T_h(\hat{\boldsymbol{y}}))(\hat{\nabla}_{\eta}^{h} g)(\hat{\boldsymbol{y}}) + g(\hat{\boldsymbol{y}})(\hat{\nabla}_{\eta}^{h} f)(\hat{\boldsymbol{y}}).
\end{aligned}$$

(6.) This is an immediate consequence of the differentiability of $f(\hat{\boldsymbol{y}})$ and the L'Hôpital theorem. □

With this definition and lemma, we prove the following intermediate result:

Proposition 3.3.6. *Let $\boldsymbol{\eta}(x) : \hat{Y} \to \mathbb{R}^n$ be a smooth, $\hat{Y}$-periodic vector field with $\boldsymbol{\eta}(\hat{\boldsymbol{y}}) \cdot \boldsymbol{n}(\hat{\boldsymbol{y}}) = 0$ for $\hat{\boldsymbol{y}} \in \hat{\Sigma}$, as well as $\boldsymbol{\eta}(\hat{\boldsymbol{y}}) = \mathbf{0}$ for all $\hat{\boldsymbol{y}} \in \partial\hat{\Sigma}$. Let $\hat{\boldsymbol{\chi}} \in H$ be the solution to (2.25). Then, provided that $\varepsilon(\boldsymbol{x}, \hat{\boldsymbol{y}})$, $\sigma(\boldsymbol{x}, \hat{\boldsymbol{y}})$ and $\hat{\boldsymbol{q}}(\hat{\boldsymbol{y}})$ are sufficiently regular:*

$$\begin{aligned}\|\hat{\nabla}\hat{\nabla}_\eta\hat{\boldsymbol{\chi}}\|^2_{L^2(\hat{Y})} + \frac{1}{\omega}\|\hat{\nabla}_{\hat{\mathbf{t}}}\hat{\nabla}_\eta\hat{\boldsymbol{\chi}}\|^2_{L^2(\hat{\Sigma})} \le\ & C\ \max\Big\{1, \|\hat{\nabla}\boldsymbol{\eta}\|_{L^\infty(\hat{Y})}, \|\hat{\nabla}^2\boldsymbol{\eta}\|_{L^\infty(\hat{Y})}\Big\} \\ & \times \Big\{\|\hat{\varepsilon}(\boldsymbol{x}, \hat{\boldsymbol{y}})\|^2_{W^{1,\infty}(\hat{Y})}\|\hat{\nabla}\hat{\boldsymbol{\chi}}\|^2_{L^2(\hat{Y})} + \frac{1}{\omega}\|\hat{\sigma}(\boldsymbol{x}, \hat{\boldsymbol{y}})\|^2_{W^{1,\infty}(\hat{\Sigma})}\|\hat{\nabla}_{\hat{\mathbf{t}}}\hat{\boldsymbol{\chi}}\|^2_{L^2(\hat{\Sigma})} \\ & \quad + \|\hat{\varepsilon}(\boldsymbol{x}, \hat{\boldsymbol{y}})\|^2_{W^{1,\infty}(\hat{Y})}\|\hat{F}^T\boldsymbol{e}_i\|^2_{H^1(\hat{Y})} + \frac{1}{\omega}\|\hat{\sigma}(\boldsymbol{x}, \hat{\boldsymbol{y}})\|^2_{W^{1,\infty}(\hat{\Sigma})}\|\hat{F}^T\boldsymbol{e}_i\|^2_{H^1(\hat{\Sigma})}\Big\}. \quad (3.14)\end{aligned}$$

Proof. Above assumptions on $\boldsymbol{\eta}(\hat{\boldsymbol{y}})$ ensure that $\hat{\boldsymbol{\varphi}} := \hat{\nabla}_\eta^{-h}\hat{\nabla}_\eta^h\,\hat{\boldsymbol{\chi}} \in H$. Testing (3.7) with this choice of test function $\hat{\boldsymbol{\varphi}}$ and taking the real part:

$$\begin{aligned}\int_{\hat{Y}} \operatorname{Re}\hat{\varepsilon}\,\hat{\nabla}\hat{\boldsymbol{\chi}}^{\,T}\cdot\hat{\nabla}\hat{\nabla}_\eta^{-h}\hat{\nabla}_\eta^h\overline{\hat{\boldsymbol{\chi}}}^{\,T}\,\mathrm{d}\hat{y} + \frac{1}{\omega}\int_{\hat{\Sigma}}\operatorname{Im}\hat{\sigma}\,\hat{\nabla}_{\hat{\mathbf{t}}}\hat{\boldsymbol{\chi}}^{\,T}\cdot\hat{\nabla}_{\hat{\mathbf{t}}}\hat{\nabla}_\eta^{-h}\hat{\nabla}_\eta^h\overline{\hat{\boldsymbol{\chi}}}^{\,T}\,\mathrm{d}\hat{o}_{\hat{y}} \\ = -\operatorname{Re}\Big\{\int_{\hat{Y}}\hat{\varepsilon}(\boldsymbol{x}, \hat{\boldsymbol{y}})(\hat{F}(\hat{\boldsymbol{y}})^T)\cdot\hat{\nabla}\hat{\nabla}_\eta^{-h}\hat{\nabla}_\eta^h\overline{\hat{\boldsymbol{\chi}}}^{\,T}\,\mathrm{d}\hat{y} \\ + \frac{1}{i\omega}\int_{\hat{\Sigma}}\hat{\sigma}(\boldsymbol{x}, \hat{\boldsymbol{y}})(\hat{F}(\hat{\boldsymbol{y}})^T)_{\hat{\mathbf{t}}}\cdot\hat{\nabla}_{\hat{\mathbf{t}}}\hat{\nabla}_\eta^{-h}\hat{\nabla}_\eta^h\overline{\hat{\boldsymbol{\chi}}}^{\,T}\,\mathrm{d}\hat{o}_{\hat{y}}\Big\}. \quad (3.15)\end{aligned}$$

We now wish to move the difference operator $\hat{\nabla}_\eta^{-h}$ from the testfunction over to $\hat{\boldsymbol{\chi}}(\hat{\boldsymbol{q}})$ and the forcing terms but we are faced with the issue that due to the curvature encoded in $\boldsymbol{\eta}(\hat{\boldsymbol{y}})$ the operators $\hat{\nabla}$, $\hat{\nabla}_{\hat{\mathbf{t}}}$, $\hat{\nabla}_\eta^{-h}$, $\hat{\nabla}_\eta^h$ do not necessarily commute. Observe, for example, that

$$[\hat{\nabla}, \hat{\nabla}_\eta^{-h}]f(\hat{\boldsymbol{y}}) \;=\; \hat{\nabla}f\big(T_{-h}(\hat{\boldsymbol{y}})\big)\hat{\nabla}\boldsymbol{\eta}(\hat{\boldsymbol{y}})\kappa(\hat{\boldsymbol{y}}) + f\big(T_{-h}(\hat{\boldsymbol{y}})\big)\frac{\hat{\nabla}\kappa(\hat{\boldsymbol{y}})}{h}, \quad (3.16)$$

where $[.,.]$ denotes the commutator. Lemma 3.3.5(2.) establishes that $|\kappa(\hat{\boldsymbol{y}})/h|_\infty \le c\,\max\big(|\nabla^2\boldsymbol{\eta}(\hat{\boldsymbol{y}})|_\infty, |\nabla^2\boldsymbol{\eta}(\hat{\boldsymbol{y}})|_\infty\big)$. Applying this result to (3.16) and taking the limit $h \to 0$ on the right hand side yields

$$\big\|[\hat{\nabla}, \hat{\nabla}_\eta^{-h}]f(\hat{\boldsymbol{y}})\big\|_{L^2(\hat{Y})} \le\ C\ \max\big\{1, \|\hat{\nabla}\boldsymbol{\eta}\|_{L^\infty(\hat{Y})}, \|\hat{\nabla}^2\boldsymbol{\eta}\|_{L^\infty(\hat{Y})}\big\}\,\big\|\hat{\nabla}f(\hat{\boldsymbol{y}})\|_{L^2(\hat{Y})}, \quad (3.17)$$

where we have used a Poincaré inequality valid for periodic $f(\hat{\boldsymbol{y}})$. A similar result holds for all other commutator pairings. Then, moving the difference operator and applying the integration by parts formula and product rule formula established in Lemma 3.3.5 we arrive at

$$\begin{aligned}
&\int_{\hat{Y}} \operatorname{Re}\hat{\varepsilon}(\boldsymbol{x}, T_h(\hat{\boldsymbol{y}}))\, \hat{\nabla}\hat{\nabla}_\eta^h \hat{\boldsymbol{\chi}}^T \cdot \hat{\nabla}\hat{\nabla}_\eta^h \overline{\hat{\boldsymbol{\chi}}}^T + (\hat{\nabla}_\eta^h \operatorname{Re}\hat{\varepsilon})\, \hat{\nabla}\hat{\boldsymbol{\chi}}^T \cdot \hat{\nabla}\hat{\nabla}_\eta^h \overline{\hat{\boldsymbol{\chi}}}^T \,\mathrm{d}\hat{y} \\
&\quad + \frac{1}{\omega}\int_{\hat{\Sigma}} \operatorname{Im}\hat{\sigma}(\boldsymbol{x}, T_h(\hat{\boldsymbol{y}}))\hat{\nabla}_{\hat{\mathbf{t}}}\hat{\nabla}_\eta^h \hat{\boldsymbol{\chi}}^T \cdot \hat{\nabla}_{\hat{\mathbf{t}}}\hat{\nabla}_\eta^h \overline{\hat{\boldsymbol{\chi}}}^T + (\hat{\nabla}_\eta^h \operatorname{Im}\hat{\sigma})\hat{\nabla}_{\hat{\mathbf{t}}}\hat{\boldsymbol{\chi}}^T \cdot \hat{\nabla}_{\hat{\mathbf{t}}}\hat{\nabla}_\eta^h \overline{\hat{\boldsymbol{\chi}}}^T \,\mathrm{d}\hat{o}_{\hat{y}} \\
&\qquad = -\operatorname{Re}\Big\{ \int_{\hat{Y}} \hat{\nabla}_\eta^h\big\{\hat{\varepsilon}(\boldsymbol{x}, \hat{\boldsymbol{y}})(\hat{F}(\hat{\boldsymbol{y}})^T)\big\} \cdot \hat{\nabla}\hat{\nabla}_\eta^h \overline{\hat{\boldsymbol{\chi}}}^T \,\mathrm{d}\hat{y} \\
&\qquad\quad + \frac{1}{i\omega}\int_{\hat{\Sigma}} \hat{\nabla}_\eta^h\big\{\hat{\sigma}(\boldsymbol{x}, \hat{\boldsymbol{y}})(\hat{F}(\hat{\boldsymbol{y}})^T)_{\hat{\mathbf{t}}}\big\} \cdot \hat{\nabla}_{\hat{\mathbf{t}}}\hat{\nabla}_\eta^h \overline{\hat{\boldsymbol{\chi}}}^T \,\mathrm{d}\hat{o}_{\hat{y}} \Big\} \\
&\qquad\qquad + \big\{\text{commutator terms}\big\}, \quad (3.18)
\end{aligned}$$

where we have collected all commutator terms in the last term (and discuss them further down below). Proceeding again as in the proof for Theorem 3.3.2 by using Young's inequality for all terms on the right hand side and uniform ellipticity of $\operatorname{Re}\hat{\varepsilon}$ and $\operatorname{Im}\hat{\sigma}$ yields:

$$\begin{aligned}
&\|\hat{\nabla}\hat{\nabla}_\eta^h \hat{\boldsymbol{\chi}}\|_{L^2(\hat{Y})}^2 + \frac{1}{\omega}\|\hat{\nabla}_{\hat{\mathbf{t}}}\hat{\nabla}_\eta^h \hat{\boldsymbol{\chi}}\|_{L^2(\hat{\Sigma})}^2 \\
&\qquad \leq\ C\,\Big\{ \|\hat{\varepsilon}(\boldsymbol{x}, \hat{\boldsymbol{y}})\|_{W^{1,\infty}(\hat{Y})}^2 \|\hat{\nabla}\hat{\boldsymbol{\chi}}\|_{L^2(\hat{Y})}^2 + \frac{1}{\omega}\|\hat{\sigma}(\boldsymbol{x}, \hat{\boldsymbol{y}})\|_{W^{1,\infty}(\hat{\Sigma})}^2 \|\hat{\nabla}_{\hat{\mathbf{t}}}\hat{\boldsymbol{\chi}}\|_{L^2(\hat{\Sigma})}^2 \\
&\qquad\quad + \|\hat{\varepsilon}(\boldsymbol{x}, \hat{\boldsymbol{y}})\|_{W^{1,\infty}(\hat{Y})}^2 \|\hat{F}^T\|_{H^1(\hat{Y})}^2 + \frac{1}{\omega}\|\hat{\sigma}(\boldsymbol{x}, \hat{\boldsymbol{y}})\|_{W^{1,\infty}(\hat{\Sigma})}^2 \|\hat{F}^T\|_{H^1(\hat{\Sigma})}^2 \\
&\qquad\qquad + \big|\text{commutator terms}\big| \Big\} \quad (3.19)
\end{aligned}$$

In the estimate above we have passed to the limit, $h \to 0$, on the right hand side.

As a last step we will discuss the commutator terms. The volume integral over $\hat{Y}$, for example, gives rise to the following terms:

$$\begin{aligned}(\mathrm{a}) \;=\; \int_{\hat{Y}} \operatorname{Re} \hat{\varepsilon}\, \hat{\nabla}\hat{\boldsymbol{\chi}}^{\,T} \cdot [\hat{\nabla}, \hat{\nabla}_\eta^{-h}] \hat{\nabla}_\eta^h \overline{\hat{\boldsymbol{\chi}}}^{\,T} \,\mathrm{d}\hat{y} \\ + \int_{\hat{Y}} \operatorname{Re} \hat{\varepsilon}(T_h(\hat{\boldsymbol{y}}))\, [\hat{\nabla}, \hat{\nabla}_\eta^h] \hat{\boldsymbol{\chi}}^{\,T} \cdot \hat{\nabla} \hat{\nabla}_\eta^h \overline{\hat{\boldsymbol{\chi}}}^{\,T} \,\mathrm{d}\hat{y} \\ + \operatorname{Re} \Big\{ \int_{\hat{Y}} \hat{\varepsilon}(\boldsymbol{x}, \hat{\boldsymbol{y}}) (\hat{F}(\hat{\boldsymbol{y}})^T) \cdot [\hat{\nabla}, \hat{\nabla}_\eta^{-h}] \hat{\nabla}_\eta^h \overline{\hat{\boldsymbol{\chi}}}^{\,T} \,\mathrm{d}\hat{y} \Big\}.\end{aligned}$$

Applying (3.17) allows us to estimate (a) by

$$\begin{aligned}\big|(a)\big| \;\le\; C\, \|\hat{\varepsilon}(\boldsymbol{x}, \hat{\boldsymbol{y}})\|_{L^\infty(\hat{Y})} \max\big\{1, \|\hat{\nabla}\boldsymbol{\eta}\|_{L^\infty(\hat{Y})}, \|\hat{\nabla}^2 \boldsymbol{\eta}\|_{L^\infty(\hat{Y})}\big\} \\ \|\hat{\nabla}\hat{\nabla}_\eta^h \hat{\boldsymbol{\chi}}\|_{L^2(\hat{Y})} \Big\{ \|\hat{\nabla}\hat{\boldsymbol{\chi}}\|_{L^2(\hat{Y})} + \|\hat{F}^T\|_{H^1(\hat{Y})} \Big\}.\end{aligned}$$

This expression can again be absorbed into the remaining terms of (3.19) by changing the constant C to $C \max\{1, \|\hat{\nabla}\boldsymbol{\eta}\|_{L^\infty(\hat{Y})}, \|\hat{\nabla}^2\boldsymbol{\eta}\|_{L^\infty(\hat{Y})}\}$. An analogous result holds for all terms arising from the surface integral over $\hat{\Sigma}$. Passing to the limit $h \to 0$ on the left side [27] now shows the final estimate given in (3.14). □

Proof of Theorem 3.3.3. Estimate (3.12) is an immediate consequence of Proposition 3.3.6 by setting $\boldsymbol{\eta} = \hat{\boldsymbol{\tau}}_i$ and using Theorem 3.3.2 to estimate the $\|\hat{\nabla}\hat{\boldsymbol{\chi}}\|_{L^2(\hat{Y})}$ and $\|\hat{\nabla}_{\hat{\mathfrak{t}}}\hat{\boldsymbol{\chi}}\|_{L^2(\hat{\Sigma})}$ terms on the right hand side of (3.14). □

3.4 Lipschitz dependence on $\hat{\boldsymbol{q}}$

The Lipschitz continuity of $\hat{\boldsymbol{q}} \mapsto \hat{\boldsymbol{\chi}}(\hat{\boldsymbol{q}})$ implies that this mapping is already Gâteaux differentiable almost everywhere, see, e.g., [10]. This justifies to take Gâteaux derivatives with respect to the control $\hat{\boldsymbol{q}}$ in the adjoint formulation; see Chapter 4.

Theorem 3.4.1 (Lipschitz dependence)**.** *Under the assumptions on the deformation field $\hat{\boldsymbol{q}}(\hat{\boldsymbol{y}})$ as stated in Lemma 3.2.2, the corrector $\hat{\boldsymbol{\chi}}(\hat{\boldsymbol{q}})$ given by the cell problem* (3.7) *depends at least Lipschitz-continuously on $\hat{\boldsymbol{q}}$. More precisely, let $\hat{\boldsymbol{q}}_1, \hat{\boldsymbol{q}}_2 \in \boldsymbol{D}(\hat{Y}, \hat{\Sigma})$ be arbitrarily chosen*

such that the assumptions of Lemma 3.2.2 are satisfied. Let $\hat{\boldsymbol{\chi}}_1, \hat{\boldsymbol{\chi}}_2 \in \boldsymbol{H}(\hat{Y}, \hat{\Sigma})$ *denote the solutions to* (3.7) *for deformation fields* $\hat{\boldsymbol{q}}_1$ *and* $\hat{\boldsymbol{q}}_2$*, respectively. Then, assuming that* $\hat{\boldsymbol{q}}_1$ *is suitably close to* $\hat{\boldsymbol{q}}_2$*, we have:*

$$\begin{aligned}
&\|\hat{\nabla}(\hat{\boldsymbol{\chi}}_1 - \hat{\boldsymbol{\chi}}_2)\|^2_{L^2(\hat{Y})} + \frac{1}{\omega}\|\hat{\nabla}_{\hat{\mathbf{t}}}(\hat{\boldsymbol{\chi}}_1 - \hat{\boldsymbol{\chi}}_2)\|^2_{L^2(\hat{\Sigma})} \\
&\qquad \leq\ C(\hat{\boldsymbol{q}}) \left\{ \|\hat{\varepsilon}_1(\boldsymbol{x}, \hat{\boldsymbol{y}}) - \hat{\varepsilon}_2(\boldsymbol{x}, \hat{\boldsymbol{y}})\|^2_{L^\infty(\hat{Y})} + \frac{1}{\omega}\, \|\hat{\sigma}_1(\boldsymbol{x}, \hat{\boldsymbol{y}}) - \hat{\sigma}_2(\boldsymbol{x}, \hat{\boldsymbol{y}})\|^2_{L^\infty(\hat{\Sigma})} \right\} \\
&\qquad\qquad \leq\ C(\hat{\boldsymbol{q}}_2) \left\{ \|\hat{\boldsymbol{q}}_1 - \hat{\boldsymbol{q}}_2\|^2_{L^\infty(\hat{Y})} + \|\hat{\boldsymbol{q}}_1 - \hat{\boldsymbol{q}}_2\|^2_{L^\infty(\hat{\Sigma})} \right\}, \quad (3.20)
\end{aligned}$$

where the constant C *only depends on* $\hat{F}_2(\hat{\boldsymbol{y}})$ *and thus on* $\hat{\boldsymbol{q}}_2$*.*

Proof. We begin with $E(\hat{\boldsymbol{\chi}}_1 - \hat{\boldsymbol{\chi}}_2, \hat{\boldsymbol{\chi}}_1 - \hat{\boldsymbol{\chi}}_2; \hat{\boldsymbol{q}}_1)$. Setting $\hat{F}_1(\hat{\boldsymbol{y}}) := \boldsymbol{I} + \hat{\nabla}\hat{\boldsymbol{q}}_1(\hat{\boldsymbol{y}})$, $\hat{F}_2(\hat{\boldsymbol{y}}) := \boldsymbol{I} + \hat{\nabla}\hat{\boldsymbol{q}}_2(\hat{\boldsymbol{y}})$ and correspondingly, $\hat{J}_1$, $\hat{J}_2$, $\hat{\varepsilon}_1(\boldsymbol{x}, \hat{\boldsymbol{y}})$, $\hat{\varepsilon}_2(\boldsymbol{x}, \hat{\boldsymbol{y}})$, $\hat{\sigma}_1(\boldsymbol{x}, \hat{\boldsymbol{y}})$, $\hat{\sigma}_2(\boldsymbol{x}, \hat{\boldsymbol{y}})$, we observe that

$$\begin{aligned}
E(\hat{\boldsymbol{\chi}}_1 - \hat{\boldsymbol{\chi}}_2, \hat{\boldsymbol{\chi}}_1 - \hat{\boldsymbol{\chi}}_2; \hat{\boldsymbol{q}}_1) \ &=\ E(\hat{\boldsymbol{\chi}}_2, \hat{\boldsymbol{\chi}}_2 - \hat{\boldsymbol{\chi}}_1; \hat{\boldsymbol{q}}_1) - E(\hat{\boldsymbol{\chi}}_2, \hat{\boldsymbol{\chi}}_2 - \hat{\boldsymbol{\chi}}_1; \hat{\boldsymbol{q}}_2) \\
&= \int_{\hat{Y}} \left\{ \hat{\varepsilon}_1(\boldsymbol{x}, \hat{\boldsymbol{y}}) - \hat{\varepsilon}_2(\boldsymbol{x}, \hat{\boldsymbol{y}}) \right\} \hat{\nabla} \hat{\boldsymbol{\chi}}_2^{\,T} \cdot \overline{\hat{\nabla}(\hat{\boldsymbol{\chi}}_2 - \hat{\boldsymbol{\chi}}_1)^{\,T}}\, \mathrm{d}\hat{y} \\
&\quad - \frac{1}{i\omega} \int_{\hat{\Sigma}} \left\{ \hat{\sigma}_1(\boldsymbol{x}, \hat{\boldsymbol{y}}) - \hat{\sigma}_2(\boldsymbol{x}, \hat{\boldsymbol{y}}) \right\} \overline{\hat{\nabla}_{\hat{\mathbf{t}}}(\hat{\boldsymbol{\chi}}_2 - \hat{\boldsymbol{\chi}}_2)^{\,T} \cdot \hat{\nabla}_{\hat{\mathbf{t}}} \hat{\boldsymbol{\chi}}_2^{\,T}}\, \mathrm{d}\hat{o}_{\hat{y}} \\
&\quad + \int_{\hat{Y}} \left\{ \hat{\varepsilon}_1(\boldsymbol{x}, \hat{\boldsymbol{y}}) \hat{F}_1(\hat{\boldsymbol{y}})^T - \hat{\varepsilon}_2(\boldsymbol{x}, \hat{\boldsymbol{y}}) \hat{F}_2(\hat{\boldsymbol{y}})^T \right\} \cdot \overline{\hat{\nabla}(\hat{\boldsymbol{\chi}}_2 - \hat{\boldsymbol{\chi}}_1)^{\,T}}\, \mathrm{d}\hat{y} \\
&\quad - \frac{1}{i\omega} \int_{\hat{\Sigma}} \left\{ \hat{\sigma}_1(\boldsymbol{x}, \hat{\boldsymbol{y}}) (\hat{F}_1(\hat{\boldsymbol{y}}))^T_{\mathbf{t}} - \hat{\sigma}_2(\boldsymbol{x}, \hat{\boldsymbol{y}}) (\hat{F}_2(\hat{\boldsymbol{y}}))^T_{\mathbf{t}} \right\} \cdot \overline{\hat{\nabla}_{\hat{\mathbf{t}}}(\hat{\boldsymbol{\chi}}_2 - \hat{\boldsymbol{\chi}}_1)^{\,T}}\, \mathrm{d}\hat{o}_{\hat{y}}.
\end{aligned}$$

Now, proceeding as in the proof of Theorem 3.3.2

$$
\begin{aligned}
&\|\hat{\nabla}(\hat{\boldsymbol{\chi}}_1 - \hat{\boldsymbol{\chi}}_2)\|^2_{L^2(\hat{Y})} + \frac{1}{\omega}\|\hat{\nabla}_{\hat{\mathbf{t}}}(\hat{\boldsymbol{\chi}}_1 - \hat{\boldsymbol{\chi}}_2)\|^2_{L^2(\hat{\Sigma})} \\
&\qquad \leq C\Big\{ \|\hat{\varepsilon}_1(\boldsymbol{x},\hat{\boldsymbol{y}}) - \hat{\varepsilon}_2(\boldsymbol{x},\hat{\boldsymbol{y}})\|_{L^\infty(\hat{Y})}\|\hat{\nabla}\hat{\boldsymbol{\chi}}_2\|_{L^2(\hat{Y})}\|\hat{\nabla}(\hat{\boldsymbol{\chi}}_2 - \hat{\boldsymbol{\chi}}_1)\|_{L^2(\hat{Y})} \\
&\qquad\qquad + \frac{1}{\omega}\,\|\hat{\sigma}_1(\boldsymbol{x},\hat{\boldsymbol{y}}) - \hat{\sigma}_2(\boldsymbol{x},\hat{\boldsymbol{y}})\|_{L^\infty(\hat{\Sigma})}\|\hat{\nabla}_{\hat{\mathbf{t}}}\hat{\boldsymbol{\chi}}_2\|_{L^2(\hat{\Sigma})}\|\hat{\nabla}_{\hat{\mathbf{t}}}(\hat{\boldsymbol{\chi}}_2 - \hat{\boldsymbol{\chi}}_1)\|_{L^2(\hat{\Sigma})} \\
&\qquad\qquad + \|\hat{\varepsilon}_1(\boldsymbol{x},\hat{\boldsymbol{y}})\hat{F}_1(\hat{\boldsymbol{y}})^T - \hat{\varepsilon}_2(\boldsymbol{x},\hat{\boldsymbol{y}})\hat{F}_2(\hat{\boldsymbol{y}})^T\|_{L^2(\hat{Y})}\|\hat{\nabla}(\hat{\boldsymbol{\chi}}_2 - \hat{\boldsymbol{\chi}}_1)\|_{L^2(\hat{Y})} \\
&\qquad\qquad + \frac{1}{\omega}\,\|\hat{\sigma}_1(\boldsymbol{x},\hat{\boldsymbol{y}})\hat{F}_1(\hat{\boldsymbol{y}})^T - \hat{\sigma}_2(\boldsymbol{x},\hat{\boldsymbol{y}})\hat{F}_2(\hat{\boldsymbol{y}})^T\|_{L^2(\hat{\Sigma}}\|\hat{\nabla}_{\hat{\mathbf{t}}}(\hat{\boldsymbol{\chi}}_2 - \hat{\boldsymbol{\chi}}_1)\|_{L^2(\hat{\Sigma})}\Big\}
\end{aligned}
$$

Young's inequality allows to absorb all factors with differences $\hat{\boldsymbol{\chi}}_2 - \hat{\boldsymbol{\chi}}_1$ into the left hand side, and the factors $\|\hat{\nabla}\hat{\boldsymbol{\chi}}_2\|_{L^2(\hat{Y})}$ and $\|\hat{\nabla}_{\hat{\mathbf{t}}}\hat{\boldsymbol{\chi}}_2\|_{L^2(\hat{\Sigma})}$ can be bounded by a constant $C(\hat{\boldsymbol{q}}_2)$ only depending on $\hat{\boldsymbol{q}}_2$ (and the shape $\hat{\Sigma}$); see Theorem 3.3.2. In summary this implies that

$$
\begin{aligned}
&\|\hat{\nabla}(\hat{\boldsymbol{\chi}}_1 - \hat{\boldsymbol{\chi}}_2)\|^2_{L^2(\hat{Y})} + \frac{1}{\omega}\|\hat{\nabla}_{\hat{\mathbf{t}}}(\hat{\boldsymbol{\chi}}_1 - \hat{\boldsymbol{\chi}}_2)\|^2_{L^2(\hat{\Sigma})} \\
&\qquad\qquad \leq C(\hat{\boldsymbol{q}})\,\Big\{ \|\hat{\varepsilon}_1(\boldsymbol{x},\hat{\boldsymbol{y}}) - \hat{\varepsilon}_2(\boldsymbol{x},\hat{\boldsymbol{y}})\|^2_{L^\infty(\hat{Y})} + \frac{1}{\omega}\,\|\hat{\sigma}_1(\boldsymbol{x},\hat{\boldsymbol{y}}) - \hat{\sigma}_2(\boldsymbol{x},\hat{\boldsymbol{y}})\|^2_{L^\infty(\hat{\Sigma})}\Big\}.
\end{aligned}
$$

The final inequality now follows from the fact that for a fixed coordinate $\hat{\boldsymbol{y}}$ the tensors ε and σ depend analytically on $\hat{\boldsymbol{q}}$; see (3.9). □

The previous section establishes that the effective permittivity tensor $\varepsilon^{\text{eff}}(\hat{\boldsymbol{\chi}}; \hat{\boldsymbol{q}})$ given by (3.11) enjoys a sufficient degree of regular dependence on $\hat{\boldsymbol{q}}$ to formulate an optimization problem; and solve it by means of derivative based optimization methods. To this end, we introduce a cost functional with the target to minimize the Frobenius norm between $\varepsilon^{\text{eff}}(\hat{\boldsymbol{\chi}}, \hat{\boldsymbol{q}})$ and a given target permittivity tensor. This quantity is the *deviation*.

Definition 4.0.1 (Cost function)**.** *For a given target tensor ε^{target}, introduce a cost function*

$$C(\hat{\boldsymbol{\chi}}; \hat{\boldsymbol{q}}) \;:=\; \frac{1}{2} \left\| \varepsilon^{\mathit{eff}}(\hat{\boldsymbol{\chi}}, \hat{\boldsymbol{q}}) - \varepsilon^{\mathit{tgt.}} \right\|_{\mathit{Fr.}}^2 + \frac{\alpha}{2} \|\nabla \hat{\boldsymbol{q}}\|_w^2 + \beta \int_{\hat{Y}} P(\hat{\boldsymbol{y}}; \hat{\boldsymbol{q}}) \, \mathrm{d}\hat{y}, \tag{4.1}$$

$$\|\nabla \hat{\boldsymbol{q}}\|_w^2 \;:=\; \int_Y w(\hat{\boldsymbol{y}}) |\nabla \hat{\boldsymbol{q}}|^2 \, \mathrm{d}\hat{y}, \quad P(\hat{\boldsymbol{y}}; \hat{\boldsymbol{q}}) \;:=\; \begin{cases} \frac{1}{2} \frac{(\hat{J}(\hat{\boldsymbol{y}})-1)^2}{|\hat{J}(\hat{\boldsymbol{y}})|+\hat{J}(\hat{\boldsymbol{y}})} & \text{if } \hat{J}(\hat{\boldsymbol{y}}) < 1, \\ \frac{1}{2} \left(\hat{J}(\hat{\boldsymbol{y}}) - 1\right)^2 & \text{if } \hat{J}(\hat{\boldsymbol{y}}) \geq 1. \end{cases}$$

In addition to the deviation, we have the regularization term $\frac{\alpha}{2} \|\nabla \hat{\boldsymbol{q}}\|_w^2$. $\alpha > 0$ is an appropriately chosen *Tikhonov regularization parameter* and $w(\hat{\boldsymbol{y}}) > 0$ is a weight function that is chosen during the experiments. This regularization term ensures the shape changes remain smooth and physically feasible by providing some control over the derivative of the deformation.

Finally, we have the term $\beta \int_{\hat{Y}} P(\hat{\boldsymbol{y}}; \hat{\boldsymbol{q}}) \, \mathrm{d}\hat{y}$, with coefficient $\beta > 0$. This is a penalty on the deviation of transformation determinant from $\hat{J} = 1$ and also ensures that the transformation gradient remains positive. The specific choice of $P * \hat{\boldsymbol{y}}; \hat{\boldsymbol{q}})$ was made based on computational stability and efficiency. A particular difficulty that has to be addressed is the necessity to maintain a lower bound, $\hat{J} \geq \delta > 0$, on the transformation determinant.

The penalty term $P(\hat{\boldsymbol{y}};\hat{\boldsymbol{q}})$ is chosen to provide a barrier that enforces positivity of the transformation gradient $\hat{J}$ and penalizes a deviation away from 1. Strictly speaking, this penalty only enforces positivity of the transformation gradient, $\hat{J} > 0$, but not a uniform lower bound. This is not a problem for the discretized setting of our numerical computations (see Section 5.2) because the finite dimensionality will ensure that $\hat{J}$ remains bounded away from 0, though with a possibly discretization dependent constant δ_h. Nevertheless, if a guaranteed lower bound δ is desired then $P(\hat{\boldsymbol{y}};\hat{\boldsymbol{q}})$ can be easily modified to accommodate this by substituting $\hat{J}$ by $\hat{J} - \delta$.

We now seek solutions $(\hat{\boldsymbol{\chi}},\hat{\boldsymbol{q}}) \in X := \boldsymbol{H}(\hat{Y},\hat{\Sigma}) \times \boldsymbol{D}(\hat{Y},\hat{\Sigma})$ of the optimization problem

$$\min_{(\hat{\boldsymbol{\chi}},\hat{\boldsymbol{q}})\in X} C(\hat{\boldsymbol{\chi}};\hat{\boldsymbol{q}}) \quad \text{subject to} \quad E(\hat{\boldsymbol{\chi}},\hat{\boldsymbol{\varphi}};\hat{\boldsymbol{q}}) = 0 \ \text{ for all } \ \hat{\boldsymbol{\varphi}} \in \boldsymbol{H}(\hat{Y},\hat{\Sigma}). \tag{4.2}$$

4.1 Adjoint formulation

In order to derive the optimality condition (4.2), we would have to compute a partial derivative in multiple directions, which is inconvenient. Therefore, we use an adjoint formulation, see, e.g., [8, 35, 82].

Definition 4.1.1. *Define a Lagrangian*

$$\mathcal{L} \ : \ \boldsymbol{H}(\hat{Y},\hat{\Sigma}) \times \boldsymbol{H}(\hat{Y},\hat{\Sigma}) \times \boldsymbol{D}(\hat{Y},\hat{\Sigma}) \to \mathbb{C},$$

$$\mathcal{L}(\hat{\boldsymbol{\chi}},\hat{\boldsymbol{z}};\hat{\boldsymbol{q}}) = C(\hat{\boldsymbol{\chi}};\hat{\boldsymbol{q}}) - E(\hat{\boldsymbol{\chi}},\hat{\boldsymbol{z}};\hat{\boldsymbol{q}}),$$

where we have introduced a Lagrange multiplier $\hat{\boldsymbol{z}}$ for the PDE constraint in (4.2)*. For a given deformation field $\hat{\boldsymbol{q}} \in H_0^1(\hat{Y},\mathbb{C})^3$ we further introduce a state equation:*

$$\textit{find } \hat{\boldsymbol{\chi}} \in \boldsymbol{H}(\hat{Y},\hat{\Sigma}) \ \textit{s. t. } \ \mathcal{L}'_{\hat{\boldsymbol{z}}}(\hat{\boldsymbol{\chi}},\hat{\boldsymbol{z}};\hat{\boldsymbol{q}})[\delta\hat{\boldsymbol{z}}] = 0 \ \ \forall \delta\hat{\boldsymbol{z}} \in \boldsymbol{H}(\hat{Y},\hat{\Sigma}) \tag{4.3}$$

and denote the solution of the state equation by $\hat{\boldsymbol{\chi}}(\hat{\boldsymbol{q}})$. Here, $\mathcal{F}'_{\hat{\boldsymbol{z}}}[\delta\hat{\boldsymbol{z}}]$ denotes the Gâteaux

derivative of a functional F with respect to $\hat{\boldsymbol{z}}$ in direction $\delta\hat{\boldsymbol{z}}$. We then introduce an adjoint equation:

$$\textit{find } \hat{\boldsymbol{z}} \in \boldsymbol{H}(\hat{Y},\hat{\Sigma}) \textit{ s.t. } \mathcal{L}'_{\hat{\boldsymbol{\chi}}}(\hat{\boldsymbol{\chi}}(\hat{\boldsymbol{q}}),\hat{\boldsymbol{z}};\hat{\boldsymbol{q}})[\delta\hat{\boldsymbol{\chi}}] = 0 \ \ \forall \delta\hat{\boldsymbol{\chi}} \in \boldsymbol{H}(\hat{Y},\hat{\Sigma}). \tag{4.4}$$

The central observation is the fact that a solution to (4.2) is a critical point of $\mathcal{L}(\hat{\boldsymbol{\chi}},\hat{\boldsymbol{z}};\hat{\boldsymbol{q}})$; see [8, 35, 82]. For the sake of completeness we summarize:

Lemma 4.1.2 (First order necessary conditions [8, 35, 82])**.** *The solution $(\hat{\boldsymbol{\chi}}^*,\hat{\boldsymbol{q}}^*)$ of (4.2) coincides with a critical point $(\hat{\boldsymbol{\chi}}^*,\hat{\boldsymbol{z}}^*,\hat{\boldsymbol{q}}^*)$ of the Lagrangian $\mathcal{L}(\hat{\boldsymbol{\chi}},\hat{\boldsymbol{z}};\hat{\boldsymbol{q}})$.*

Proof. Let $(\hat{\boldsymbol{\chi}}^*,\hat{\boldsymbol{q}}^*)$ be a solution to (4.2) and let $\hat{\boldsymbol{z}}^*$ be the solution to the adjoint equation (4.4). We then have $\mathcal{L}'_{\hat{\boldsymbol{z}}}(\hat{\boldsymbol{\chi}}^*,\hat{\boldsymbol{z}}^*;\hat{\boldsymbol{q}}^*)[\delta\hat{\boldsymbol{z}}] = 0$ and $\mathcal{L}'_{\hat{\boldsymbol{\chi}}}(\hat{\boldsymbol{\chi}}^*,\hat{\boldsymbol{z}}^*;\hat{\boldsymbol{q}}^*)[\delta\hat{\boldsymbol{\chi}}] = 0$ by virtue of (4.3) and (4.4).

For an arbitrary deformation $\hat{\boldsymbol{q}} \in \boldsymbol{D}(\hat{Y},\hat{\Sigma})$ let $\hat{\boldsymbol{\chi}}(\hat{\boldsymbol{q}})$ denote the unique solution to the state equation (4.3), as well as $\hat{\boldsymbol{z}}(\hat{\boldsymbol{q}})$ denote the unique solution to the adjoint equation (4.4). We now introduce the functional $c(\hat{\boldsymbol{q}}) := C(\hat{\boldsymbol{\chi}}(\hat{\boldsymbol{q}});\hat{\boldsymbol{q}}) = \mathcal{L}(\hat{\boldsymbol{\chi}}(\hat{\boldsymbol{q}}),\hat{\boldsymbol{z}}(\hat{\boldsymbol{q}});\hat{\boldsymbol{q}})$ and make the observation that $\hat{\boldsymbol{q}}$, by virtue of being an optimum, is necessarily a critical point of $c(\hat{\boldsymbol{q}})$, i. e., $c'_{\hat{\boldsymbol{q}}}(\hat{\boldsymbol{q}})[\delta\hat{\boldsymbol{q}}] = 0$ for all $\delta\hat{\boldsymbol{q}} \in \boldsymbol{D}(\hat{Y},\hat{\Sigma})$. Using above identity and the chain rule we get for all $\delta\hat{\boldsymbol{q}} \in \boldsymbol{D}(\hat{Y},\hat{\Sigma})$:

$$\begin{aligned} 0 &= c'(\hat{\boldsymbol{q}})[\delta\hat{\boldsymbol{q}}] \\ &= \mathcal{L}'_{\hat{\boldsymbol{\chi}}}(\hat{\boldsymbol{\chi}}(\hat{\boldsymbol{q}}),\hat{\boldsymbol{z}}(\hat{\boldsymbol{q}});\hat{\boldsymbol{q}})\big[\hat{\boldsymbol{\chi}}'_{\hat{\boldsymbol{q}}}(\hat{\boldsymbol{q}})[\delta\hat{\boldsymbol{q}}]\big] + \mathcal{L}'_{\hat{\boldsymbol{z}}}(\hat{\boldsymbol{\chi}}(\hat{\boldsymbol{q}}),\hat{\boldsymbol{z}}(\hat{\boldsymbol{q}});\hat{\boldsymbol{q}})[\hat{\boldsymbol{z}}'(\hat{\boldsymbol{q}})[\delta\hat{\boldsymbol{q}}]] \\ &\quad + \mathcal{L}'_{\hat{\boldsymbol{q}}}(\hat{\boldsymbol{\chi}}(\hat{\boldsymbol{q}}),\hat{\boldsymbol{z}}(\hat{\boldsymbol{q}});\hat{\boldsymbol{q}})[\delta\hat{\boldsymbol{q}}] \\ &= \mathcal{L}'_{\hat{\boldsymbol{q}}}(\hat{\boldsymbol{\chi}}(\hat{\boldsymbol{q}}),\hat{\boldsymbol{z}}(\hat{\boldsymbol{q}});\hat{\boldsymbol{q}})[\delta\hat{\boldsymbol{q}}], \end{aligned} \tag{4.5}$$

where for the last equality we have exploited the fact that the first two terms vanish due to $\hat{\boldsymbol{\chi}}(\hat{\boldsymbol{q}})$ and $\hat{\boldsymbol{z}}(\hat{\boldsymbol{q}})$ solving the state and adjoint equations, respectively. $(\hat{\boldsymbol{\chi}}^*,\hat{\boldsymbol{z}}^*,\hat{\boldsymbol{q}}^*)$ is thus a critical point of the Lagrangian $\mathcal{L}(\hat{\boldsymbol{\chi}},\hat{\boldsymbol{z}};\hat{\boldsymbol{q}})$. □

The previous lemma is based on the fact the Lagrangian $\mathcal{L}$ can be used to describe the derivative of $c(\hat{\boldsymbol{q}})$ [8, 35, 82]; for all $\delta\hat{\boldsymbol{q}} \in \boldsymbol{D}(\hat{Y}, \hat{\Sigma})$:

$$c'(\hat{\boldsymbol{q}})[\delta\hat{\boldsymbol{q}}] \;=\; \mathcal{L}'_{\hat{\boldsymbol{q}}}(\hat{\boldsymbol{\chi}}(\hat{\boldsymbol{q}}), \hat{\boldsymbol{z}}(\hat{\boldsymbol{q}}); \hat{\boldsymbol{q}})[\delta\hat{\boldsymbol{q}}].$$

We will make use of this result in the numerical algorithm to compute a gradient direction for the deformation. Noting that $c'(\hat{\boldsymbol{q}})$ is an element of the dual space of $H_0^1(\hat{Y}, \mathbb{C})^3$, we find the Riesz-representation, or gradient, as follows:

Definition 4.1.3 (Gradient equation)**.** *Given a deformation field $\hat{\boldsymbol{q}}$ and corresponding $\hat{\boldsymbol{z}}(\hat{\boldsymbol{q}})$, $\hat{\boldsymbol{\chi}}(\hat{\boldsymbol{q}})$ given by* (4.3) *and* (4.4)*, we find $\boldsymbol{\delta c}(\hat{\boldsymbol{q}}) \in \boldsymbol{D}(\hat{Y}, \hat{\Sigma})$ by solving the* gradient equation

$$\int_{\hat{Y}} \nabla\boldsymbol{\delta c}(\hat{\boldsymbol{q}}) \cdot \nabla\delta\hat{\boldsymbol{q}} \,\mathrm{d}\hat{y} \;=\; \mathcal{L}'_{\hat{\boldsymbol{q}}}(\hat{\boldsymbol{\chi}}(\hat{\boldsymbol{q}}), \hat{\boldsymbol{z}}(\hat{\boldsymbol{q}}); \hat{\boldsymbol{q}})[\delta\hat{\boldsymbol{q}}] \qquad \forall\delta\hat{\boldsymbol{q}} \in \boldsymbol{D}(\hat{Y}, \hat{\Sigma}). \tag{4.6}$$

4.2 Methods of numerical optimization

The optimization problem discussed in this thesis uses *gradient descent* and *BFGS* and in this section, we provide an overview of the algorithms used in our numerical algorithms. Gradient descent is a first-order iterative method that minimizes the gradient of the objective function, which in our case is $c(\hat{\boldsymbol{q}})$. As discussed, we use the *gradient equation* (4.6) to compute the derivative $c'(\hat{\boldsymbol{q}})$ using the Reisz representation theorem. Algorithm 1 is computing the gradient using the adjoint approach,

Algorithm 1 Computing the H^1-gradient $\boldsymbol{\delta c}(\hat{\boldsymbol{q}})$ of the cost functional $c(\hat{\boldsymbol{q}})$ by means of the adjoint formulation; see Lemma 4.1.2.

Given $\hat{\boldsymbol{q}} \in \boldsymbol{D}(\hat{Y}, \hat{\Sigma})$

a) compute a solution $\hat{\boldsymbol{\chi}}(\hat{\boldsymbol{q}}) \in \boldsymbol{H}(\hat{Y}, \hat{\Sigma})$ of the state equation (4.3),

$$\mathcal{L}'_{\hat{\boldsymbol{z}}}(\hat{\boldsymbol{\chi}}, \hat{\boldsymbol{z}}; \hat{\boldsymbol{q}})[\delta\hat{\boldsymbol{z}}] = -E(\hat{\boldsymbol{\chi}}, \delta\hat{\boldsymbol{z}}; \hat{\boldsymbol{q}}) = 0 \ \ \forall \delta\hat{\boldsymbol{z}} \in \boldsymbol{H}(\hat{Y}, \hat{\Sigma});$$

b) compute a solution $\hat{\boldsymbol{z}}(\hat{\boldsymbol{q}})$ of the adjoint equation (4.4),

$$\mathcal{L}'_{\hat{\boldsymbol{\chi}}}(\hat{\boldsymbol{\chi}}(\hat{\boldsymbol{q}}), \hat{\boldsymbol{z}}; \hat{\boldsymbol{q}})[\delta\hat{\boldsymbol{\chi}}] = 0 \ \ \forall \delta\hat{\boldsymbol{\chi}} \in \boldsymbol{H}(\hat{Y}, \hat{\Sigma});$$

c) solve the gradient equation (4.6),

$$\int_{\hat{Y}} \nabla \boldsymbol{\delta c}(\hat{\boldsymbol{q}}) \cdot \nabla \delta\hat{\boldsymbol{q}} \, \mathrm{d}\hat{y} \ = \ \mathcal{L}'_{\hat{\boldsymbol{q}}}(\hat{\boldsymbol{\chi}}(\hat{\boldsymbol{q}}), \hat{\boldsymbol{z}}(\hat{\boldsymbol{q}}); \hat{\boldsymbol{q}})[\delta\hat{\boldsymbol{q}}] \qquad \forall \delta\hat{\boldsymbol{q}} \in \boldsymbol{D}(\hat{Y}, \hat{\Sigma}).$$

Return $\boldsymbol{\delta c}(\hat{\boldsymbol{q}})$.

BFGS (Broyden-Fletcher-Goldfarb-Shanno) is a quasi-Newton method that approximates the inverse Hessian to minimize the cost function. We use a slight modification of BFGS, and algorithm 2 provides an overview of our methods. The modified method still approximates the inverse Hessian and introduces *a damping*, which is utilized to allow the use of an Armijo backtracking linesearch within the optimization while still guaranteeing positive definiteness of the approximate inverse Hessian [34]. The proof of the positive definiteness remaining intact is omitted here and we refer the reader to [34] for a detailed description and analysis of the *inverse damped BFGS* method.

Also, note here that the pseudo-code for the algorithm uses the discretized version of the cost function and Lagrangian $(c_h(\hat{\boldsymbol{q}}), \mathcal{L}_{h,\hat{\boldsymbol{q}}})$, however the discretization itself is described in more detail in Chapter 5.

Algorithm 2 The inverse damped BFGS algorithm for finding an approximate solution $\hat{\boldsymbol{q}}_h^*$ of the optimization problem (4.2).

Given an initial guess $\hat{\boldsymbol{q}}_h^0 \in \boldsymbol{D}_h$ and an initial approximate inverse Hessian operator $B^0 \in \mathcal{L}(\boldsymbol{D}_h, \boldsymbol{D}_h)$ iterate:

a) Compute the gradient $\boldsymbol{\delta c}_h(\hat{\boldsymbol{q}}_h^n) \in \boldsymbol{D}_h$ with Algorithm 1, and obtain a search direction $\boldsymbol{p}^n \in \boldsymbol{D}_h$ by setting

$$\boldsymbol{p}^n = -B^n \boldsymbol{\delta c}_h(\hat{\boldsymbol{q}}_h^n).$$

b) Perform an Armijo backtracking line search with parameters $\beta \in (0,1)$ and $\gamma \in (0,1/2)$ to find the maximal $\lambda^n \in \{1, \beta, \beta^2, \ldots\}$ satisfying the *Armijo condition* $\boldsymbol{c}_h(\hat{\boldsymbol{q}}_h^n + \lambda^n \boldsymbol{p}^n) \leq \boldsymbol{c}_h(\hat{\boldsymbol{q}}_h^n) + \gamma \lambda^n (\nabla \boldsymbol{\delta c}_h(\hat{\boldsymbol{q}}_h^n), \nabla p^n)$. Then, update

$$\boldsymbol{s}^n := \lambda^n \boldsymbol{p}^n, \quad \hat{\boldsymbol{q}}_h^{n+1} = \hat{\boldsymbol{q}}_h^n + \boldsymbol{s}^n.$$

c) Update the approximate inverse Hessian matrix using a damped inverse BFGS update formula derived in [34] to assert positive definiteness of the operator B^{n+1}. To this end, compute

$$\boldsymbol{y}^n = \boldsymbol{\delta c}_h(\hat{\boldsymbol{q}}_h^{n+1}) - \boldsymbol{\delta c}_h(\hat{\boldsymbol{q}}_h^n).$$

Define a scaling parameter

$$\theta_n = \begin{cases} 1 & (\nabla \boldsymbol{y}^n, \nabla \boldsymbol{s}^n) \geq 0.2 (\nabla \boldsymbol{y}^n, \nabla B^n \boldsymbol{y}^n), \\ 0.8 \frac{(\nabla \boldsymbol{y}^n, \nabla B^n \boldsymbol{y}^n)}{(\nabla \boldsymbol{y}^n, \nabla B^n \boldsymbol{y}^n) - (\nabla \boldsymbol{y}^n, \nabla \boldsymbol{s}^n)} & \text{otherwise,} \end{cases}$$

and with $\widehat{\boldsymbol{s}}^n = \theta_n \boldsymbol{s}^n + (1-\theta_n) B^n \boldsymbol{y}^n$ set

$$\begin{aligned} B^{n+1} \;=\; B^n + \frac{(\widehat{\boldsymbol{s}}^n - B^n \boldsymbol{y}^n)(\nabla \widehat{\boldsymbol{s}}^n, \nabla \cdot) + \widehat{\boldsymbol{s}}^n (\nabla (\widehat{\boldsymbol{s}}^n - B^n \boldsymbol{y}^n), \nabla \cdot)}{(\nabla \boldsymbol{y}^n, \nabla \widehat{\boldsymbol{s}}^n)} \\ - \frac{(\nabla (\widehat{\boldsymbol{s}}^n - B^n \boldsymbol{y}^n), \nabla \boldsymbol{y}^n)}{(\nabla \boldsymbol{y}^n, \nabla \widehat{\boldsymbol{s}}^n)^2} \widehat{\boldsymbol{s}}^n (\nabla \widehat{\boldsymbol{s}}^n, \nabla \cdot), \end{aligned}$$

where, of course, the matrix corresponding to the operator B^{n+1} is never constructed directly. Instead, the application of B^{n+1} to the direction $\boldsymbol{\delta c}_h(\hat{\boldsymbol{q}}_h^n)$ is computed by storing the vectors $\widehat{\boldsymbol{s}}^n$ and $B^n \boldsymbol{y}^n$.

d) If the stopping criterion was reached, return $\hat{\boldsymbol{q}}_h^{n+1}$, otherwise continue at (a).

5. COMPUTATIONAL FRAMEWORK AND NUMERICAL ILLUSTRATIONS*

For our numerical tests we use the optimization toolkit `DOpElib` [28] which is based on the finite element library `deal.II` [6, 7]. The library supports a variety of finite element formulations based on quadrilateral (in 2D) and hexahedrical (in 3D) meshes.

5.1 Finite element discretization and optimization framework

For our numerical tests we use the optimization toolkit `DOpElib` [28] which is based on the finite element library `deal.II` [6, 7]. The library supports a variety of finite element formulations based on quadrilateral (in 2d) and hexahedrical (in 3d) meshes.

Let $\mathcal{T}_h$ be a partition of $\hat{Y}$ into shape-regular (quadrilateral or) hexahedral elements that are *fitted* to the hypersurface $\hat{\Sigma}$. This is to say, we make the assumption that every element that is intersected by $\hat{\Sigma}$ has a face for which all four vertices of the face are located on $\hat{\Sigma}$. We denote by $\hat{\Sigma}_h$ the set of all faces for which all vertices of the face are located on $\hat{\Sigma}$. By slight abuse of notation we will interpret $\hat{\Sigma}_h$ either as a collection of faces or as the polyhedral hypersurface created by the union of all faces. We denote by $\{\phi_i^h\}_{i=1}^{\mathcal{N}}$ the Lagrange basis of $\mathbb{Q}_1(\mathcal{T}_h)$, the space of piecewise (bilinear) trilinear finite elements defined on $\mathcal{T}_h$. Note that the tangential derivative $\hat{\nabla}_{\hat{\mathbf{t}}}\varphi$ on a face $f \in \hat{\Sigma}_h$ of a finite element function $\varphi \in \mathbb{Q}_1(\mathcal{T}_h)$ is single valued.

We can thus introduce a discrete bilinear form corresponding to (3.10):

$$E_h(\hat{\boldsymbol{\chi}}_h, \hat{\boldsymbol{\varphi}}_h; \hat{\boldsymbol{q}}_h) := \int_{\hat{Y}} \hat{\varepsilon}_h(\boldsymbol{x}, \hat{\boldsymbol{y}}) \big(\hat{F}_h(\hat{\boldsymbol{y}})^T + \hat{\nabla}\hat{\boldsymbol{\chi}}_h^T\big) \cdot \hat{\nabla}\hat{\boldsymbol{\varphi}}_h^T \, \mathrm{d}\hat{y} \\ - \frac{1}{i\omega} \int_{\hat{\Sigma}_h} \hat{\sigma}_h(\boldsymbol{x}, \hat{\boldsymbol{y}}) \big((\hat{F}_h(\hat{\boldsymbol{y}})^T)_{\hat{\mathbf{t}}} + \hat{\nabla}_{\hat{\mathbf{t}}}\hat{\boldsymbol{\chi}}_h^T\big) \cdot \hat{\nabla}_{\hat{\mathbf{t}}}\hat{\boldsymbol{\varphi}}_h^T \, \mathrm{d}\hat{o}_{\hat{y}}, \quad (5.1)$$

for $\hat{\boldsymbol{\chi}}_h, \hat{\boldsymbol{\varphi}}_h \in \boldsymbol{H}_h := \mathbb{Q}_1(\mathcal{T})^{2\times 3}$ and $\hat{\boldsymbol{q}}_h \in \boldsymbol{D}_h := \mathbb{Q}_1(\mathcal{T})^3$.

Here, $\hat{\varepsilon}_h$, $\hat{\sigma}_h$ and $\hat{F}_h$ are computed with respect to the discrete objects $\hat{\boldsymbol{q}}_h$ and $\hat{\Sigma}_h$.

*Part of this chapter is reprinted with permission from M. Bezbaruah, M. Maier, and W. Wollner, "Shape optimization of optical microscale inclusions," *SIAM Journal on Scientific Computing*, vol. 46, no. 4, pp. B377-B402, 2024.

Similarly, we introduce a discrete counterpart $\varepsilon_h^{\text{eff}}$ of the effective permittivity tensor given by (3.11) and we set

$$C_h(\hat{\boldsymbol{\chi}}_h;\hat{\boldsymbol{q}}_h) := \frac{1}{2}\left\|\varepsilon_h^{\text{eff}}(\hat{\boldsymbol{\chi}}_h;\hat{\boldsymbol{q}}_h)-\varepsilon^{\text{trgt}}\right\|_{\text{Fr.}}^2+\frac{\alpha}{2}\left\|\nabla\hat{\boldsymbol{q}}_h\right\|_{w_h}^2+\beta\int_{\hat{Y}}P(\hat{\boldsymbol{y}};\hat{\boldsymbol{q}}_h)\,\mathrm{d}\hat{y}. \tag{5.2}$$

Here, we choose the following weight function in order to penalize more the deformation gradient on mesh cells at the interface that ensures that the discrete interface Σ_h retains a sufficient degree of smoothness:

$$w_h(\hat{\boldsymbol{y}})=\begin{cases}1+\alpha_\Sigma/\mathrm{diam}K & \text{for } \hat{\boldsymbol{y}}\in K \text{ with } \partial K\cap\delta\Sigma_h\neq\emptyset,\\ 1 & \text{otherwise.}\end{cases}$$

By introducing a discrete Lagrangian,

$$\mathcal{L}_h \;:\; \boldsymbol{H}_h\times\boldsymbol{H}_h\times\boldsymbol{D}_h\to\mathbb{C},$$

$$\mathcal{L}(\hat{\boldsymbol{\chi}}_h,\hat{\boldsymbol{z}}_h;\hat{\boldsymbol{q}}_h)=C_h(\hat{\boldsymbol{\chi}};\hat{\boldsymbol{q}})-E_h(\hat{\boldsymbol{\chi}},\hat{\boldsymbol{z}};\hat{\boldsymbol{q}}),$$

we are now in a position to use the adjoint formulation to compute a discrete gradient [28]; see Algorithm 1. We use an inverse BFGS algorithm with damping as proposed in [34] to find an approximate minimum of $C_h(\hat{\boldsymbol{q}}_h)$; see Algorithm 2. The λ^n in the above algorithm is the step size it is chosen by an Armijo backtracking linesearch and changes at every iteration. As mentioned, B^n is an approximate inverse Hessian matrix. The update procedure in Algorithm 2(c) ensures that B^{n+1} remains symmetric and positive definite. The initial value B^0 is chosen as,

$$B_0=\frac{-1}{\alpha}\Delta_h^{-1}\colon\boldsymbol{D}_h\to\boldsymbol{D}_h$$

in order to exactly recover the inverse Hessian of the control cost as suggested by the local convergence theory outlined in [29, 40].

5.2 Numerical illustrations

In this section, we discuss a number of numerical results to illustrate the performance of the shape optimization algorithm. We implemented the algorithm in a small C++ code using the optimization toolkit `DOpElib` [28] which is based on the finite element library `deal.II` [6, 7]. We have made our source code publicly available on Zenodo [9]. For the sake of simplicity we restrict our numerical computations to 2D by assuming translation invariance in the z-direction. Then, the cell problem (3.7) and the averaging (3.6) reduce to a 2D problem. Throughout the section we have chosen $\varepsilon = \boldsymbol{I}$ and the surface conductivity to be given by (2.6) with a fixed frequency of either $\omega = 0.3$, or $\omega = 0.5$. The reference geometry consists of an inscribed circle $\hat{\Sigma}$ at the center of $\hat{Y} = [0,1]^2$ with a radius of $r = 0.3$; see Figure 3.1. We have chosen a fixed spatial discretization $\mathcal{T}_h$ of 53 248 quadrilaterals (fitted to the hypersurface $\hat{\Sigma}$) which amounts to 429 062 degrees of freedom for the (complex tensor-valued) state problem and 107 266 for the (vector-valued) control problem.

5.2.1 Influence of the regularization parameters

We first present a parameter study to assess the influence of the regularization parameters α and β found in (4.1) on the target tensor ε^{eff} and the deformation field $\hat{\boldsymbol{q}}$. The optimization problem without stabilization terms in (4.1) is highly ill-posed; the main reason being the fact that the deformation vector $\hat{\boldsymbol{q}}$ has no influence on the target functional away from the interface $\hat{\Sigma}$. Thus, a reasonable amount of penalization is required to (a) ensure consistent mesh regularity (i. e. $\hat{J}$ being reasonably close to 1), and (b) allow the geometry to deform sufficiently to actually obtain an effective tensor $\varepsilon^{\text{eff}}(\hat{\boldsymbol{\chi}}, \hat{\boldsymbol{q}})$ close to the target $\varepsilon^{\text{target}}$. For the parameter study we choose a target permittivity tensor of

$$\varepsilon^{\text{target}} = \begin{pmatrix} 0.8 + 0.008\mathrm{i} & 0.05 \\ 0.05 & 0.8 + 0.008\mathrm{i} \end{pmatrix},$$

`https://zenodo.org/records/10459309`

$\boldsymbol{\beta}$	$\boldsymbol{\alpha}$	$\boldsymbol{\alpha}_\Sigma$	$\varepsilon_{xx}^{\text{eff}}$	$\varepsilon_{xy}^{\text{eff}}$	deviation	optimality
0.2	0.01	10	$0.8244 + 0.0200\text{i}$	$0.0444 - 0.0174\text{i}$	4.63%	0.00503
0.2	0.001	100	$0.8233 + 0.0202\text{i}$	$0.0441 - 0.0170\text{i}$	4.51%	0.00739
0.2	0.001	10	$0.8057 + 0.0133\text{i}$	$0.0484 - 0.0090\text{i}$	1.70%	0.00890
0.1	0.01	10	$0.8239 + 0.0204\text{i}$	$0.0440 - 0.0174\text{i}$	4.61%	0.02082
0.1	0.001	100	$0.8230 + 0.0206\text{i}$	$0.0438 - 0.0171\text{i}$	4.51%	0.02598
0.1	0.001	10	$0.8052 + 0.0140\text{i}$	$0.0481 - 0.0090\text{i}$	1.72%	0.01366
0.05	0.01	10	$0.8235 + 0.0207\text{i}$	$0.0438 - 0.0173\text{i}$	4.59%	0.02360
0.05	0.001	100	$0.8228 + 0.0209\text{i}$	$0.0436 - 0.0170\text{i}$	4.51%	0.07232
0.05	0.001	10	$0.8049 + 0.0145\text{i}$	$0.0480 - 0.0090\text{i}$	1.73%	0.00472

Table 5.1: Diagonal and off-diagonal components of $\varepsilon^{\text{eff}}(\hat{\boldsymbol{\chi}}, \hat{\boldsymbol{q}})$, relative deviation $\left\|\varepsilon^{\text{eff}} - \varepsilon^{\text{target}}\right\|_{\text{Fr.}} / \left\|\varepsilon^{\text{target}}\right\|_{\text{Fr.}}$, optimality, i. e., relative norm of the reduced gradient, for different values of stabilization parameters β, α and α_Σ (rows). Results are shown for a fixed number of 200 iterations of the BFGS algorithm 2. The initial deviation was 10.97%.

$\boldsymbol{\beta}$	$\boldsymbol{\alpha}$	$\boldsymbol{\alpha}_\Sigma$	$\varepsilon_{xx}^{\text{eff}}$	$\varepsilon_{xy}^{\text{eff}}$	deviation	optimality
0.2	0.001	10	$0.8057 + 0.0135\text{i}$	$0.0483 - 0.0092\text{i}$	1.73%	0.00667
0.1	0.001	10	$0.8052 + 0.0141\text{i}$	$0.0481 - 0.0092\text{i}$	1.74%	0.00747
0.05	0.001	10	$0.8048 + 0.0145\text{i}$	$0.0480 - 0.0091\text{i}$	1.75%	0.00533

Table 5.2: Subset of the parameter study reported in Table 5.1 but with 5 instead of 6 global refinement steps resulting in 13 312 quadrilaterals which amounts to 108 040 degrees of freedom for the (complex tensor-valued) state problem and in 27 010 for the (vector-valued) control problem.

which has a moderate initial relative deviation $\left\|\varepsilon^{\text{eff}} - \varepsilon^{\text{target}}\right\|_{\text{Fr.}} / \left\|\varepsilon^{\text{target}}\right\|_{\text{Fr.}}$ of around 10.97%. We choose to perform a fixed number of 200 steps of Algorithm 2 without an active stopping criterion. Results for varying degrees of regularization $\alpha = 0.01,\ 0.001$, $\alpha_\Sigma = 10,\ 100$, and $\beta = 0.2,\ 0.1,\ 0.05$ are reported in Table 5.1. We see in the above experiments that the combination of α and α_Σ have the largest influence on the achieved deviation from the target tensor. Lower values of the stabilization parameters result in smaller deviations; see Table 5.1. As a last figure of merit we also report the achieved *optimality*, i. e., the norm of the reduced gradient normalized over the initial value: $\|\boldsymbol{\delta c}_h(\hat{\boldsymbol{q}}_h^n)\| / \|\boldsymbol{\delta c}_h(\hat{\boldsymbol{q}}_h^0)\|$ for the final step $n = 200$. Here, we observe that the highest reduction after 200 steps with an optimality

of around 0.005 is achieved for the choice $\alpha = 0.001$, $\alpha_\Sigma = 10$, $\beta = 0.05$. However, if the stabilization parameters are chosen too small, the mesh can degrade, in particular near the edges of the interface Σ_h. Thus, in order to balance both these factors, we make a conservative choice of $\alpha = 0.001$, $\alpha_\Sigma = 10$ and $\beta = 0.1$ for all subsequent numerical tests.

As a final test we examine the influence of mesh refinement on the numerical result and rerun the case of $\alpha = 0.001$, $\alpha_\Sigma = 10$ and $\beta = 0.2$, 0.1, 0.05 with a lower resolution of 13 312 quadrilaterals resulting in 108 040 degrees of freedom for the (complex tensor-valued) state problem and in 27 010 for the (vector-valued) control problem; see Table 5.2. The final ε^{eff} values after 200 iterations are very close to the results obtained for 6 global refinement steps; cf Table 5.1. We conclude that the chosen resolution of 53 248 quadrilaterals is appropriate with minimal influence on the optimization result.

5.2.2 Optimizing an epsilon-near-zero material

We now illustrate the shape optimization procedure for three different target permittivity tensors given by

$$\varepsilon^{\text{target}} = \begin{pmatrix} * & 0.05 \\ 0.05 & 0.5 + 0.01\text{i} \end{pmatrix},$$

where we vary the $\varepsilon_{xx}^{\text{target}}$ component from (a) $0.5 + 0.01\text{i}$, (b) $0.25 + 0.005\text{i}$, to (c) 0.0. The target tensor has been chosen close to the initial permittivity tensor of

$$\varepsilon_{\text{ref}}^{\text{eff}} = \begin{pmatrix} 0.50304 + 0.01114\text{i} & 0.0 \\ 0.0 & 0.50304 + 0.01114\text{i} \end{pmatrix},$$

obtained for the reference configuration with frequency $\omega = 0.3$.

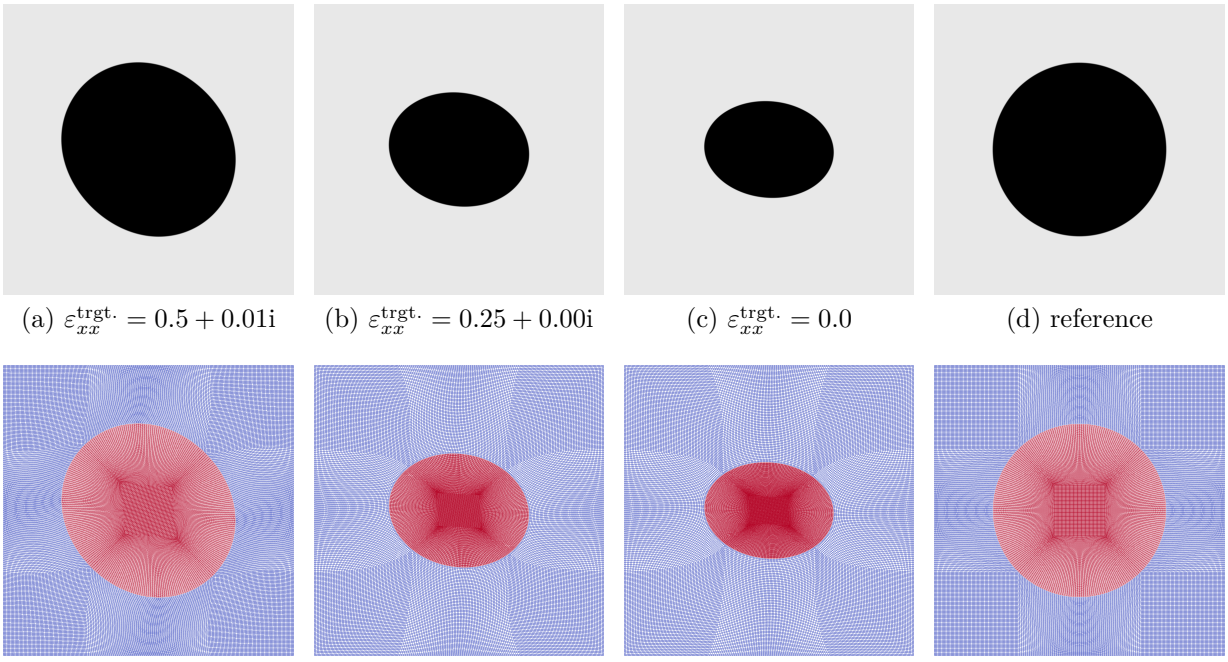

(a) $\varepsilon_{xx}^{\text{trgt.}} = 0.5 + 0.01\text{i}$ (b) $\varepsilon_{xx}^{\text{trgt.}} = 0.25 + 0.00\text{i}$ (c) $\varepsilon_{xx}^{\text{trgt.}} = 0.0$ (d) reference

(e) $\varepsilon_{xx}^{\text{trgt.}} = 0.5 + 0.01\text{i}$ (f) $\varepsilon_{xx}^{\text{trgt.}} = 0.25 + 0.00\text{i}$ (g) $\varepsilon_{xx}^{\text{trgt.}} = 0.0$ (h) reference

Figure 5.1: Epsilon-near-zero testcase: Final geometry obtained for target cases (a), (b) and (c) with increasingly smaller $\varepsilon_{xx}^{\text{target}}$ component. The corresponding deformed (and initial) meshes are shown in (e)-(h). The black region in (a)-(d), as well as the red region in (e)-(h) show the volume surrounded by the interface Σ_h. Reprinted with permission from [9].

	$\varepsilon_{xx}^{\text{eff}}$	$\varepsilon_{xy}^{\text{eff}}$	$\varepsilon_{yy}^{\text{eff}}$	initial	final	steps
ref.	$0.5030 + 0.011\text{i}$	$0.0 - 0.0\text{i}$	$0.5030 + 0.011\text{i}$			
(a)	$0.5041 + 0.011\text{i}$	$0.0488 - 0.001\text{i}$	$0.5041 + 0.011\text{i}$	7.09%	0.65%	263
(b)	$0.2897 + 0.027\text{i}$	$0.0486 - 0.002\text{i}$	$0.5285 + 0.016\text{i}$	26.3%	5.40%	2047
(c)	$0.0271 + 0.054\text{i}$	$0.0493 - 0.003\text{i}$	$0.5161 + 0.021\text{i}$	50.8%	6.36%	2977

Table 5.3: Epsilon-near-zero testcase: Final permittivity tensors obtained for target cases (a), (b), (c), and the starting value for the undeformed reference configuration. In addition, we report the initial and final deviation $\left\|\varepsilon^{\text{eff}} - \varepsilon^{\text{target}}\right\|_{\text{Fr.}} / \left\|\varepsilon^{\text{target}}\right\|_{\text{Fr.}}$, as well as the number of BFGS iterations in Algorithm 2 needed to achieve convergence.

As the target vector gradually gets closer to an epsilon-near-zero material [58, 61] an increasingly larger mesh deformation is required to achieve an optimal configuration. We chose to add an off-diagonal value of 0.05 in the target permittivity tensor to force an increased interaction between the x- and y-directions. For our numerical computation we use the stabilization parameters discussed in Section 5.2.1 and a stopping criterion to achieve a reduction of the reduced gradient, viz. $\|\boldsymbol{\delta c}_h(\hat{\boldsymbol{q}}_h^n)\|/\|\boldsymbol{\delta c}_h(\hat{\boldsymbol{q}}_h^0)\|$, of better than 10^{-4}.

The initial and final geometry is illustrated in Figure 5.1. It can be seen that proceeding from case (a) to (c) an increasingly larger mesh deformation is required, the shapes remain largely elliptic. The final permittivity tensor values and deviation are given in Table 5.3. With the chosen stabilization parameters we were able to improve the initial deviation to our target tensor consistently by an order of magnitude.

Remark 5.2.1. *We point out that it does not seem possible in general to achieve a deviation of zero for arbitrary target permittivities [58]. This is largely due to the fact that the effective permittivity tensor $\varepsilon^{\mathit{eff}}$ as a function of shape and frequency possesses a well defined structure that does not allow to tune all components and the real and imaginary part arbitrarily; see [58].*

In Figure 5.2 we report the evolution of the optimality, $\|\boldsymbol{\delta c}_h(\hat{\boldsymbol{q}}_h^n)\|/\|\boldsymbol{\delta c}_h(\hat{\boldsymbol{q}}_h^0)\|$, during the solution process. We note that with the larger deformation necessary for cases (b) and (c) a significant increase in the number of required steps to achieve convergence can be observed. As a final figure of merit we examine the evolution of the deviation, $\left\|\varepsilon^{\mathrm{eff}} - \varepsilon^{\mathrm{target}}\right\|_{\mathrm{Fr.}} / \left\|\varepsilon^{\mathrm{target}}\right\|_{\mathrm{Fr.}}$, during the solution process; see Figure 5.3. We observe that the deviation converges to its final value very fast (in between 10 to 100 steps) which corresponds to the initial steep slope for the optimality; cf. Figure 5.2. The remaining steps are then spend on further minimizing the penalty and thus improving the overall mesh quality.

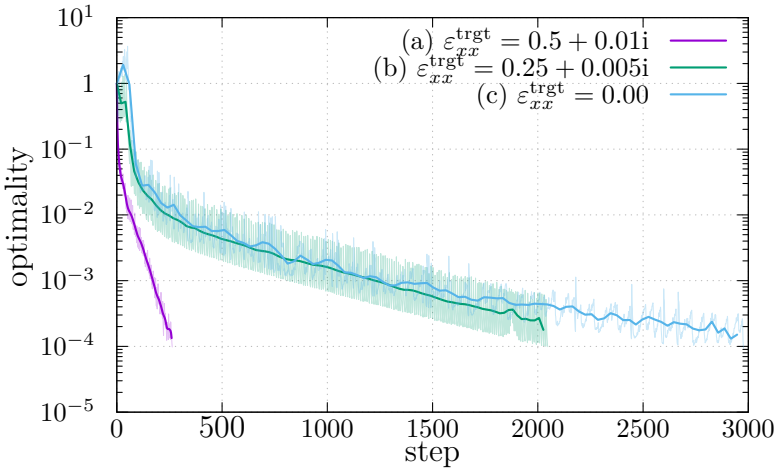

Figure 5.2: Evolution of the optimality, $\|\boldsymbol{\delta c}_h(\hat{\boldsymbol{q}}_h^n)\|/\|\boldsymbol{\delta c}_h(\hat{\boldsymbol{q}}_h^0)\|$, during the BFGS solution process for the three cases (a) $0.5 + 0.01\mathrm{i}$, (b) $0.25 + 0.005\mathrm{i}$, to (c) 0.0. The thick line for each case is a smoothed Bezier curve (gnuplot builtin) that is overlayed over the actual, oscillatory value. Reprinted with permission from [9].

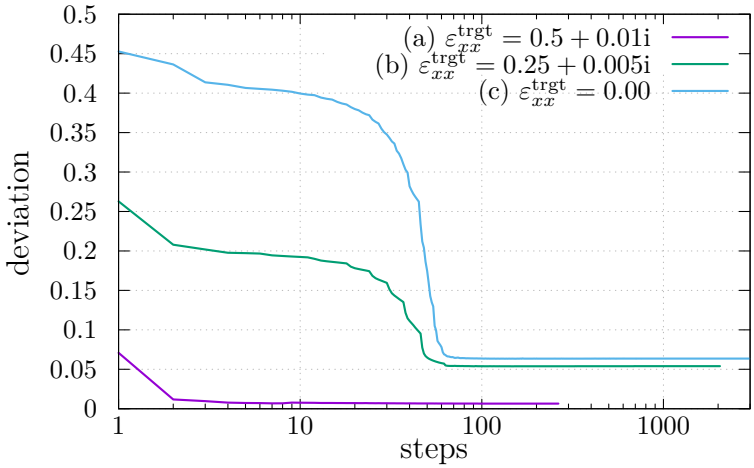

Figure 5.3: Evolution of the deviation, $\left\|\varepsilon^{\mathrm{eff}} - \varepsilon^{\mathrm{target}}\right\|_{\mathrm{Fr.}} / \left\|\varepsilon^{\mathrm{target}}\right\|_{\mathrm{Fr.}}$, during the BFGS solution process for the three cases (a) $0.5 + 0.01\mathrm{i}$, (b) $0.25 + 0.005\mathrm{i}$, to (c) 0.0. Reprinted with permission from [9].

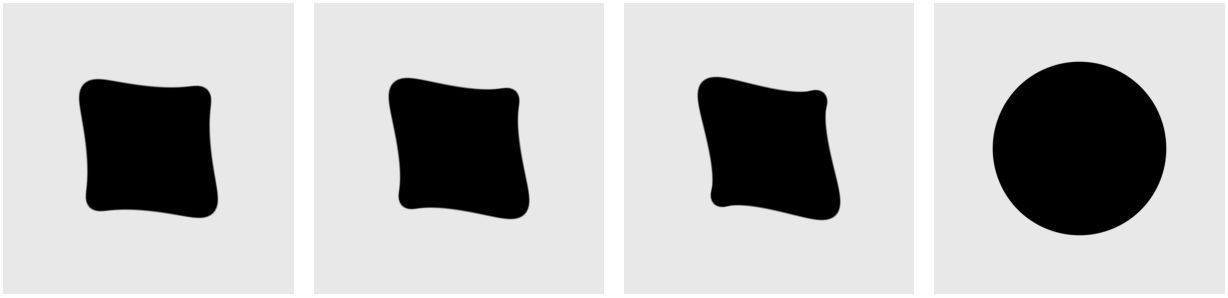

(a) $\varepsilon_{xy}^{\text{trgt.}} = 0.10$ (b) $\varepsilon_{xy}^{\text{trgt.}} = 0.15$ (c) $\varepsilon_{xy}^{\text{trgt.}} = 0.20$ (d) reference

Figure 5.4: Large deformation testcase: Final geometry obtained for target cases (a), (b) and (c) with increasingly larger $\{\varepsilon_{xy}^{\text{target}}, \varepsilon_{yx}^{\text{target}}\}$ components. Reprinted with permission from [9].

	$\varepsilon_{xx}^{\text{eff}}$	$\varepsilon_{xy}^{\text{eff}}$	initial	final	steps
ref.	$0.7783 + 0.003\text{i}$	$0.0 - 0.0\text{i}$			
(a)	$0.5254 + 0.063\text{i}$	$0.0953 - 0.013\text{i}$	41.8%	8.58%	$0 + 512$
(b)	$0.5256 + 0.063\text{i}$	$0.1429 - 0.020\text{i}$	44.7%	8.89%	$100 + 435$
(c)	$0.5258 + 0.063\text{i}$	$0.1904 - 0.027\text{i}$	48.4%	9.30%	$100 + 709$

Table 5.4: Large deformation testcase: Final permittivity tensors obtained for target cases (a), (b), (c), and the starting value for the undeformed reference configuration. In addition, we report the initial and final deviation, as well as the number of BFGS iterations in Algorithm 2 needed to achieve convergence.

5.2.3 Large mesh deformations

As a final test, we demonstrate that our optimization algorithm can handle larger mesh deformations. For this, we use again the target tensor introduced in Section 5.2.2 but vary the off-diagonal elements instead of the xx-component:

$$\varepsilon^{\text{target}} = \begin{pmatrix} 0.5 + 0.01 & * \\ * & 0.5 + 0.01\text{i} \end{pmatrix},$$

where we vary the $\varepsilon_{xy}^{\text{target}}$, $\varepsilon_{yx}^{\text{target}}$ components from (a) 0.10, (b) 0.15, to (c) 0.20. In addition, we set the angular frequency to $\omega = 0.4$.

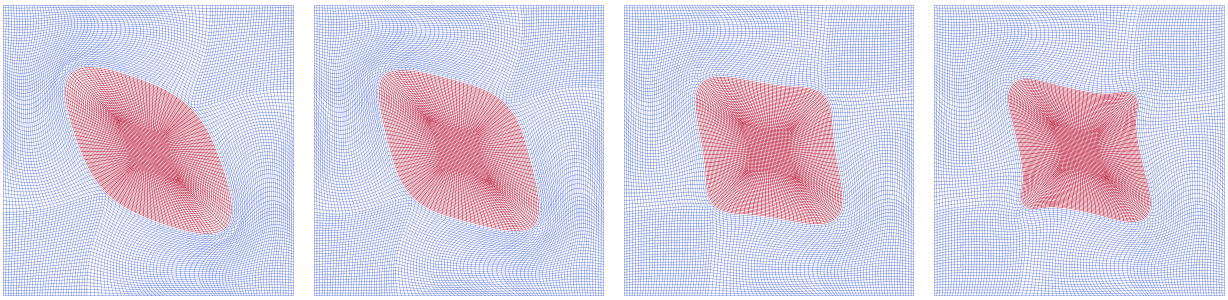

(a) step 10, dev. 23% (b) step 30, dev. 21 (c) step 100, dev. 16% (d) st. 100+50, dev. 9%

Figure 5.5: Large deformation testcase: Mesh evolution for Case (c) with $\varepsilon_{xy}^{\text{target}} = 0.2$ after (a) 10, (b) 30, and (c) 100 steps with a large regularization parameter $\beta = 0.8$, and (d) after running another 50 steps with a smaller penalty of $\beta = 0.1$. The deviation value reported is the normalized difference of the effective permittivity tensor to target tensor. Reprinted with permission from [9].

For visualization purposes, we also chose to run this set of computations with a lower resolution of 13 312 quadrilaterals (see also the discussion about mesh resolution in Section 5.2.1). The mesh deformation for cases (b) and (c) is so large that it would require to increase the values of the stabilization parameters significantly. This would result in a significantly higher deviation of the obtained permittivity tensor from the target tensor possibly beyond what would be deemed acceptable. We thus employ a slightly more sophisticated strategy: In cases (b) and (c) we first run 100 steps of the BFGS algorithm with a large penalty of $\beta = 0.4$ for (b) and $\beta = 0.8$ for (c) which ensures that the mesh does not degrade too much and the regular solutions shown in Figure 5.4 are obtained. Afterwards we fall back to the original stabilization value of $\beta = 0.1$ and run the BFGS algorithm until the stopping criterion is reached.

As reported in Figure 5.4 with the modified choice of target tensor and angular frequency a much more dramatic shape deformation away from a simple ellipse was achieved. The corresponding final permittivity tensors, final deviation and number of BFGS steps are reported in Table 5.4. We reach a final deviation of around 9% for all three cases. We report in Figure 5.5 the mesh evolution observed during the solution process for case (c) with $\varepsilon_{xy}^{\text{target}} = 0.2$.

The most crucial part in the solution process is between steps 30 and 100: if we lower β too much below 0.8 then the algorithm tries to approximate an eight-figure shape (and becoming singular in the process) instead of reaching the shape shown in Figure 5.4(c).

6. CONCLUSION AND OUTLOOK

In this thesis, a shape optimization problem for plasmonic crystals composed of dielectric inclusions is discussed. The objective of the work is to optimize the shape of microscale inclusions so that the effective permittivity tensor of the material matches a specified target. Achieving this goal requires modifying the geometrical configuration. A mesh deformation technique is introduced and incorporated within the framework of the cell problem.

Next, the thesis addresses the well-posedness and regularity of the deformed cell problem, ensuring that the modified problem provides a unique solution that behaves smoothly under deformation. This step is critical as it guarantees that the optimization process will converge and will arrive at a meaningful solution, even as the shapes are altered significantly. The mathematical framework and penalties established in the thesis provides the foundation for ensuring that these deformations do not introduce numerical instability and can often occur when handling complex shapes or large deformations. The numerical optimization techniques are introduced, and then the discretization is discussed. This provides the mathematical framework for the experiments.

A series of numerical experiments are conducted to validate the framework, with the results clearly demonstrating its capability to successfully solve the optimization problem. The numerical experiments not only show that the optimization method can converge to solutions, but also highlight the robustness of the approach when applied to large-scale shape modifications. The techniques are shown to effectively control the deformations while keeping the solution feasible and close to the desired target. In particular, the experimental setup demonstrates that despite the large-scale deformations, the optimization process remains stable and converges to the desired solution.

The work emphasizes the practical effectiveness and reliability of the proposed optimization approach, offering valuable insights for the design of plasmonic materials with customized properties, particularly for advanced applications in materials science.

6.1 Outlook: Frequency dependent approach

The approach described in this thesis is limited to optimizing a microstructure for a single fixed frequency ω. This is somewhat limiting as in practice a target permittivity that is valid over a (large) frequency interval is desired. In this regard we will explore how the optimization approach can be adapted to a result reported in [58].

6.1.1 Frequency response of ε^{eff}

The frequency response of $\varepsilon_{ij}^{\text{eff}}(\omega)$ is described by a purely algebraic expression

$$\varepsilon_{ij}^{\text{eff}}(\omega) \;=\; \varepsilon\,\delta_{ij} \;-\; \eta(\omega)\,N_{ij} \;-\; \sum_{n=1}^{\infty} \frac{\lambda_n\,\eta^2(\omega)}{\varepsilon - \lambda_n\,\eta(\omega)}\; M_{jn}\; M_{in},$$

where $\eta(\omega) = \frac{\sigma(\omega)}{\mathrm{i}\omega}$, the coefficient N_{ij} is a weight only depending on the geometry, and M_{in}, M_{jn} are weights depending on eigenfunctions φ_n with corresponding eigenvalues λ_n that are characterized by a purely geometric eigenvalue problem:

$$\begin{cases} \Delta\varphi_n(\boldsymbol{x})\big) = 0 & \text{in } Y \setminus \Sigma\ , \\ [\varphi_n(\boldsymbol{x}))]_\Sigma = 0 & \text{on } \Sigma\ , \\ \lambda_n\,[\boldsymbol{\nu}\cdot\nabla_{\mathbf{t}}\varphi_n(\boldsymbol{x})]_\Sigma = \nabla_{\mathbf{t}}\cdot\nabla_{\mathbf{t}}\varphi_n(\boldsymbol{x}) & \text{on } \Sigma\ . \end{cases}$$

The following analysis is summarized from [58] by Maier et al. The geometric problem is to identify all $\{\lambda_n\} \subset \mathbb{R}$ for which there exists a nonzero φ_n satisfying [58]:

$$\lambda_n \int_Y \tilde{\varepsilon}(\boldsymbol{x},\boldsymbol{y})\;\nabla\varphi_n(\boldsymbol{y})^T\cdot\overline{\nabla\psi(\boldsymbol{y})}\,\mathrm{d}y \;=\; \int_\Sigma \tilde{\sigma}(\boldsymbol{x},\boldsymbol{y})\;\nabla_{\mathbf{t}}\varphi_n(\boldsymbol{y})^T\cdot\nabla_{\mathbf{t}}\overline{\nabla\psi(\boldsymbol{y})}\,\mathrm{d}o_y,$$
$$\text{where } \int_\Sigma (\tilde{\sigma}(\boldsymbol{x},\boldsymbol{y})\nabla_{\mathbf{t}}\varphi_n(\boldsymbol{y}))\cdot\nabla_{\mathbf{t}}\varphi_n\,\mathrm{d}o_y = 1 \quad (6.1)$$

for all admissible test functions ψ.

We make the ansatz $\chi_j = \sum_n \alpha_n \varphi_n(\boldsymbol{y})$ and plug into our cell problem (2.25).

$$\sum_n \alpha_n \Big(\varepsilon(\omega) \int_Y \tilde{\varepsilon}(\boldsymbol{x},\boldsymbol{y})\, \nabla \varphi_n^T \cdot \overline{\nabla \psi(\boldsymbol{y})}\, \mathrm{d}y \;-\; \eta(\omega) \int_\Sigma \tilde{\sigma}(\boldsymbol{x},\boldsymbol{y})\, \nabla_{\mathbf{t}} \varphi_n^T \cdot \overline{\nabla_{\mathbf{t}} \psi(\boldsymbol{y})}\, \mathrm{d}o_y \Big)$$
$$= \; -\varepsilon(\omega) \int_Y \tilde{\varepsilon}(\boldsymbol{x},\boldsymbol{y})\, \boldsymbol{e}_j \cdot \overline{\nabla \psi(\boldsymbol{y})}\, \mathrm{d}y \;+\; \eta(\omega) \int_\Sigma \tilde{\sigma}(\boldsymbol{x},\boldsymbol{y})\, \boldsymbol{e}_{j_{\mathbf{t}}} \cdot \overline{\nabla_{\mathbf{t}} \psi(\boldsymbol{y})}\, \mathrm{d}o_y.$$

Using (6.1) and dividing by $\varepsilon(\omega)$ on both sides,

$$\sum_n \alpha_n \Big(\frac{1}{\lambda_n} - \frac{\eta(\omega)}{\varepsilon(\omega)} \Big) \int_\Sigma \tilde{\sigma}(\boldsymbol{x},\boldsymbol{y})\, \nabla_{\mathbf{t}} \varphi_n^T \cdot \overline{\nabla_{\mathbf{t}} \psi(\boldsymbol{y})}\, \mathrm{d}o_y$$
$$= \; -\int_Y \tilde{\varepsilon}(\boldsymbol{x},\boldsymbol{y})\, \boldsymbol{e}_j \cdot \overline{\nabla \psi(\boldsymbol{y})}\, \mathrm{d}y \;+\; \frac{\eta(\omega)}{\varepsilon(\omega)} \int_\Sigma \tilde{\sigma}(\boldsymbol{x},\boldsymbol{y})\, \boldsymbol{e}_{j_{\mathbf{t}}} \cdot \overline{\nabla_{\mathbf{t}} \psi(\boldsymbol{y})}\, \mathrm{d}o_y.$$

Testing with φ_k^T,

$$\sum_n \alpha_n \Big(\frac{1}{\lambda_n} - \frac{\eta(\omega)}{\varepsilon(\omega)} \Big) \int_\Sigma \tilde{\sigma}(\boldsymbol{x},\boldsymbol{y})\, \nabla_{\mathbf{t}} \varphi_n^T \cdot \overline{\nabla_{\mathbf{t}} \varphi_k^T}\, \mathrm{d}o_y$$
$$= \; -\int_Y \tilde{\varepsilon}(\boldsymbol{x},\boldsymbol{y})\, \boldsymbol{e}_j \cdot \overline{\nabla \varphi_k^T}\, \mathrm{d}y \;+\; \frac{\eta(\omega)}{\varepsilon(\omega)} \int_\Sigma \tilde{\sigma}(\boldsymbol{x},\boldsymbol{y})\, \boldsymbol{e}_{j_{\mathbf{t}}} \cdot \overline{\nabla_{\mathbf{t}} \varphi_k^T}\, \mathrm{d}o_y.$$

Finally, we rearrange and divide by $\left(\frac{1}{\lambda_n} - \frac{\eta(\omega)}{\varepsilon(\omega)} \right)$ on both sides to get

$$\alpha_n \;=\; -\frac{\varepsilon(\omega)\lambda_n}{\varepsilon(\omega) - \eta(\omega)\lambda_n} \int_Y \tilde{\varepsilon}(\boldsymbol{x},\boldsymbol{y})\, \boldsymbol{e}_j \cdot \overline{\nabla \varphi_k^T}\, \mathrm{d}o_y$$
$$+ \; \frac{\eta(\omega)\lambda_n}{\varepsilon(\omega) - \eta(\omega)\lambda_n} \int_\Sigma \tilde{\sigma}(\boldsymbol{x},\boldsymbol{y})\, \boldsymbol{e}_{j_{\mathbf{t}}} \cdot \overline{\nabla_{\mathbf{t}} \varphi_k^T}\, \mathrm{d}y. \quad (6.2)$$

Plugging into the effective permittivity tensor (2.24),

$$\begin{aligned}
\varepsilon_{ij}^{\text{eff}} = \varepsilon(\omega) \int_Y \tilde{\varepsilon}(\boldsymbol{x},\boldsymbol{y})\ \boldsymbol{e}_j \cdot \boldsymbol{e}_i \,\mathrm{d}y \ -\ \eta(\omega) \int_\Sigma \tilde{\sigma}(\boldsymbol{x},\boldsymbol{y})\ \boldsymbol{e}_{j_\mathbf{t}} \cdot \boldsymbol{e}_{i\mathbf{t}} \,\mathrm{d}o_y \\
- \sum_n \frac{(\varepsilon(\omega))^2 \lambda_n}{\varepsilon(\omega) - \eta(\omega)\lambda_n} \int_Y \tilde{\varepsilon}(\boldsymbol{x},\boldsymbol{y})\ \boldsymbol{e}_j \cdot \overline{\nabla \varphi_k^T} \,\mathrm{d}y \int_Y \tilde{\varepsilon}(\boldsymbol{x},\boldsymbol{y})\ \nabla \varphi_k^T \cdot \boldsymbol{e}_i \,\mathrm{d}y. \\
+ \sum_n \frac{\varepsilon(\omega)\eta(\omega)\lambda_n}{\varepsilon(\omega) - \eta(\omega)\lambda_n} \int_Y \tilde{\varepsilon}(\boldsymbol{x},\boldsymbol{y})\ \boldsymbol{e}_j \cdot \overline{\nabla \varphi_k^T} \,\mathrm{d}y \int_\Sigma \tilde{\sigma}(\boldsymbol{x},\boldsymbol{y})\ \nabla_\mathbf{t} \varphi_k^T \cdot \boldsymbol{e}_{i\mathbf{t}} \,\mathrm{d}o_y. \\
+ \sum_n \frac{\varepsilon(\omega)\eta(\omega)\lambda_n}{\varepsilon(\omega) - \eta(\omega)\lambda_n} \int_\Sigma \tilde{\sigma}(\boldsymbol{x},\boldsymbol{y})\ \boldsymbol{e}_{j_\mathbf{t}} \cdot \overline{\nabla_\mathbf{t} \varphi_k^T} \,\mathrm{d}o_y \int_Y \tilde{\varepsilon}(\boldsymbol{x},\boldsymbol{y})\ \nabla \varphi_k^T \cdot \boldsymbol{e}_i \,\mathrm{d}y. \\
- \sum_n \frac{\overline{\eta}^2(\omega)\lambda_n}{\overline{\varepsilon}(\omega) - \overline{\eta}(\omega)\lambda_n} \int_\Sigma \tilde{\sigma}(\boldsymbol{x},\boldsymbol{y})\ \boldsymbol{e}_{j_\mathbf{t}} \cdot \overline{\nabla_\mathbf{t} \varphi_k^T} \,\mathrm{d}o_y \int_\Sigma \tilde{\sigma}(\boldsymbol{x},\boldsymbol{y})\ \nabla_\mathbf{t} \varphi_k^T \cdot \boldsymbol{e}_{i\mathbf{t}} \,\mathrm{d}o_y. \quad (6.3)
\end{aligned}$$

Note that in (6.3), the integrals only depend on geometry, and the coefficients only depend on frequency. Equations (6.1) and (6.3) use the same convention and notations as (2.25) and (2.24).

6.1.2 Deformation of the spectral problem

We are now in a position to recast (6.1) using the definitions in section 3.1. We introduce a spectral problem to identify all $\{\hat{\lambda}_n[\hat{\boldsymbol{q}}]\} \subset \mathbb{R}$ for which there exists a $\hat{\varphi}_n[\hat{\boldsymbol{q}}]$ satisfying:

$$\begin{aligned}
\hat{\lambda}_n \int_{\hat{Y}} \tilde{\varepsilon}(x,y)\ \hat{F}(\hat{\boldsymbol{y}})^{-T} \hat{\nabla} \hat{\varphi}(\hat{\boldsymbol{y}})_n^T \cdot \nabla \hat{F}(\hat{\boldsymbol{y}})^{-T} \hat{\nabla} \overline{\hat{\psi}}(\hat{\boldsymbol{y}}) \hat{J} \,\mathrm{d}\hat{y} \\
= \int_{\hat{\Sigma}} \tilde{\sigma}(x,y) \Big(\sum_k \boldsymbol{\tau}_k \boldsymbol{\tau}_k^T (\hat{F}(\hat{\boldsymbol{y}})^{-T} \hat{\nabla} \hat{\varphi}_n(\hat{\boldsymbol{y}})^T) \Big) \\
\cdot \Big(\sum_k \boldsymbol{\tau}_k \boldsymbol{\tau}_k^T (\hat{F}(\hat{\boldsymbol{y}})^{-T} \hat{\nabla} \overline{\psi}(\hat{\boldsymbol{y}}) \Big) \| \hat{F}(\hat{\boldsymbol{y}})^{-T} \hat{\boldsymbol{\nu}} \|_{\ell^2} \hat{J} \,\mathrm{d}\hat{o}_{\hat{y}}, \quad (6.4)
\end{aligned}$$

where

$$\begin{aligned}
\int_{\hat{\Sigma}} \Big(\tilde{\sigma}(x,y) \sum_k \boldsymbol{\tau}_k \boldsymbol{\tau}_k^T (\hat{F}(\hat{\boldsymbol{y}})^{-T} \hat{\nabla} \hat{\varphi}_n(\hat{\boldsymbol{y}})) \Big) \\
\cdot \Big(\sum_k \boldsymbol{\tau}_k \boldsymbol{\tau}_k^T (\hat{F}(\hat{\boldsymbol{y}})^{-T} \hat{\nabla} \hat{\varphi}_n(\hat{\boldsymbol{y}})) \Big) \| \hat{F}(\hat{\boldsymbol{y}})^{-T} \hat{\boldsymbol{\nu}} \|_{\ell^2} \hat{J} \,\mathrm{d}\hat{o}_{\hat{y}} = 1 \quad (6.5)
\end{aligned}$$

for all admissible test functions $\hat{\psi}[\hat{\boldsymbol{q}}]$.

Using the tensors described in (3.9), (6.4) can be recast as

$$\hat{\lambda}_n \int_{\hat{Y}} \hat{\varepsilon}(\boldsymbol{x}, \boldsymbol{y}(\hat{\boldsymbol{y}}))\ \hat{\nabla}\hat{\varphi}_n(\hat{\boldsymbol{y}})^T \cdot \overline{\hat{\nabla}_{\hat{\mathbf{t}}}\hat{\psi}(\hat{\boldsymbol{y}})}\, \mathrm{d}\hat{y} \ = \ \int_{\hat{\Sigma}} \hat{\sigma}(\boldsymbol{x}, \boldsymbol{y}(\hat{\boldsymbol{y}}))\ \hat{\nabla}_{\hat{\mathbf{t}}}\hat{\varphi}_n(\hat{\boldsymbol{y}})^T \cdot \overline{\hat{\nabla}_{\hat{\mathbf{t}}}\hat{\psi}(\hat{\boldsymbol{y}})}\, \mathrm{d}\hat{o}_{\hat{y}},$$

$$\text{where } \int_{\hat{\Sigma}} (\hat{\sigma}(\boldsymbol{x}, \boldsymbol{y}(\hat{\boldsymbol{y}}))\hat{\nabla}_{\hat{\mathbf{t}}}\hat{\varphi}_n(\hat{\boldsymbol{y}})) \cdot \hat{\nabla}_{\hat{\mathbf{t}}}\hat{\varphi}_n\, \mathrm{d}\hat{o}_{\hat{y}} = 1 \quad (6.6)$$

With this formulation, we would prove that the deformed problem is well-posed, and also provide the regularity and robustness results required for the optimization algorithms.

6.1.3 Proposed cost function and optimization problem

Now, we formulate a tentative cost function for this problem. The penalties are similar to the ones in chapter 4, while the deviation term is now an absolute difference between two real numbers.

Definition 6.1.1. *For a given target λ^*, introduce a cost function:*

$$C((\hat{\lambda}, \hat{\boldsymbol{\varphi}}); \hat{\boldsymbol{q}}) := \frac{1}{2}|\hat{\lambda} - \lambda^*| + \frac{\alpha}{2}\Big(\|\hat{\boldsymbol{q}}\|^2 + \|\hat{\nabla}\hat{\boldsymbol{q}}\|^2\Big) + \beta \int_{\hat{Y}} P(\hat{\boldsymbol{y}}; \hat{\boldsymbol{q}})\, \mathrm{d}\hat{y},$$

$$P(\hat{\boldsymbol{y}}; \hat{\boldsymbol{q}}) := \begin{cases} \frac{1}{2}\frac{(\hat{J}(\hat{\boldsymbol{y}})-1)^2}{|\hat{J}(\hat{\boldsymbol{y}})|+\hat{J}(\hat{\boldsymbol{y}})} & \text{if } \hat{J}(\hat{\boldsymbol{y}}) < 1, \\ \\ \frac{1}{2}(\hat{J}(\hat{\boldsymbol{y}}) - 1)^2 & \text{if } \hat{J} \geq 1. \end{cases} \quad (6.7)$$

The proposed optimization problem is:

Definition 6.1.2. *We seek the solution* $((\hat{\lambda}, \hat{\varphi}); \hat{\boldsymbol{q}}) \in X := ((\mathbb{R} \times \boldsymbol{H}(\hat{Y}, \hat{\Sigma})) \times \boldsymbol{D}(\hat{Y}, \hat{\Sigma}))$

$$\min_{((\hat{\lambda},\hat{\boldsymbol{\varphi}});\hat{\boldsymbol{q}})} C((\hat{\lambda}, \hat{\boldsymbol{\varphi}}); \hat{\boldsymbol{q}}) \ s.t.$$

$$\hat{\lambda} \int_{\hat{Y}} \hat{\varepsilon}(\boldsymbol{x}, \boldsymbol{y}(\hat{\boldsymbol{y}}))\ \hat{\nabla}\hat{\varphi}(\hat{\boldsymbol{y}})^T \cdot \overline{\hat{\nabla}_{\hat{\mathbf{t}}}\hat{\psi}(\hat{\boldsymbol{y}})}\, \mathrm{d}\hat{y} \ = \ \int_{\hat{\Sigma}} \hat{\sigma}(\boldsymbol{x}, \boldsymbol{y}(\hat{\boldsymbol{y}}))\ \hat{\nabla}_{\hat{\mathbf{t}}}\hat{\varphi}(\hat{\boldsymbol{y}})^T \cdot \overline{\hat{\nabla}_{\hat{\mathbf{t}}}\hat{\psi}(\hat{\boldsymbol{y}})}\, \mathrm{d}\hat{o}_{\hat{y}},$$

for all admissible test functions $\hat{\psi}$, *and*

$$\int_{\hat{\Sigma}} (\hat{\sigma}(\boldsymbol{x}, \boldsymbol{y}(\hat{\boldsymbol{y}}))\hat{\nabla}_{\hat{\mathbf{t}}}\hat{\varphi}(\hat{\boldsymbol{y}})) \cdot \hat{\nabla}_{\hat{\mathbf{t}}}\hat{\varphi}\, \mathrm{d}\hat{o}_{\hat{y}} = 1. \tag{6.8}$$

We would once again proceed with an adjoint approach and iterative optimization algorithms.

6.2 Outlook: Computational efficiency

A major computational bottleneck with this shape optimization routine is the repeated assembly of the finite element and mesh at each iterative step of the optimization. A proposed solution is to speed up the finite element assembly using `GraphBLAS` [20].

6.2.1 Sparsity pattern

Creating the sparsity pattern of an assembled finite-element matrix is simple and fast using `GraphBLAS` [62]. A finite-element analysis creates a sparse n-by-n matrix $\mathbf{A}$ that is the sum of m individual finite-elements, $\mathbf{A} = \sum_{k=1}^{m} \mathbf{A}_k$. The matrix $\mathbf{A}_k$ is a very sparse n-by-n matrix that can be thought of as the adjacency matrix of a single small clique in a graph of n nodes. In terms of a matrix, $\mathbf{A}_k$ has nonzero entries only in the positions defined by the Cartesian product of two small lists of integers, typically of length 9 to 30. If the sparsity pattern of $\mathbf{A}_k$ is symmetric then only one such list is needed. The size of this list depends on the kind of discretization (2D or 3D, polynomial degree of finite element ansatz, continuous or discontinuous) and the kind of differential equations being modeled by the finite-element method.

Let $\mathbf{F}$ be an m-by-n boolean matrix that represents m finite elements. The structure of the kth finite-element is represented by the kth row, $\mathbf{F}_{k*}$, and the list of column indices of

entries present in this row gives the list of integer indices that define the sparsity pattern of $\mathbf{A}_k$. The outer product of the two vectors $\mathbf{F}_{k*}^{\mathsf{T}} \vee . \wedge \mathbf{F}_{k*}$ gives the sparsity pattern of the kth finite-element, and thus the sparsity pattern of $\mathbf{A}$ is $\mathbf{F}^{\mathsf{T}} \vee . \wedge \mathbf{F}$, via a single call to `GrB_mxm`. Applying this technique in the `deal.II` finite-element package [7] yields a speedup of about 4x for the overall strategy, and 15x when comparing only the portion handled by GraphBLAS, on an 18-core shared-memory system, since the existing assembly of the sparsity pattern is handled with a single-threaded algorithm in `deal.II` version 9.5. For matrices with unsymmetric sparsity pattern and rectangular finite-elements, we can replace $\mathbf{F}^{\mathsf{T}}$ with a different matrix $\mathbf{G}$ and compute $\mathbf{A} = \mathbf{G} \vee . \wedge \mathbf{F}$ instead.

6.2.2 Proposed usage of `GrB_IndexBinaryOp`

We [62] propose using the `GrB_IndexBinaryOp` to create the numerical values of $\mathbf{A}$ as well, with a semiring that constructs each entry of $\mathbf{A}_k$ inside its multiplicative operator. Suppose the entries f_{ki} and f_{kj} of $\mathbf{F}$ contain a user-defined data type with enough information, along with the scalar θ, so that an index binary operator can compute $(\mathbf{A}_k)_{ij} = \otimes(f_{ki}, f_{kj}, i, k, j, \theta)$. This operator would have access to all three indices i, j, and k, as well as the user-defined scalar θ. The data type of θ could be simply a pointer to a complex user-provided data structure, and could be dereferenced with k and perhaps the *global* indices i and j to find any information need for the kth finite-element.

It may also be useful for this $\otimes$ operator to have access to the *local* indices, i_{local} and j_{local} of the $(\mathbf{A}_k)_{ij}$ entry. The local index i_{local} is an index into a small dense finite-element; that is, if f_{ki} is the third entry present in the kth row of $\mathbf{F}_{k*}$, then $i_{\text{local}} = 3$ (or 2 if zero-based indexing is used). This local index is not part of the proposed `GrB_IndexBinaryOp`, so if needed it would be added to the user-defined data type and encoded in the value of f_{ki}. We anticipate other uses for this local index in LAGraph such as in the Connected Components algorithm which requires the selection of the leftmost 4 entries in each row. This suggests future work on an indexed binary operator that includes such local indices.

REFERENCES

[1] A. M Urbas et al., "Roadmap on optical metamaterials," *J. Opt.*, vol. 18, no. 9, p. 093005, 2016. [Online]. Available: https://doi.org/10.1088%2F2040-8978%2F18%2F9%2F093005

[2] G. Allaire, "Homogenization and two-scale convergence." *SIAM Journal on Mathematical Analysis*, vol. 23, no. 6, pp. 1482–1518, 1992.

[3] I. F. Almog, M. S. Bradley, and V. Bulović, "Lorentz force and electromagnetic energy," MIT OpenCourseWare, Course 6.007: Electromagnetic Energy: From Motors to Lasers, 2011, accessed: 2025-02-21. [Online]. Available: https://ocw.mit.edu/courses/6-007-electromagnetic-energy-from-motors-to-lasers-spring-2011/af10a4aa72a61e655726e72a47e8b71e_MIT6_007S11_lorentz.pdf

[4] A. Alù and N. Engheta, "Achieving transparency with plasmonic and metamaterial coatings," *Physical Review E*, vol. 72, p. 016623, Jul 2005.

[5] Y. Amirat and V. V. Shelukhin, "Homogenization of time harmonic Maxwell equations: the effect of interfacial currents," *Mathematical Methods in the Applied Sciences*, vol. 40, no. 8, pp. 3140–3162, 2017.

[6] D. Arndt, W. Bangerth, D. Davydov, T. Heister, L. Heltai, M. Kronbichler, M. Maier, J.-P. Pelteret, B. Turcksin, and D. Wells, "The deal.II finite element library: design, features, and insights," *Computers & Mathematics with Applications*, vol. 81, no. 1, pp. 407–422, 2021.

[7] D. Arndt, W. Bangerth, M. Feder, M. Fehling, R. Gassmöller, T. Heister, L. Heltai, M. Kronbichler, M. Maier, P. Munch, J.-P. Pelteret, S. Sticko, B. Turcksin, and D. Wells, "The deal.II Library, Version 9.4," *journal of Numerical Mathematics*, 2022.

[8] R. Becker, D. Meidner, and B. Vexler, "Efficient numerical solution of parabolic optimization problems by finite element methods," *Optimization Methods and Software*, vol. 22, no. 5, pp. 813–833, 2007.

[9] M. Bezbaruah, M. Maier, and W. Wollner, "Shape optimization of optical microscale inclusions," *SIAM Journal on Scientific Computing*, vol. 46, no. 4, pp. B377–B402, 2024.

[10] V. I. Bogachev and E. Mayer-Wolf, "Some remarks on Rademacher's theorem in infinite dimensions," *Potential Analysis*, vol. 5, pp. 23–30, 1996.

[11] C. Brandenburg, F. Lindemann, M. Ulbrich, and S. Ulbrich, "A continuous adjoint approach to shape optimization for navier stokes flow," in *Optimal control of coupled systems of partial differential equations*. Springer, 2009, pp. 35–56.

[12] A. H. Castro Neto, F. Guinea, N. M. R. Peres, K. S. Novoselov, and A. K. Geim, "The electronic properties of graphene," *Rev. Mod. Phys.*, vol. 81, pp. 109–162, 2009.

[13] T. Chang, X. Zhang, X. Zhang, and H.-L. Cui, "Accurate determination of dielectric permittivity of polymers from 75GHz to 1.6THz using both S-parameters and transmission spectroscopy," *Appl. Opt.*, vol. 56, no. 12, pp. 3287–3292, 2017. [Online]. Available: http://ao.osa.org/abstract.cfm?URI=ao-56-12-3287

[14] J. Cheng, W. L. Wang, H. Mosallaei, and E. Kaxiras, "Surface plasmon engineering in graphene functionalized with organic molecules: A multiscale theoretical investigation," *Nano Letters*, vol. 14, no. 1, pp. 50–56, 2014.

[15] T. C. Choy, *Effective Medium Theory: Principles and Applications*. Oxford, UK: Clarendon Press, 1999, chap. 3.

[16] C. L. Cortes, W. Newman, S. Molesky, and Z. Jacob, "Quantum nanophotonics using hyperbolic metamaterials," *J. Opt.*, vol. 14, p. 063001, 2012.

[17] C. Cortes, W. Newman, S. Molesky, and Z. Jacob, "Corrigendum: Quantum nanophotonics using hyperbolic metamaterials," *J. Opt.*, vol. 16, p. 129501, 2014.

[18] S. Dai, Q. Ma, M. K. Liu, T. Andersen, Z. Fei, M. D. Goldflam, M. Wagner, K. Watanabe, T. Taniguchi, M. Thiemens, F. Keilmann, G. C. A. M. Janssen, S.-E. Zhu, P. Jarillo-Herrero, M. M. Fogler, and D. N. Basov, "Graphene on hexagonal boron nitride as a tunable hyperbolic metamaterial," *Nat. Nano*, vol. 10, pp. 682–686, 2015.

[19] C. L. Davies, J. B. Patel, C. Q. Xia, L. M. Herz, and M. B. Johnston,

"Temperature-dependent refractive index of quartz at terahertz frequencies," *J. Infrared Millim. Te.*, vol. 39, no. 12, pp. 1236–1248, Dec 2018. [Online]. Available: https://doi.org/10.1007/s10762-018-0538-7

[20] T. A. Davis, "Algorithm 10xx: Suitesparse:graphblas: Graph algorithms in the language of sparse linear algebra," *ACM Trans. Math. Softw.*, (under revision) 2022.

[21] H. Deng, F. Ye, B. A. Malomed, X. Chen, and N. C. Panoiu, "Optically and electrically tunable dirac points and Zitterbewegung in graphene-based photonic superlattices," *Phys. Rev. B*, vol. 91, p. 201402(R), 2015.

[22] H. Deng, Y. Chen, C. Huang, and F. Ye, "Topological interface modes in photonic superlattices containing negative-index materials," *Europhys. Lett.*, vol. 124, no. 6, p. 64001, 2018.

[23] P. Drude, "Zur elektronentheorie der metalle," *Annalen der Physik*, vol. 306, no. 3, pp. 566–613, 1900. [Online]. Available: https://onlinelibrary.wiley.com/doi/10.1002/andp.19003060312

[24] S. Frei, H. Andrä, R. Pinnau, and O. Tse, "Optimizing fiber orientation in fiber-reinforced materials using efficient upscaling," *Computational Optimization and Applications*, vol. 62, no. 1, pp. 111–129, 2015.

[25] T. Galfsky, E. E. Narimanov, and V. M. Menon, "Enhanced spontaneous emission in photonic hypercrystals," in *Frontiers in Optics 2015*, ser. OSA Technical Digest, 2015, paper FW6A.3, pp. 1, 2. [Online]. Available: https://www.osapublishing.org/abstract.cfm?uri=FiO-2015-FW6A.3

[26] A. K. Geim and I. V. Grigorieva, "Van der waals heterostructures," *Nature (London)*, vol. 499, pp. 419–425, 2013.

[27] D. Gilbarg and N. S. Trudinger, *Elliptic Partial Differential Equations of Second Order*, 2nd ed., ser. Classics in Mathematics. Springer, 2001, vol. 224.

[28] C. Goll, T. Wick, and W. Wollner, "DOpElib: Differential equations and optimization environment; a goal oriented software library for solving pdes and optimization problems

with pdes," *Archive of Numerical Software*, vol. 5, no. 2, 2017.

[29] A. Griewank, "The local convergence of Broyden-like methods on Lipschitzian problems in Hilbert spaces," *SIAM Journal of Numerical Analysis*, vol. 24, no. 3, pp. 684–705, 1987.

[30] A. N. Grigorenko, M. Polini, and K. S. Novoselov, "Graphene plasmonics," *Nature Photonics*, vol. 6, pp. 749–758, 2012.

[31] E. Hassan and A. C. Lesina, "Time-domain topology optimization of wideband dispersive plasmonic nanostructures," in *2022 Photonics North (PN)*, 2022, pp. 1–1.

[32] J. Haubner, M. Ulbrich, and S. Ulbrich, "Analysis of shape optimization problems for unsteady fluid-structure interaction," *Inverse Problems*, vol. 36, no. 3, p. 034001, 2020.

[33] H. A. Haus, *Waves and Fields in Optoelectronics*. Englewood Cliffs, NJ: Prentice Hall, 1984, chap. 5.

[34] C. Herter and W. Wollner, "Numerical eigenvalue optimization by shape-variations for electromagnetic cavities," 2023, in preparation.

[35] M. Hinze, R. Pinnau, M. Ulbrich, and S. Ulbrich, *Optimization with PDE Constraints*, ser. Mathematical Modelling: Theory and Applications. Springer, 2009, vol. 23.

[36] H. Hu, X. Guo, D. Hu, Z. Sun, X. Yang, and Q. Dai, "Flexible and electrically tunable plasmons in graphene– mica heterostructures," *Adv. Sci.*, vol. 5, p. 1800175, 2018.

[37] H. Hu, X. Yang, X. Guo, K. Khaliji, S. R. Biswas, F. J. G. de Abajo, T. Low, Z. Sun, and Q. Dai, "Gas identification with graphene plasmons," *Nat. Commun.*, vol. 10, p. 1131, 2019.

[38] X. Huang, Y. Lai, Z. H. Hang, H. Zheng, and C. T. Chan, "Dirac cones induced by accidental degeneracy in photonic crystals and zero-refractive-index materials," *Nat. Mater.*, vol. 10, pp. 582–586, 2011.

[39] M. Jablan, M. Soljačić, and H. Buljan, "Plasmons in graphene: Fundamental properties and potential applications," *Proc. IEEE*, vol. 101, no. 7, pp. 1689–1704, 2013.

[40] C. T. Kelley and E. W. Sachs, "A new proof of superlinear convergence for Broyden's

method in Hilbert space," *SIAM Journal on Optimization*, vol. 1, no. 1, pp. 146–150, 1991.

[41] S. Kim, M. S. Jang, V. W. Brar, K. W. Mauser, L. Kim, and H. A. Atwater, "Electronically tunable perfect absorption in graphene," *Nano Lett.*, vol. 18, no. 2, pp. 971–979, 2018.

[42] S. Kim, S. G. Menabde, V. W. Brar, and M. S. Jang, "Functional mid-infrared polaritonics in van der waals crystals," *Adv. Opt. Mater.*, p. 1901194, 2019.

[43] A. Kumar, T. Low, K. H. Fung, P. Avouris, and N. X. Fang, "Tunable light-matter interaction and the role of hyperbolicity in graphene-hbn system," *Nano Lett.*, vol. 15, pp. 3172–3180, 2015.

[44] I.-H. Lee, D. Yoo, P. Avouris, T. Low, and S.-H. Oh, "Graphene acoustic plasmon resonator for ultrasensitive infrared spectroscopy," *Nat. Nano*, vol. 14, pp. 313–319, 2019.

[45] W. Li, R. Lipton, and M. Maier, "Lorentz resonance in the homogenization of plasmonic crystals," *Proceedings of the Royal Society A: Mathematical, Physical, and Engineering Sciences*, vol. 477, p. 20210609, 2021.

[46] Y. Li, S. Kita, P. Muñoz, O. Reshef, D. I. Vulis, M. Yin, M. Lončar, and E. Mazur, "On-chip zero-index metamaterials," *Nat. Photon.*, vol. 9, pp. 738–742, 2015.

[47] Z. Q. Li, E. A. Henriksen, Z. Jiang, Z. Hao, M. C. Martin, P. Kim, H. L. Stormer, and D. N. Basov, "Dirac charge dynamics in graphene by infrared spectroscopy," *Nat. Phys.*, vol. 4, pp. 532–535, 2008.

[48] I. Liberal and N. Engheta, "Near-zero refractive index photonics," *Nature Photonics*, vol. 11, pp. 149–158, 2017.

[49] T. Low, A. Chaves, J. D. Caldwell, A. Kumar, N. X. Fang, P. Avouris, T. F. Heinz, F. Guinea, L. Martín-Moreno, and F. Koppens, "Polaritons in layered two-dimensional materials," *Nat. Mater.*, vol. 16, pp. 182–194, 2017.

[50] A. Lucas and K. C. Fong, "Hydrodynamics of electrons in graphene," *J. Phys.: Condens.*

Matter, vol. 30, p. 053001, 2018.

[51] P. Ma, Y. Salamin, B. Baeuerle, A. Josten, W. Heni, A. Emboras, and J. Leuthold, "Plasmonically enhanced graphene photodetector featuring 100 gbit/s data reception, high responsivity, and compact size," *ACS Photon.*, vol. 6, no. 1, pp. 154–161, 2019.

[52] M. Mahmoodi, S. H. Tavassoli, O. Takayama, J. Sukham, R. Malureanu, and A. V. Lavrinenko, "Existence conditions of high-k modes in finite hyperbolic metamaterials," *Laser Photon. Rev.*, vol. 13, p. 1800253, 2019.

[53] M. Maier, D. Margetis, and M. Luskin, "Dipole excitation of surface plasmon on a conducting sheet: finite element approximation and validation," *J. Comp. Phys.*, vol. 339, pp. 126–145, 2017.

[54] ——, "Generation of surface plasmon-polaritons by edge effects," *Commun. Math. Sci.*, vol. 16, pp. 77–95, 2018.

[55] M. Maier, M. Mattheakis, E. Kaxira, M. Luskin, and D. Margetis, "Universal behavior of dispersive Dirac cone in gradient-index plasmonic metamaterials," *Phys. Rev. B*, vol. 97, p. 035307, 2018.

[56] M. Maier, W. X. Boo, and E. Kaxira, "Graphene epsilon-near-zero plasmonic crystals," in *Proceedings of the Sixth Annual ACM International Conference on Nanoscale Computing and Communication*, ser. NANOCOM '19, 2019, pp. 2:1–2:6. [Online]. Available: https://arxiv.org/abs/1906.00018

[57] M. Maier, M. Mattheakis, E. Kaxira, M. Luskin, and D. Margetis, "Homogenization of plasmonic crystals: seeking the epsilon-near-zero effect," *Proc. R. Soc. A*, vol. 475, p. 20190220, 2019.

[58] M. Maier, M. Mattheakis, E. Kaxiras, M. Luskin, and D. Margetis, "Homogenization of plasmonic crystals: Seeking the epsilon-near-zero effect," *Proceedings of the Royal Society A: Mathematical, Physical, and Engineering Sciences*, vol. 475, 2019.

[59] M. Maier, D. Margetis, and M. Luskin, "Finite-size effects in wave transmission through plasmonic crystals: A tale of two scales," *Physical Review B*, vol. 102, p. 075308, 2020.

[60] M. Maier, D. Margetis, and A. Mellet, "Homogenization of Maxwell's equations in nonhomogeneous plasmonic structures," *Journal of Computational and Applied Mathematics*, vol. 377, 2020.

[61] M. Mattheakis, C. A. Valagiannopoulos, and E. Kaxiras, "Epsilon-near-zero behavior from plasmonic dirac point: Theory and realization using two-dimensional materials," *Phys. Rev. B*, vol. 94, p. 201404(R), 2016.

[62] T. Mattson, M. Bezbaruah, M. Maier, S. McMillan, M. Pelletier, E. Welch, and T. Davis, "Indexed binary operations in the graphblas," in *28th Annual IEEE High Performance Extreme Computing*, 2024.

[63] N. Mohammadi Estakhri, C. Argyropoulos, and A. Alù, "Graded metascreens to enable a new degree of nanoscale light management," *Philosophical transactions. Series A, Mathematical, physical, and engineering sciences*, vol. 373, no. 2049, p. 20140351, 2015.

[64] P. Moitra, Y. Yang, Z. Anderson, I. I. Kravchenko, D. P. Briggs, and J. Valentine, "Realization of an all-dielectric zero-index optical metamaterial," *Nature Photonics*, vol. 7, pp. 791–795, 2013.

[65] S. Molesky, Z. Lin, A. Y. Piggott, W. Jin, J. Vucković, and A. W. Rodriguez, "Inverse design in nanophotonics," *Nature Photon*, vol. 12, pp. 659–670, 2018.

[66] P. Monk, *Finite Element Methods for Maxwell's Equations*, ser. Numerical Mathematics and Scientific Computation. Oxford University Press, 2003.

[67] A. Nematpour, N. Lim, A. Piegari, L. Lancellotti, G. Hu, and M. L. Grilli, "Experimental near infrared absorption enhancement of graphene layers in an optical resonant cavity," *Nanotechnology*, vol. 30, no. 44, p. 445201, 2019.

[68] A. Nemilentsau, T. Low, and G. Hanson, "Anisotropic 2d materials for tunable hyperbolic plasmonics," *Phys. Rev. Lett.*, vol. 116, p. 066804, 2016.

[69] G. Nguetseng, "A general convergence result for a functional related to the theory of homogenization." *SIAM Journal on Mathematical Analysis*, vol. 20, no. 3, pp. 608–623, 1989.

[70] V. Nikkhah, M. J. Mencagli, and N. Engheta, "Reconfigurable nonlinear optical element using tunable couplers and inverse-designed structure," *Nanophotonics*, 2023.

[71] K. S. Novoselov, V. I. Fal'ko, L. Colombo, P. R. Gellert, M. G. Schwab, and K. Kim, "A roadmap for graphene," *Nature (London)*, vol. 490, pp. 192–200, 2012.

[72] A. N. Papadimopoulos, A. Duspayev, N. L. Tsitsas, N. V. Kantartzis, and C. Valagiannopoulos, "Wavefront engineering with optimally loaded absorbing metamirrors," *Phys. Rev. B*, vol. 103, p. 165307, 2021.

[73] P. Papadopoulos, "Me 185 course notes," Berkeley Center for Computational and Data Science in Mechanics, 2020, accessed: 2025-02-21. [Online]. Available: https://csml.berkeley.edu/Notes/ME185.pdf

[74] G. Pavliotis and A. M. Stuart, *Multiscale methods: Averaging and homogenization*. Berlin, Germany: Springer, 2007.

[75] T. Richter, *Fluid-structure interactions: models, analysis and finite elements*. Springer, 2017, vol. 118.

[76] J. Si and C. Sun, "On the optical performance of composite structures of graphene and photonic crystals at infrared wavelengths," *J. Appl. Phys.*, vol. 122, p. 133104, 2017.

[77] A. Silva, F. Monticone, G. Castaldi, V. Galdi, A. Alù, and N. Engheta, "Performing mathematical operations with metamaterials," *Science*, vol. 343, no. 6167, pp. 160–163, 2014.

[78] M. Silveirinha and N. Engheta, "Tunneling of electromagnetic energy through subwavelength channels and bends using ϵ-near-zero materials," *Phys. Rev. Lett.*, vol. 97, p. 157403, 2006.

[79] A. J. M. Spencer, *Continuum Mechanics*. Dover Publications, 2004.

[80] T. Tan, X. Jiang, C. Wang, B. Yao, and H. Zhang, "2D material optoelectronics for information functional device applications: Status and challenges," *Advanced Science*, vol. 7, no. 11, p. 2000058, 2020.

[81] F. Torres, S. Roche, and J. Charlier, *Introduction to Graphene-Based Nanomaterials:*

From Electronic Structure to Quantum Transport. Cambridge, UK: Cambridge University Press, 2014.

[82] F. Tröltzsch, *Optimal control of partial differential equations*, ser. Graduate Studies in Mathematics. American Mathematical Society, Providence, RI, 2010, vol. 112.

[83] N. Wellander, "Homogenization of the Maxwell equations: Case ii. nonlinear conductivity," *Applications of Mathematics*, vol. 47, no. 3, pp. 255–283, 2002.

[84] ——, "Homogenization of the Maxwell equations: Case i. linear theory," *Applications of Mathematics*, vol. 46, no. 1, pp. 29–51, 2001.

[85] N. Wellander and G. Kristensson, "Homogenization of the Maxwell equations at fixed frequency," *SIAM Journal on Applied Mathematics*, vol. 64, no. 1, pp. 170–195, 2003.

[86] H. Xueqin, L. Yun, H. Zhi, Z. Huihuo, and C. T. Chan, "Dirac cones induced by accidental degeneracy in photonic crystals and zero-refractive-index materials," *Nature Materials*, vol. 10, pp. 582–586, 2011.

[87] H. Yan, X. Li, B. Chandra, G. Tulevski, Y. Wu, M. Freitag, W. Zhu, P. Avouris, and F. Xia, "Tunable infrared plasmonic devices using graphene/insulator stacks," *Nat. Nano*, vol. 7, pp. 330–334, 2012.

[88] H. Yang, Y. Wang, Z. C. Tiu, S. J. Tan, L. Yuan, and H. Zhang, "All-optical modulation technology based on 2D layered materials," *Micromachines*, vol. 13, no. 1, p. 92, 2022.

[89] B. Yao, Y. Liu, S.-W. Huang, C. Choi1, Z. Xie, J. F. Flores, Y. Wu, M. Yu, D.-L. Kwong, Y. Huang, Y. Rao, X. Duan, and C. W. Wong, "Broadband gate-tunable terahertz plasmons in graphene heterostructures," *Nat. Photon.*, vol. 12, pp. 22–28, 2018.

[90] P. Yeh, *Optical Waves in Layered Media*, 2nd ed. Hoboken, NJ: Wiley, 2005, chap. 5.

[91] S. V. Zhukovsky, A. Andryieuski, J. E. Sipe, and A. V. Lavrinenko, "From surface to volume plasmons in hyperbolic metamaterials: General existence conditions for bulk high-**k** waves in metal-dielectric and graphene-dielectric multilayers," *Phys. Rev. B*, vol. 90, p. 2155429, 2014.